U.S.NRC
United States Nuclear Regulatory Commission
Protecting People and the Environment

ASSESSMENT OF SAN ONOFRE CONCRETE SUSCEPTIBILITY AGAINST IRRADIATION DAMAGE

Prepared by:
Yann Le Pape, Elena Tajuelo, Paula Bran Anleu, Adam Brooks, Lawrence M. Anovitz, Arzu Alpan, Julia Sheets (Ohio State University), Michael Koehler (University of Tennessee, Knoxville), Gernot Rother and Thomas M. Rosseel

Oak Ridge National Laboratory
One Bethel Valley Road
Oak Ridge, TN 37830

Madhumita Sircar, NRC
Technical Lead and Project Manager

Research Information Letter
Office of Nuclear Regulatory Research

Disclaimer

Legally binding regulatory requirements are stated only in laws, NRC regulations, licenses, including technical specifications, or orders; not in Research Information Letters (RILs). A RIL is not regulatory guidance, although NRC's regulatory offices may consider the information in a RIL to determine whether any regulatory actions are warranted.

ABSTRACT

The work performed under this contract covers the characterization of unirradiated concrete specimens cored from the walls of the steam generator room of the SONGS Unit 2, currently under decommission. This report documents the extensive set of characterization conducted at the Oak Ridge National Laboratory, at the University of Tennessee, Knoxville, at the Ohio State University, and at ALG Global. The susceptibility of irradiation-induced damage in concrete is governed by the exposure level (fast neutron fluence > 10^{19} n.cm^{-2} at E > 0.1 MeV) and the mineralogy of the aggregates (high quartz content and chemical heterogeneity of the assemblage). Both conditions are met for the SONGS concrete biological shield. Hence, harvesting in-service irradiated concrete from the SONGS Unit 2 or 3 biological shield is currently an unparalleled opportunity to study the flux effects of neutron irradiation.

TABLE OF CONTENTS

LIST OF FIGURES

LIST OF TABLES

EXECUTIVE SUMMARY

Context

Nuclear power plants (NPPs) in the US were originally licensed for 40 years of operation. Since then, many plants have undergone a license renewal process to extend the plant operation to 60 years, and most other remaining NPPs are planning to do the same. Currently, subsequent license renewal (SLR) from 60 to 80 years has been initiated. Per Commission direction in the August 29, 2014, Staff Requirements Memorandum (SRM) to SECY-014-0016, the staff should keep the Commission informed on the progress of resolving various technical issues related to SLR, including technical issues related to concrete and concrete degradation. This SRM also directs the staff to emphasize in communications with the industry the need to strive for satisfactory resolution of these issues. The Expanded Material Degradation Assessment (EMDA) Report, NUREG/CR-7153, Vol. 4, "Aging of Concrete and Civil Structures," dated October 2014, identifies radiation effects on concrete as low knowledge but high significance related to SLR. Based on this assessment and the Office of Nuclear Reactor Regulation (NRR) User Need Request for Research on the Effects of Irradiation on Concrete Structures, the Office of Nuclear Regulatory Research (RES) is conducting research to confirm the effects of irradiation on the concrete structures and the structural implications of these effects to support long-term operation of NPPs. The work under this contract covers the characterization of concrete specimens cored from outside of Steam Generator Room 2 (106) on the north wall of the primary shield at elevations of 45, 30 and 17 feet of the SONGS Unit 2, currently under decommission.

Objectives

The main objective of this project was to assess the opportunity of future harvesting of irradiated concrete cores from the most exposed region of the biological shield (i.e., facing directly toward the reactor pressure vessel (RPV) at the approximate elevation of the belt line). The susceptibility of irradiation-induced damage of concrete is governed by the mineralogy of its aggregates. This report documents the extensive set of characterization conducted at the Oak Ridge National Laboratory, the University of Tennessee, Knoxville, the Ohio State University, and ALG Global.

Accomplishments

Despite the lack of clear identification of the quarry selected to extract the aggregates used for the construction of concrete structures in SONGS Units 2 and 3 in the late 70s, it is likely that they contain a complex assemblage of shale (mudstone), San Onofre breccia, sandstone, and limestone, and that they are rich in varied silicates including quartz, plagioclase feldspar, felspathoid, clay, biotite, talc, and amphibole (hornblende, actinolite, tremolite).

Three unirradiated concrete specimens were harvested by SONGS Decommissioning Solutions (SDS) at three different elevations of the primary shield. After careful removal of the aggregates from the concrete cores and preparation for characterization, a selected set of techniques, including ultrasonic pulse velocity, thin-section petrography, micro x-ray fluorescence, x-ray diffraction, energy dispersive x-ray spectroscopy, inductively coupled plasma spectroscopy, and scanning electron microscopy (SEM), were employed to assess the composition and physical properties of the aggregates and concrete. The main findings of this research are as follows:

1. The quality of the concrete is sound (dynamic modulus ranging between 44–48 GPa); The aggregates appear to be well bonded to the cement paste.

2. The aggregates are a complex assemblage of mostly silicate minerals. The quartz content of the characterized aggregates varies between ~35 and 95%. Other dominant silicates are feldspars and phyllosilicates (micas or chlorite). The mineral grains are generally small (a few microns).

3. The estimated fluence level at the surface of the concrete biological shield facing the RPV ranges from 1.9 to 3.5×10^{19} n.cm^{-2} (E > 10 keV). The average fluence level is estimated at 1.8×10^{19} n.cm^{-2} (E > 0.1 MeV).

4. The estimated volumetric expansion of the aggregates at the irradiation conditions presented above in the test reactor is about 1%.

Path Forward

The susceptibility of irradiation-induced damage in concrete is governed by the exposure level (fast neutron fluence > 10^{19} n.cm^{-2} at E > 0.1 MeV) and the mineralogy of the aggregates (high quartz content and chemical heterogeneity of the assemblage). Both conditions are met for the SONGS concrete biological shield. The fast-neutron flux in test reactors is about 30 to 180 times higher than that in light-water reactors. The effects of flux reduction on the formation of the irradiation-induced damage rate in concrete constituents are not established. Hence, harvesting in-service irradiated concrete from the SONGS (unit 2 or 3) biological shield is an unparalleled opportunity to study the flux effects of neutron irradiation. Oak Ridge National Laboratory is developing a research plan for the harvesting, characterization, and companion modeling for irradiated SONGS concrete. This plan will be transmitted to the NRC in a separate document.

ABBREVIATIONS AND ACRONYMS

AI	artificial intelligence
ASR	alkali-silica reaction
BWR	boiling water reactor
CBS	concrete biological shield
CEA	Commissariat à l'Energie Atomique
CIWP	Cross, Iddings, Pirsson and Washington
CSH	calcium-silicate hydrate
DOE	US Department of Energy
EDS	energy dispersive x-ray spectroscopy
EDX	energy dispersive x-ray
EFPY	effective full-power year
EMDA	Expanded Materials Degradation Analysis
EPRI	Electric Power Research Institute
hcp	hardened cement paste
ICP	inductively coupled plasma
ICP-S	inductively coupled plasma spectroscopy
IMAC	Irradiated Minerals, Aggregates and Concrete
ITZ	interfacial transition zone
JCAMP	Japan Concrete Aging Management Program
MCNP	Monte Carlo N-Particle
MXRF	micro x-ray fluorescence
NPP	nuclear power plant
NRC	US Nuclear Regulatory Commission
OPC	ordinary Portland cement
PIE	post-irradiation examination
RCA	recycled concrete aggregaterac
RIVE	radiation-induced volumetric expansion
RH	relative humidity
RPV	reactor pressure vessel
R_{wp}	weighted profile R-factor
SCE	Southern California Edison
SDS	SONGS Decommissioning Solutions
SEM	scanning electron microscopy
SONGS	San Onofre Nuclear Generating Station
SLR	subsequent license renewal
SRM	Staff Requirements Memorandum
UPV	ultrasound pulse velocity
XRD	x-ray diffraction
XRF	x-ray fluorescence

1 INTRODUCTION

The effects of irradiation on concrete have been the subject of sustained research by the Electric Power Research Institute (EPRI), the US Nuclear Regulatory Commission (NRC), and the US Department of Energy (DOE) Light Water Reactors Sustainability Program (LWRSP) since 2011. This research is motivated by the need to inform the license renewal and long-term operation of US light-water reactors. To date, the effects of irradiation on concrete and its constituents are well understood when subjected to accelerated irradiation conditions in test reactors.

The concrete biological shields (CBSs) in light-water reactors are exposed to high neutron and gamma irradiations, potentially reaching levels for which degradation has been reported in the literature (i.e., $> \sim 10^{19}$ n.cm^{-2} at E > 0.1 MeV). At 80 years of operation, it is estimated that the bounding fluence approaches 6×10^{19} n.cm^{-2} (E>0.1 MeV), or about six times the potentially critical dose for irradiation-induced damage onset. The susceptibility of concrete against neutron irradiation greatly varies as a function of its constituents, including coarse aggregates, sand, and hardened cement paste (hcp). Higher irradiation susceptibility was found as a direct function of the aggregates' radiation-induced volumetric expansion (RIVE): that is, the propensity of swelling as a function of their mineral contents, structures, and textures. Irradiation-induced *amorphization*, also referred to as *metamictization*, is accompanied by significant swelling, especially in silicates [HIE78, DEN12, FIE15]. For example, the maximum volumetric expansion of quartz and feldspars—a group of rock-forming tectosilicate minerals that make up as much as 60% of the Earth's crust have been shown to be as large as ~18% and ~8%, respectively, whereas the change of density in calcite remains rather low (~0.3–0.5%). The main reason for higher swelling is the number of covalent bonds (Si-O) and the degree of polymerization of [SiO$_4$] tetrahedrons. Depending on the mineralogical content, considerable variations in aggregate RIVE have been observed [DEN12]. Moreover, some observed post-irradiation expansions exceed what is considered as detrimental by alkali-silica reaction (ASR) researchers. Because the CBS structural concrete is made of 70% of aggregates by volume, RIVE can impose severe stresses on the surrounding hcp, leading to microcracking, or even fracturing.

Gamma-irradiation primarily causes radiolysis of the water contained in concrete (free water, adsorbed water, and eventually, chemically bonded water). At doses under 100 MGy, no literature data indicate significant loss of mechanical properties [GRA71, MAR17].

The radiation field's strong attenuation produces a high RIVE gradient, causing high biaxial compressive elastic stresses in the vertical and hoop directions near the reactor cavity, and potentially causing elastic tensile hoop stresses toward the back of the CBS. Simultaneously, the prolonged moderate temperature exposure (< 65°C by design) and strong internal moisture content gradient affect the degree of concrete hydration, and thus, its mechanical properties leading to the development of lower strengths toward the reactor cavity. The dissipation of the RIVE-induced elastic stresses results from a competition between the development of cracking and potential relaxation in the hcp [GIO17]. Although the extent of radiation-induced concrete damage appears to be limited to a depth of about < 20 cm of the CBS, the consequences of this damage to the structural performance under seismic conditions (e.g., impact on RPV supports, or accident conditions, including a sudden increase of temperature in the cavity or seismic events) remain to be investigated. It must be noted that the estimated damage area extends beyond the inner layer of reinforcement and appears strongly oriented along parallel planes to

that layer, calling its ability to effectively transfer stresses into question based on the possible degradation of the steel–concrete bond [KAM20]. There are no data in the open literature on the effects of irradiation on the steel-concrete bond properties. A separate ongoing NRC-sponsored research activity entitled "Effects of irradiation on the bond strength of reinforced concrete" (2018–2023) aims at providing a set of initial data (scoping study) and addressing the significance of residual (post-irradiation) bond strength against the performance of the reinforced CBS.

Numerous gaps of knowledge still exist on the topic of irradiated concrete, which is comparative to other concrete aging mechanisms (e.g., corrosion or ASR) or the effects of irradiation on other metallic materials. Evaluation of the structural significance of irradiated CBS requires knowledge increase in the following areas:

1. **Rate effects**: Unlike the RPV steel, there is no surveillance program to assess the in-situ irradiated concrete. All irradiated concrete data were obtained in test reactors under accelerated conditions (high flux and often at higher temperature). The only option to assess the potential rate effect is to characterize harvested in-service concrete from decommissioned plants according to the conditions under which sufficient fluence levels were reached (> 10^{19} n.cm^{-2} at E > 0.1 MeV) and to determine whether the mineralogical composition of the concrete-forming aggregate exhibits significant silica content.

2. **Irradiated concrete–steel bond strength**: Because the RIVE-induced damage of concrete is expected to extend beyond the inner layers of reinforcement, and because possible neutron streaming may affect the RPV support shoe anchorages, evaluation of the irradiated concrete–steel bond strength is critical to determine the structural margin for accidental scenarios.

3. **Irradiated concrete creep and shrinkage**: Irradiated concrete cracking is driven by two factors: (a) the difference between aggregate's RIVE and the hcp shrinkage, and (2) the RIVE rate. RIVE causes high-stress concentration in the hcp. The dissipation of the stored elastic energy results either in hcp cracking or viscous deformation. In test reactors, the irradiation duration is limited and the RIVE rate is high, so significant viscous-type dissipation is not permitted. Very limited data on cement grouts suggest that irradiated hcp could be subjected to high creep rate. Collecting additional data is critical.

4. **Irradiated assisted alkali–silica reaction and irradiated-assisted corrosion**: These mechanisms have not been observed in situ to date, but research is needed to assess their potential. Irradiation-induced amorphization greatly increases the dissolution rate of silicate-bearing aggregate in a high alkali medium. Irradiation-induced radiolysis releases oxygen that can modify the redox condition around the steel reinforcement.

This project addresses item 1, rate effects. A preliminary study was performed to assess the opportunity for future harvesting of irradiated concrete cores from the under-decommissioning the San Onofre Nuclear Generating Station (SONGS). Harvesting opportunities are scarce, and the cost associated with handling radioactive materials is high. Therefore, the actual value and benefits of any harvesting campaign must be weighed carefully. Two criteria must guide this assessment. First, has the concrete been exposed to fast neutron fluence high enough to cause potential irradiation-induced damage? The comparison relies on damaging fluences in accelerated conditions such as > 10^{19} n.cm^{-2} at E > 0.1 MeV. Second, does the concrete aggregate contain minerals that are highly susceptible to irradiation damage, such as silicates?

Previous harvesting campaigns did not meet these two criteria. Boiling water reactors (BWRs) such as Hamaoka are typically exposed to doses on the order of 10^{18} n.cm^{-2} at E > 0.1 MeV. Likewise, the ORNL Graphite Reactor and the Jose Cabrera Nuclear Generating Station (Zorita, Spain) contained either baryte-haydite [BLO58] or highly calcareous aggregates.

This project describes the characterization of unirradiated concrete cores extracted from the walls of the steam generator room of SONGS Unit 2.

2 GEOLOGICAL FORMATION

The SONGS is located south of San Onofre, California, on the Pacific coast. The location of the aggregate quarry that supplied the aggregates for construction of both units could not be determined with certainty from the documentation provided by Southern California Edison (SCE). Two potential quarries have been suggested during the coordination meetings with the NRC, ORNL, SCE, and SDS: Santa Catalina Island, located directly west of SONGS, and San Juan Capistrano located about 15 miles north of SONGS. Although, the Santa Catalina Island quarry is located at a greater distance than the other possible inland quarries, Santa Catalina Island rocks were used to construct the Wheeler North Reef (SONGS Mitigation Reef) located 1.5 miles offshore from the city of San Clemente in 1999 (Phase 1) and 2008 (Phase 2).

Figure 2-1 shows that the Catalina Island quarry is located south of Jewfish Point in the Southeast tip of the island (Miocene [M] + Cretaceous and Jurassic sandstone of the Franciscan Complex [KJfs]). According to the geologic map of California (https://maps.conservation.ca.gov/cgs/gmc/) provided by the California Department of Conservation, the geological formation, including the quarry, appears to be a mix of (KJfs) blueschist and semi-schist of the Franciscan complex and (M) Miocene marine sandstone, siltstone, conglomerate, and breccia, moderately to well consolidated. It is designated as Miocene San Onofre breccia [STU79, ROW84, ALT97], a sedimentary rock composed of larger minerals (clasts) and rocks cemented together by a fine-grained matrix of similar or different origin. The rock facies of the quarry are quite complex [ROW84]. Three sedimentary units are "exposed [VED79] and intruded by Miocene dacitic and gabbroic dikes and sills." "The upper part. . . is a Miocene breccia" potentially associated with San Onofre breccia. "The clast composition. . .includes quartz schist, amphibolite, actinolite schist, tremolite(?) schist, talc schist, saussuritized gabbro, veined quartz, aphanitic (fine grain) to porphyritic (distinct grain size) siliceous metavolcanic rocks, porphyritic basalt, and feldspathic sandstone" [VED79]. "Two pre-middle Miocene units occur below the Miocene breccia," the lower part of which is "composed of interbedded siltstone, quartzofeldspathic sandstone and conglomerate. Lithic fragments are of granitic, volcanic and metamorphic origin, and they do not include detritus derived from the Catalina schist. Overlaying these marine sediments is a sequence of nonmarine redbeds consisting of sandstone, pebble-cobble conglomerate, and minor mudstone."

As mentioned above, the concrete aggregates may have been extracted from quarries located in the San Juan Capistrano area: Lapeyre Industrial Sands Inc. and Green Stone Materials still produce aggregate and sand from crushed stones. A third location could be considered: an abandoned quarry near the Prima Deschecha landfill. All three are located near Miocene marine sandstone, shale, siltstone, conglomerate, and breccia, with moderately to well consolidated formations. Near the two operating quarries, formations can be found such as alluvium, lake, playa and terrasse deposits (unconsolidated and semi-consolidated) and Eocene marine shale, sandstone, conglomerate and minor limestone (mostly well consolidated), as shown in Figure 2-2.
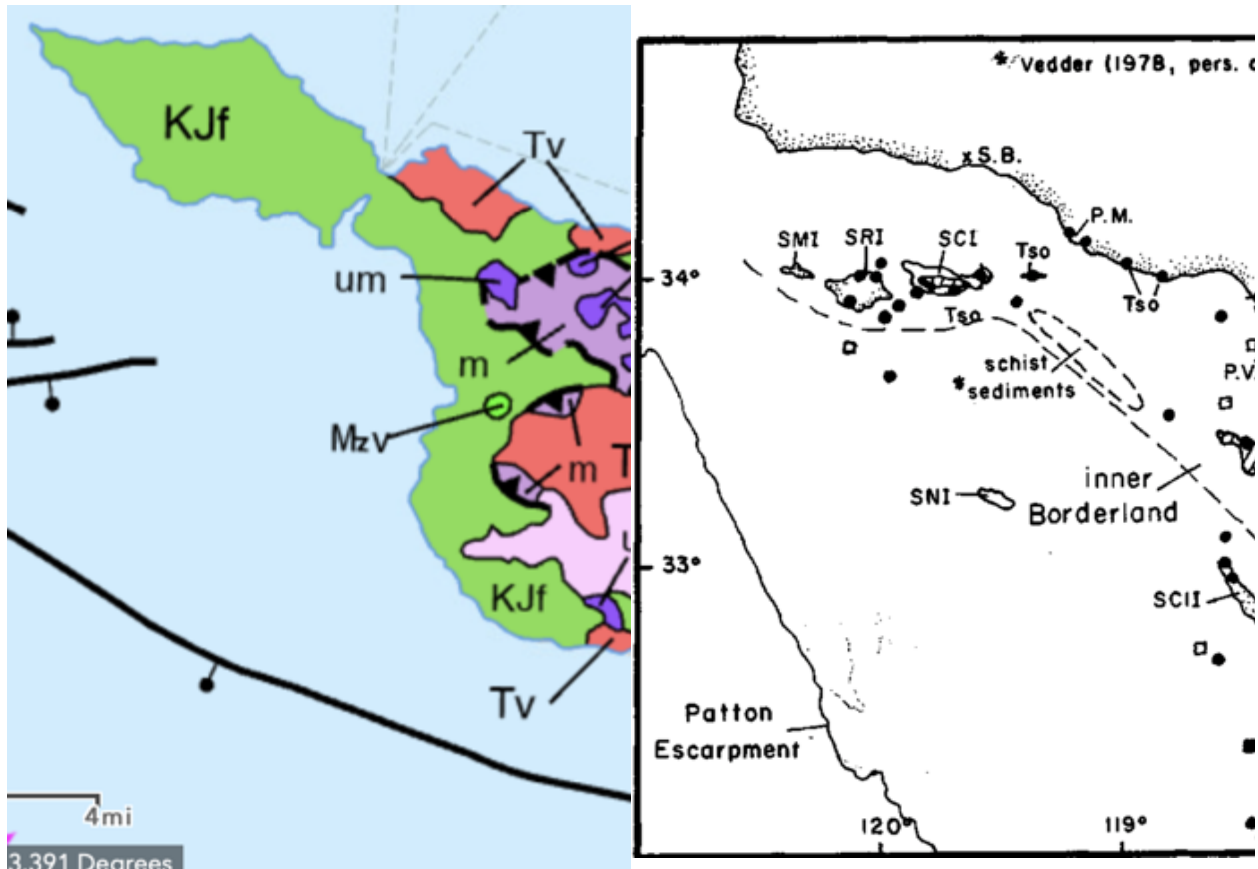
Figure 2-1   Left: Santa Catalina geological survey map (https://maps.conservation.ca.gov/cgs/gmc/). Right: (reproduced from [STU79]). Localities of bottom samples and outcrops of Catalina Schist-bearing sedimentary rocks, and outcrops of Catalina Schist. Modified from Vedder and Howell (1976, Fig. 1). Tso (Blue): San Onofre Breccia; CI: Santa Catalina Island, COR: Los **Coronados** Islands, SCI: Santa Cruz Island, SCLI: San Clemente Island, SMB: Sixty Mile Bank, SMI: San Miguel Island, SNI: San Nicolas Island, SRI: Santa Rosa Island, TFB : Thirty and Forty Mile Banks; L.A.: Los Angeles, L.B.: Laguna Beach, P.M.: Point Mugu, P.V.: Palos Verdes, Peninsula, S.B.: Santa Barbara, S.CL.: San Clemente, S.D.: San Diego, T.: Tijuana, O. : Oceanside. Orange: SONGS.
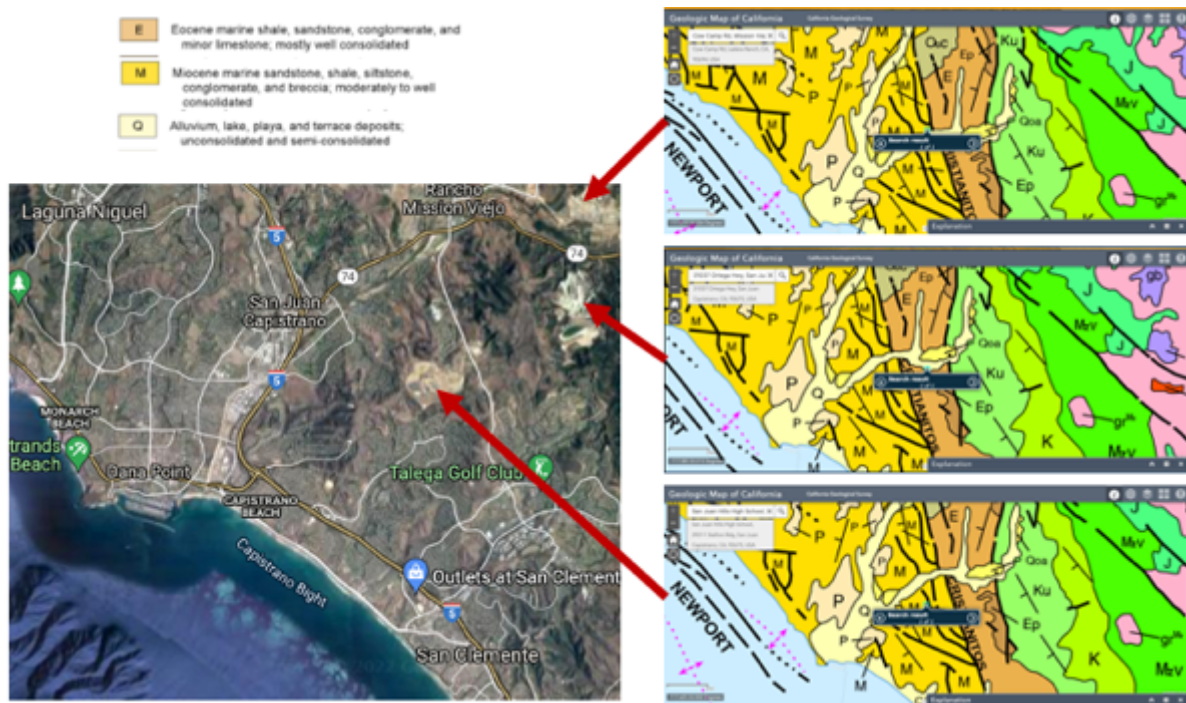
Figure 2-2 Location of two operating quarries and one possibly abandoned quarry in the San Juan Capistrano area. To the right: Corresponding geological survey maps (https://maps.conservation.ca.gov/cgs/gmc/) showing Miocene, Eocene, and alluvium formations.

Despite the lack of clear identification of the quarry used to extract the aggregates used for the construction of SONGS Units 2 and 3 in the late 1970s, it is likely that the aggregates contain a complex assemblage of shale (mudstone), San Onofre breccia, sandstone, and limestone, rich in varied silicates including quartz, plagioclase feldspar, felspathoid, clay, biotite, talc, and amphibole (hornblende, actinolite, tremolite).

3   CORED SPECIMENS

Three core samples were taken from SONGS Unit 2 the week of October 14, 2021 and were shipped to ORNL for characterization. The specimens were wrapped in plastic to avoid further dehydration and were received at ORNL on October 15, 2021.

The coring work was performed under SDS contract # DWP SDS-2-C-CO-1788.

The specimens were taken from outside of Steam Generator Room 2 (106) on the north wall of the primary shield at elevations of 45, 30 and 17 feet. Coring locations are provided in Appendix A. It is expected that the same aggregates were used to construct the CBS around the RPV.

Each specimen is labeled according to the coring elevation: SONG-PS-17, SONG-PS-30, and SONG-PS-45. All cores are 3 inches in diameter, and their lengths vary with the elevation. Except for specimen SONGS-PS-45 (see comment below), the specimens are sound. The quality of the concrete appears to be sound because the adhesion between the paste and the aggregates looks good. Some millimeter-size air bubbles are visible, which is common for in-situ vibrated concrete. The shapes of the aggregate appear mostly rounded. Some aggregates exhibit elongations. The nature of the aggregates seems quite heterogeneous, with the presence of dark gray homogenous aggregates, blueish, greenish, yellowish, and whitish aggregates. The fractured surface (back end of the core) shows either aggregate separation from the paste or intra-aggregate fractures. Visually, the maximum aggregate size appears to be approximately 3–4 cm.

SONGS-PS-17 (Figure 3-1): The length of the specimen is about 9 in. The specimen appears to be intact.
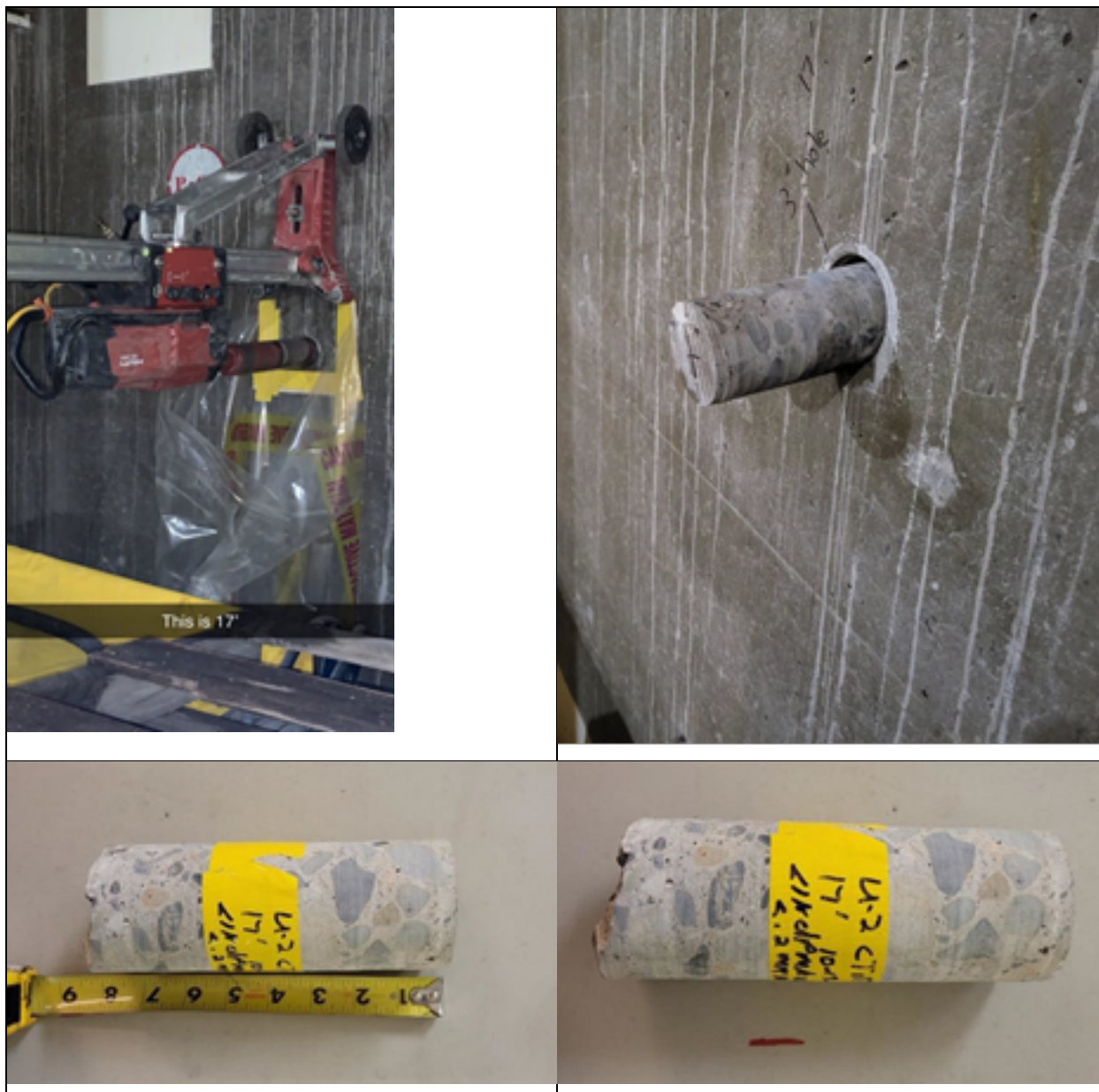
Figure 3-1. Cored specimen at 17 ft elevation

SONGS-PS-30 (Figure 3-2): The length of the specimen is about 8.5 in. The specimen appears to be intact.

Figure 3-2   Cored specimen at 30 ft elevation

SONGS-PS-45 (Figure 3-3): The length of the specimen is about 6.5 in. The specimen is cracked from the outer surface to about ¾ of the length of the specimen at an angle of about 20 degrees from the axis of the core. The crack is visible to the naked eye. There is concern that this part may split when the specimens are sawed.

Figure 3-3   Cored specimen at 45 ft elevation

4 MATERIALS CHARACTERIZATION

4.1 Ultrasound Pulse Velocity

The specimens were cut with a blade saw (GEOCUT) to obtain a flat surface. The lengths were measured with a caliper. The P-wave (UPVs) were measured using a Proceq Pundit PL-200 instrument provided by EPRI. Olympus Couplant-D was used to ensure wave transmission between the transducer, the receiver, and the concrete. The transducers were zeroed using the calibration rod provided (25.4 μs). The signal frequency was 54 kHz (standard value). The measurements were taken at laboratory temperature between 10 and 30°C (no correction). The pulse velocities are given in Table 4.1.

Table 4-1   P-wave velocities

Specimen	Length (mm)	Velocity (m/s)	Dynamic modulus* (GPa)	Compressive strength** (Mpa)
SONGS-PS-17	168.9	4,721	44.6	52.8
SONGS-PS-30	174.1	4,860-4,874	47.2-47.5	61.3-62.2
SONGS-PS-45	131.1	4,645	43.1	48.6

Estimates (See equation in text).
Empirical equation: $fc \approx (V/2{,}178.71)/0.1949$.

Pulse wave velocity is a nondestructive technique that provides an indirect measurement of the dynamic elastic properties of a material. ASTM C597-09 defines how the technique is used for concrete. The relation between the pulse velocity V and the (isotropic) dynamic properties E_{dyn} (modulus) and v_{dyn} (Poisson's ratio) is given by

$$V = \sqrt{\frac{E_{dyn}(1-v_{dyn})}{\rho(1+v_{dyn})(1-2v_{dyn})}}, \tag{1}$$

where ρ is the density of the material. Assuming that the density of the concrete is 2.4 g.cm^{-3} and the dynamic Poisson's ratio is 0.25, the corresponding dynamic moduli's estimates range between 43 and 47.5 GPa (Table 4-1). The compressive strength estimates are provided for information only using an empirical correlation equation that is subject to important uncertainties caused by the concrete mix composition, the varied curing condition and test methods.

Preparation of samples for petrography and micro-XRF and aggregate extraction

The core SONGS-PS-17 was sliced for petrography and micro-XRF (MXRF) characterization, and the remainder of the core was used for aggregate extraction. Figure 4-1 shows the slices and surfaces used for subsequent analyses. The three slices for MXRF were cut in half to ease polishing on the chosen surfaces. Surface number 4 broke during polishing, so x-ray fluorescence (XRF) was not completed on this surface. The slices used for petrography were sent to Spectrum Petrographics to be prepared as thin sections of 30 μm on 2 × 3-inch. The surfaces from which the thin sections were prepared approximately match the surfaces chosen for XRF (Figure 4-2).
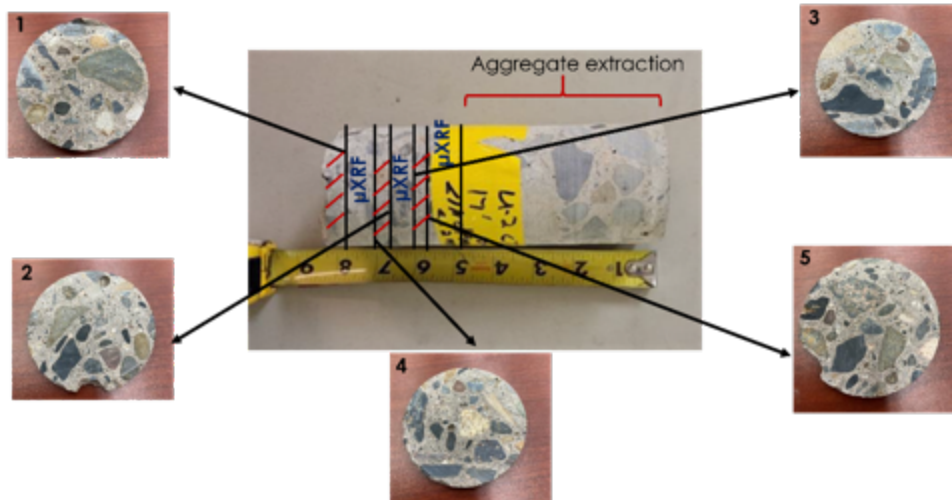
Figure 4-1 Schematic of the slices cut for petrography and MXRF of the core from SONGS-PS-17 showing the five surfaces of interest extracted at 17 feet of elevation. Red lines indicate pieces used for preparation of thin sections; the remaining part of the core was used for aggregate extraction
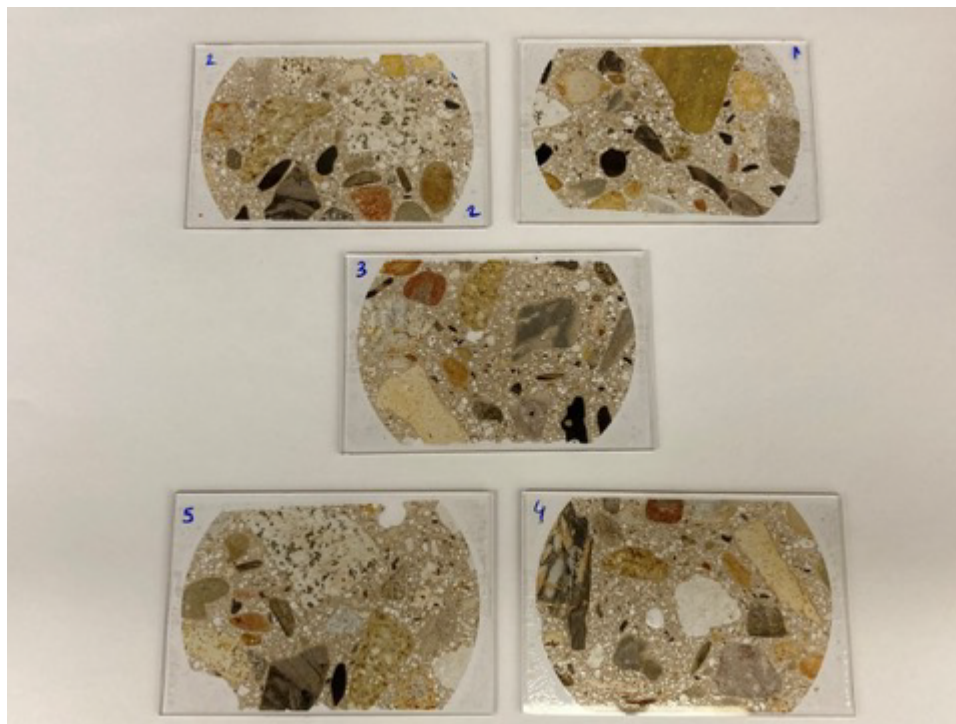
Figure 4-2 Thin sections prepared from five surfaces of the core from SONGS-PS-17

4.2 Micro XRF

MXRF elemental maps were collected on surfaces 1, 2, 3, and 5 using an Atlas system (iXRF instruments) operated under vacuum at 50 kV and 600 µA with a spot size of 10 µm. The map dimensions were 45 × 45 mm with a resolution of 1,500 pixels, and a pixel size of 30 µm. The

dwell time was 300 msec, and the time constant was 1. Seven elements (Al, Ca, Fe, K, Mn, S, Si) were analyzed for consistency throughout the core. Figures 4-3 and 4-4 show the elemental maps that serve as the basis for the statistical analysis of the samples.
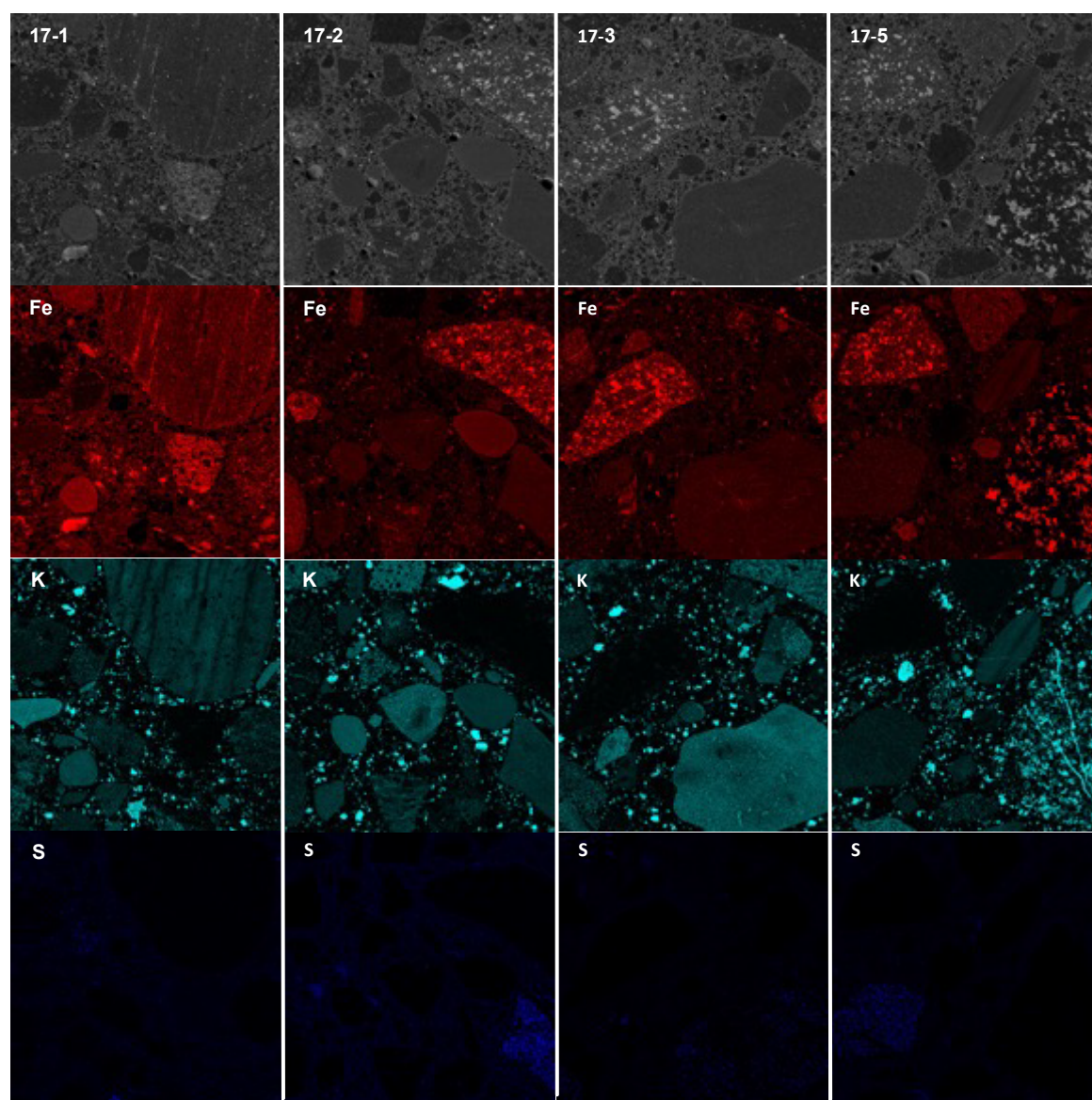
Figure 4-3   Element intensity maps of iron, potassium, and sulfur
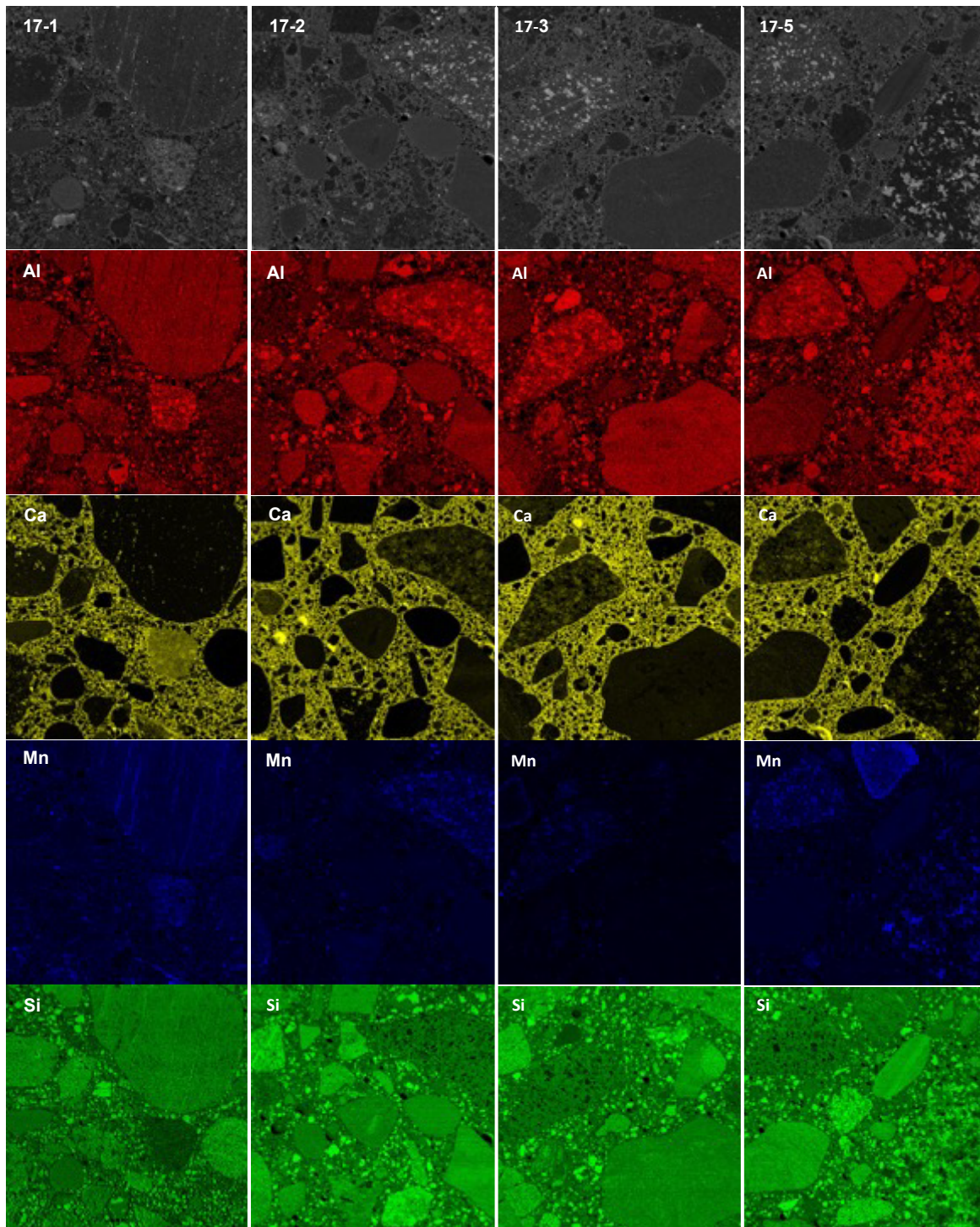
Figure 4-4   Element intensity maps of aluminum, calcium, manganese, and silicon

Each pixel is assigned an intensity value, and then each instance of that intensity is counted, resulting in a histogram. Figure 4-5 shows the resulting histograms for calcium and iron. For each sample, the mean values, standard deviations, and skewness were calculated for each

element. Table 4-2 shows the mean count value of each element for each sample and then the mean, standard deviation, and skewness across the core length.
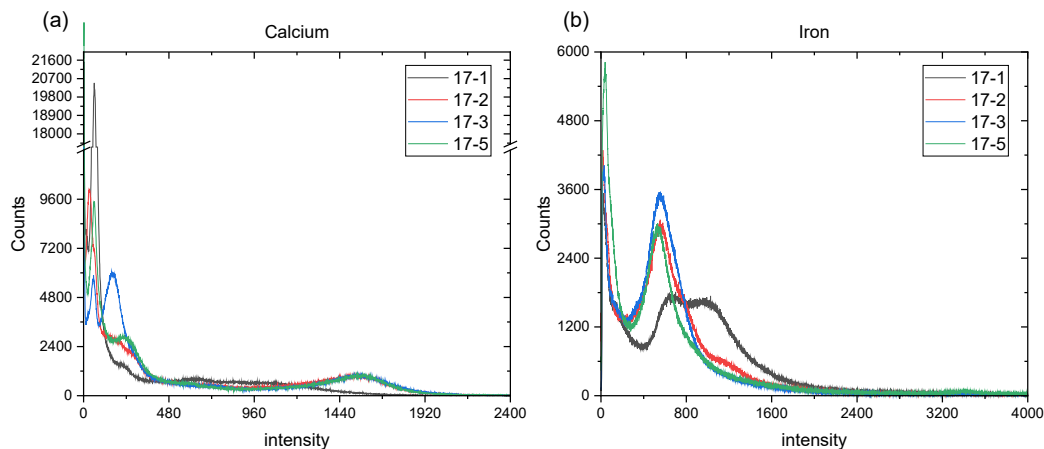
Figure 4-5   Intensity histograms: (a) calcium and (b) iron

Table 4-2   Mean count values for each sample and element

	17-1	17-2	17-3	17-5	mean	st dev	skew
Aluminum	14,705.9	34,615.4	40,909.1	39,473.7	32,426.0	12,116.5	-1.7
Calcium	523.7	438.2	489.6	458.6	477.5	37.4	0.4
Iron	207.1	234.0	238.7	229.3	227.3	14.0	-1.6
Potassium	697.5	1,759.2	2,252.3	1,901.9	1,652.7	669.7	-1.4
Manganese	808.8	912.8	590.1	954.2	816.5	162.8	-1.2
Sulfur	5,079.0	3,839.6	2,098.9	2,317.2	3,333.7	1,397.6	0.6
Silicon	2,388.5	2,656.4	4,032.3	3,138.1	3,053.8	722.3	1.0

In general, the mean values for the different slices are relatively similar, except for sample SONGS PS 17-1, which shows large deviations for Al, K, and S (see Figure 4-6). It should be noted that the count values do not reflect the volume percentages of each element in the sample, but they are a general comparison of the overall inclusion of each element. The standard deviation shows that calcium, iron, and silicon are the most consistent elements across the core, whereas sulfur and aluminum are the most varied, and potassium and manganese are also relatively consistent.
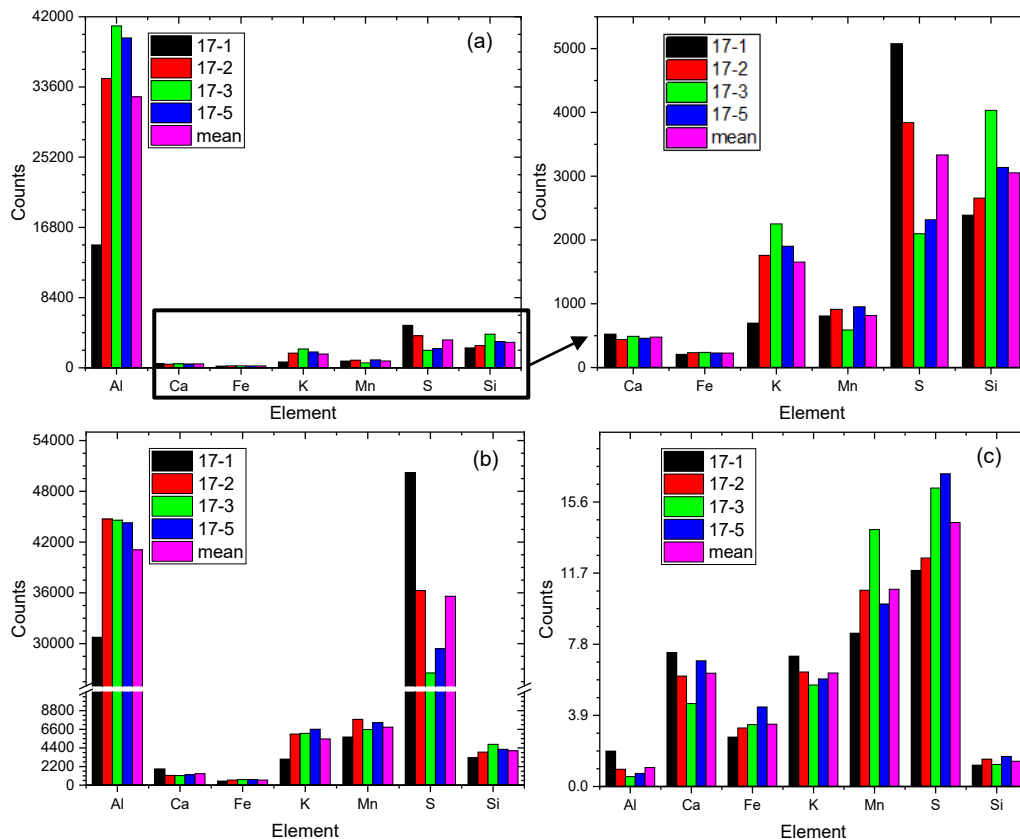
Figure 4-6   Statistical analysis of XRF data: (a) mean count values, (b) standard deviation of counts in each sample, and (c) skewness of counts across the samples

Finally, all elements show a positive skewness, with aluminum and silicon having the closest to a normal distribution across the samples, whereas all other elements show a higher tendency to have highly concentrated locations within the sample, thus creating the larger right skews. Overall, because concrete is a composite material created from cement paste and aggregates, which are composites themselves, the core shows consistency throughout its length. Samples from other cores may undergo future testing to determine the consistency throughout the structure height, as well as further analysis of the XRF data to compile the percentage of each element in the samples.

4.3 Petrography

Petrographic images of the thin sections were taken to qualitatively assess the mineral phases present in the aggregates. The work was performed using a Nikon D700 camera attached to an Olympus BX60 optical microscope. Images were taken at magnifications from 1.25 to 20× under transmitted light with crossed and uncrossed polarizers and under reflected light.

The results of the exploration of aggregates in the thin sections indicate a variety of altered rocks with igneous (granite), volcanic, and sedimentary (shale) origins. The predominant identified minerals are as follows:

Quartz
Feldspars (altered and unaltered)
Plagioclase feldspar
Amphiboles (blue and green)
Epidote
Iron oxides: hematite, biotite, and possibly ilmenite
Pyrite
Pyroxene
Olivine
Chlorite
Clay
Muscovite
Sericite
Sericitic mica
Serpentine
Organic materials

The fine aggregates showed a composition that was similar to the larger aggregates, although less alteration was present (Appendix B). Crystal precipitation was observed in some bubbles present in the cement paste (Figure 4-13). Further study of some of the areas in thin section 1, including the bubbles, was performed using advanced SEM quantitative methods to identify phases based on chemical composition.
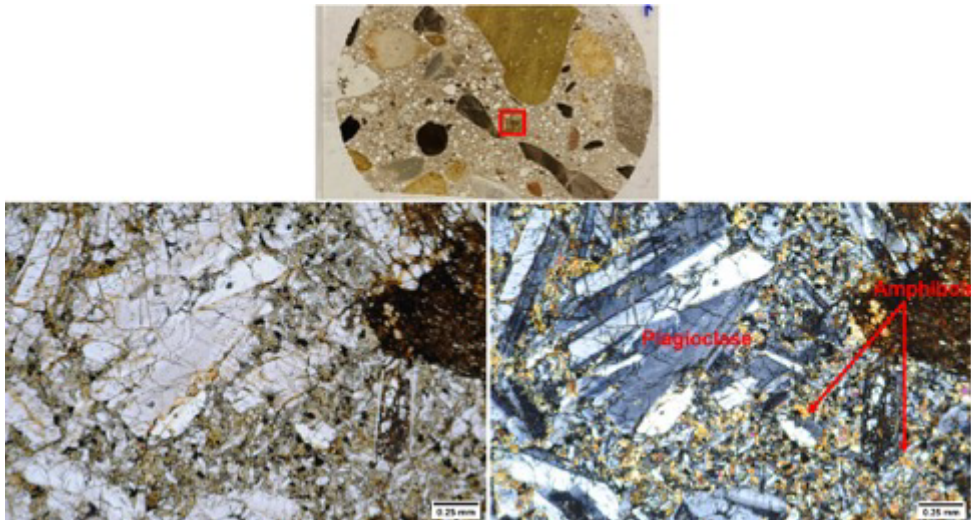
Figure 4-7   Petrographic images with uncrossed (left) and crossed polarizers (right) taken in the area marked with a red rectangle
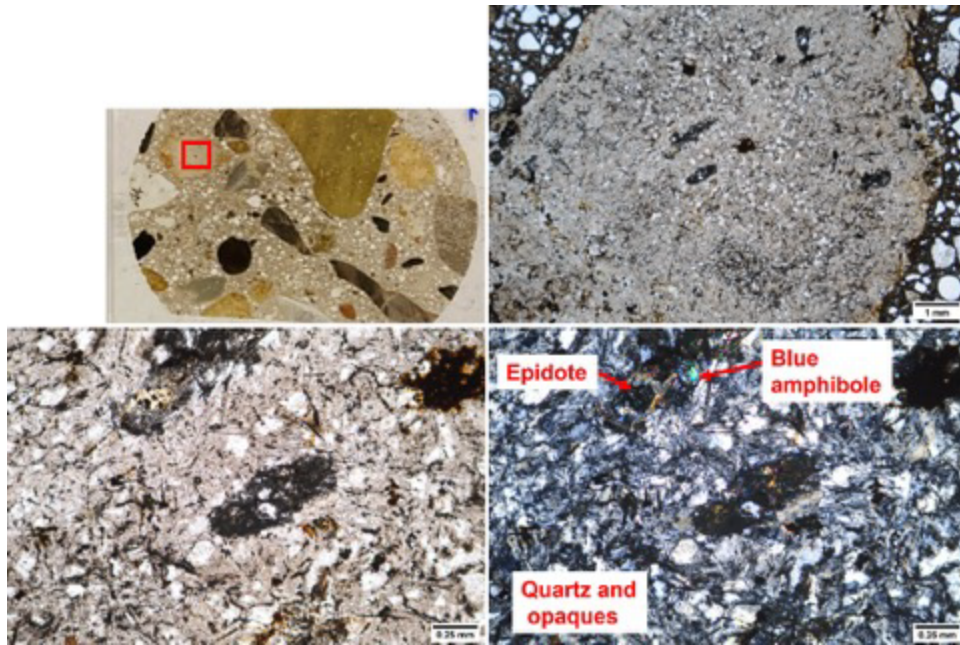
Figure 4-8   Petrographic images with uncrossed (top right and bottom left) and crossed polarizers (bottom right) taken in the aggregate marked with a red rectangle
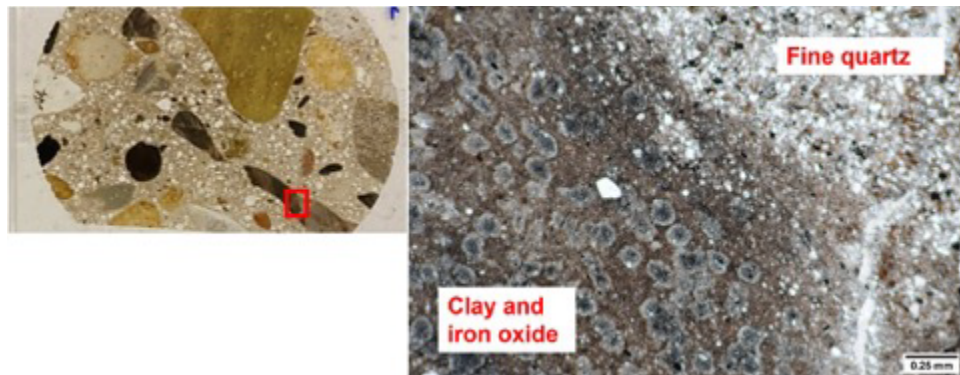
Figure 4-9   Petrographic image with crossed polarizers taken in the area marked with a red rectangle
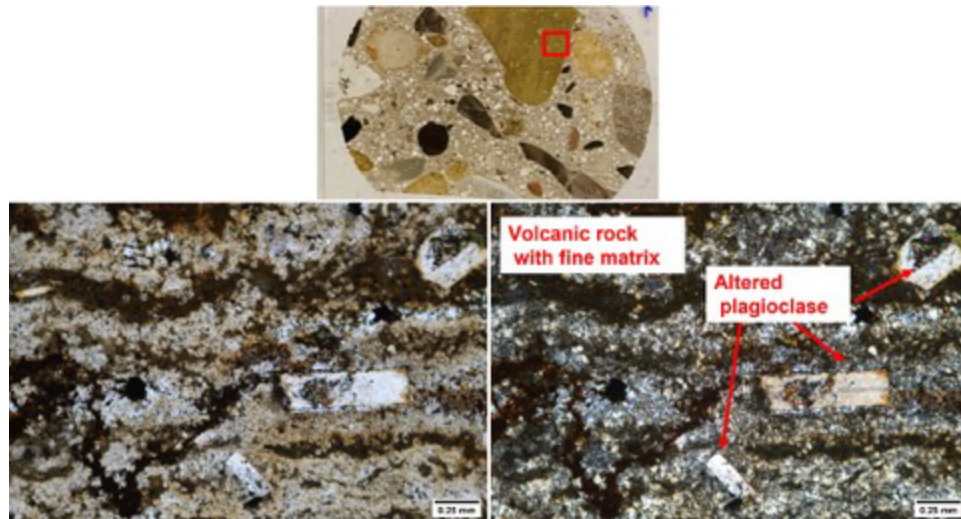
Figure 4-10   Petrographic image with uncrossed (left) and crossed polarizers (right) taken in the area marked with a red rectangle
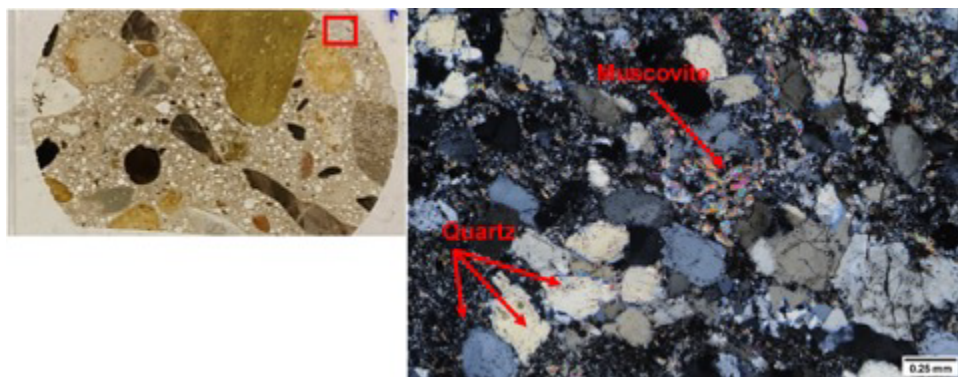
Figure 4-11   Petrographic image with crossed polarizers taken in the area marked with a red rectangle
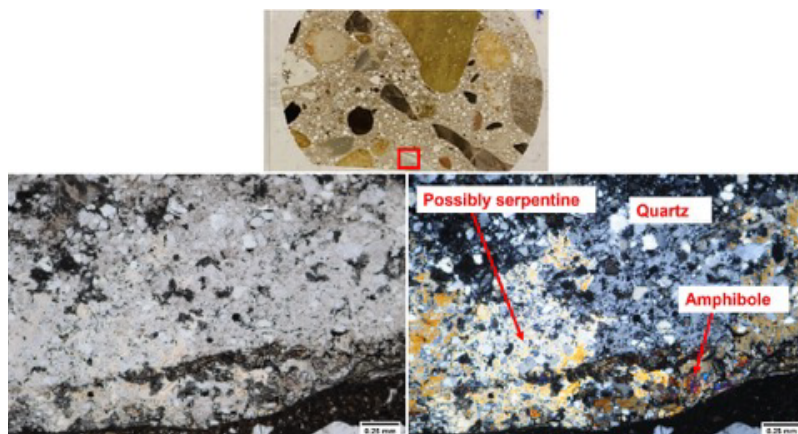
Figure 4-12   Petrographic images with uncrossed (left) and crossed polarizers (right) taken in the area marked with a red rectangle

19
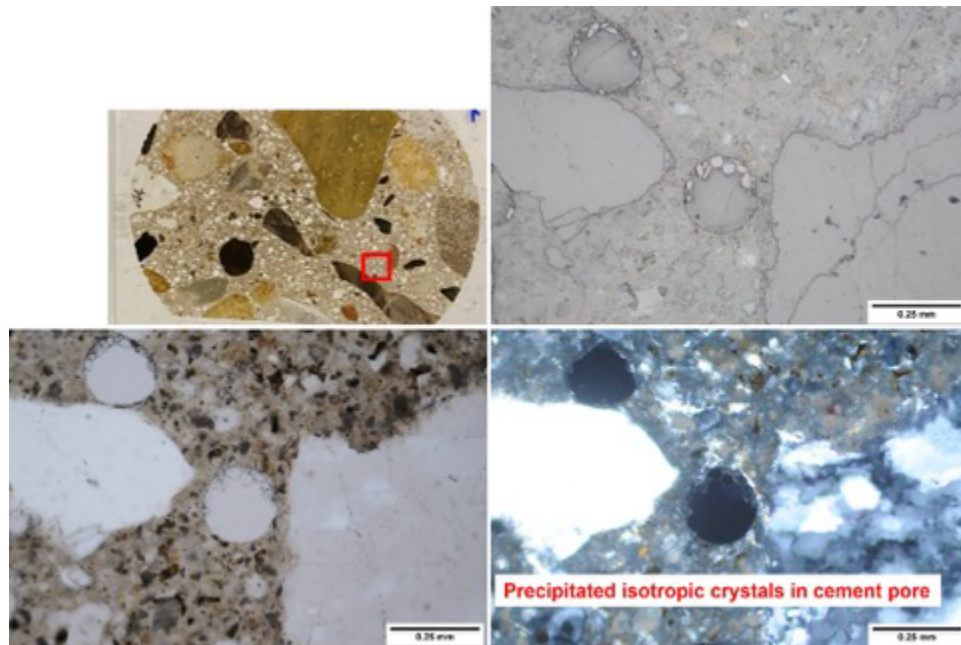
Figure 4-13 Petrographic images taken under reflected light (top right), under transmitted light with uncrossed (bottom left) and crossed polarizers (bottom right) showing an air bubble in cement paste with precipitated crystals around the edge
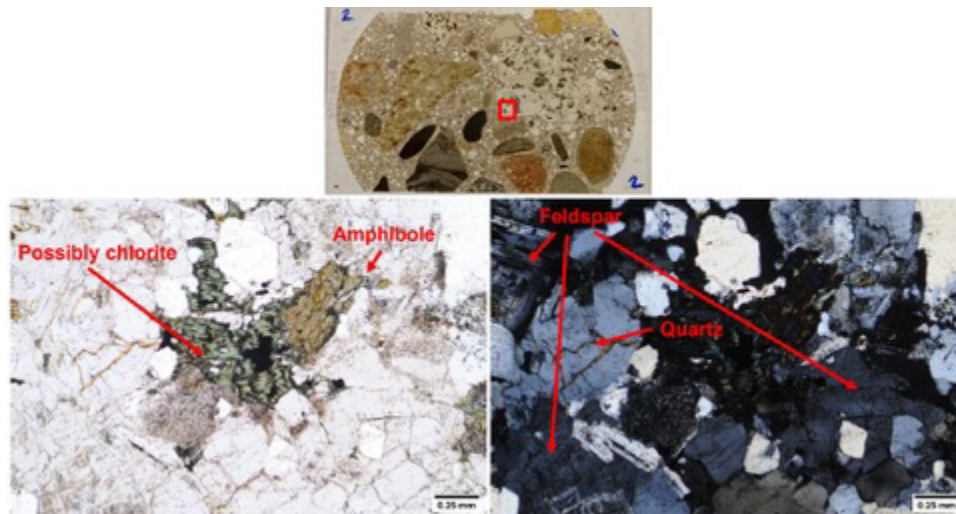
Figure 4-14 Petrographic images with uncrossed (left) and crossed polarizers (right) taken in the aggregate marked with a red rectangle
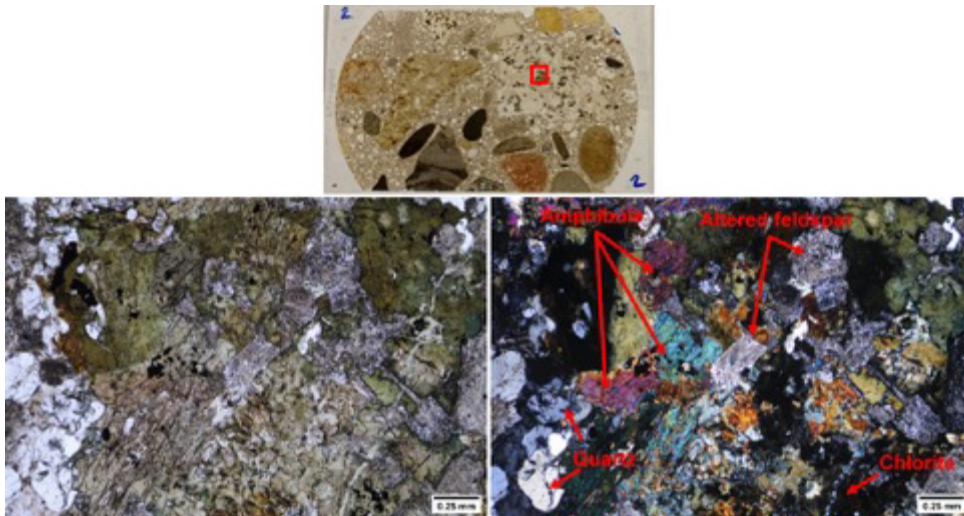
Figure 4-15 Petrographic images with uncrossed (left) and crossed polarizers (right) taken in the area marked with a red rectangle
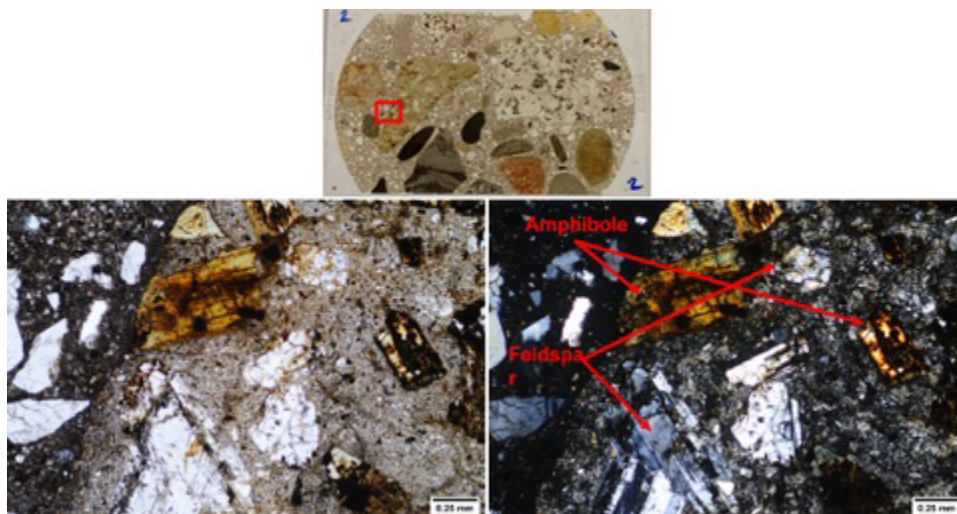
Figure 4-16 Petrographic images with uncrossed (left) and crossed (right) polarizers taken in the area marked with a red rectangle
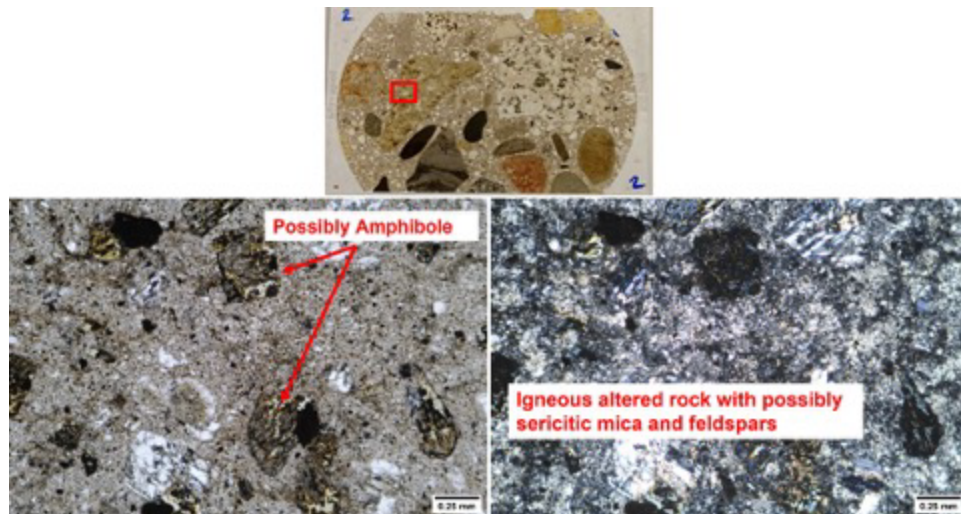
Figure 4-17 Petrographic images with uncrossed (left) and crossed polarizers (right) taken in the area marked with a red rectangle
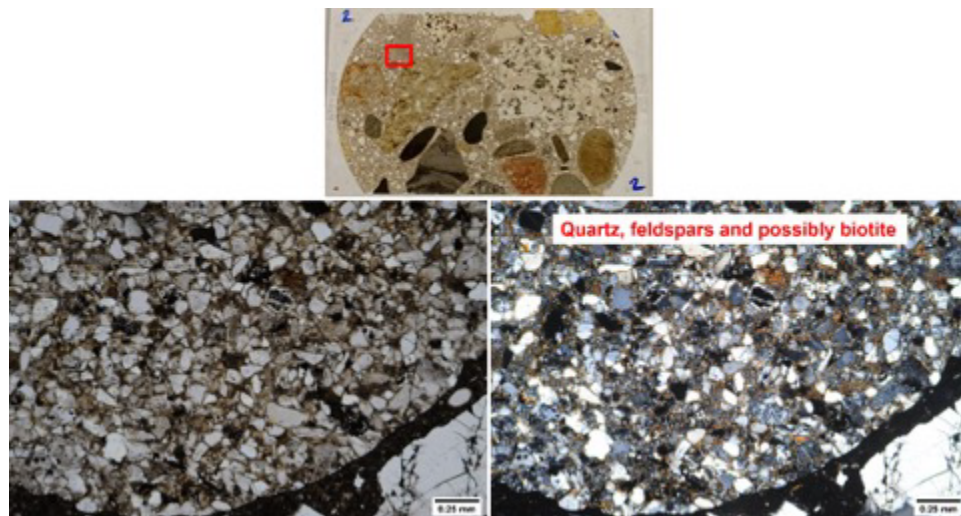
Figure 4-18 Petrographic images with uncrossed (left) and crossed polarizers (right) taken in the area marked with a red rectangle
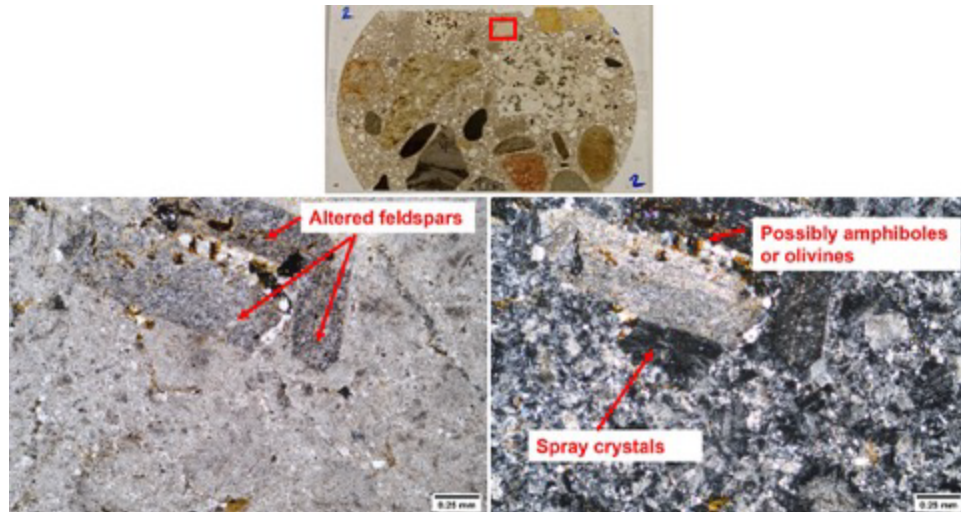
Figure 4-19 Petrographic images with uncrossed (left) and crossed polarizers (right) taken in the area marked with a red rectangle
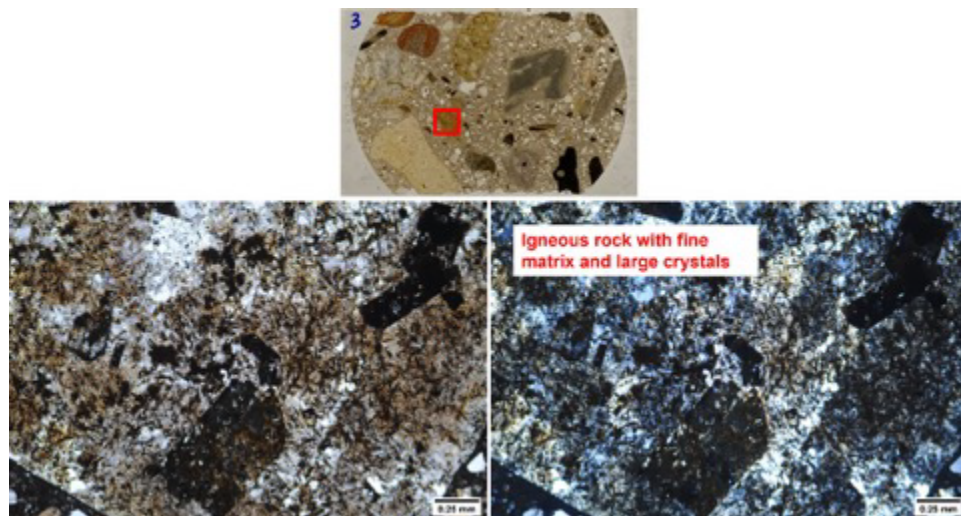
Figure 4-20 Petrographic images with uncrossed (left) and crossed polarizers (right) taken in the area marked with a red rectangle
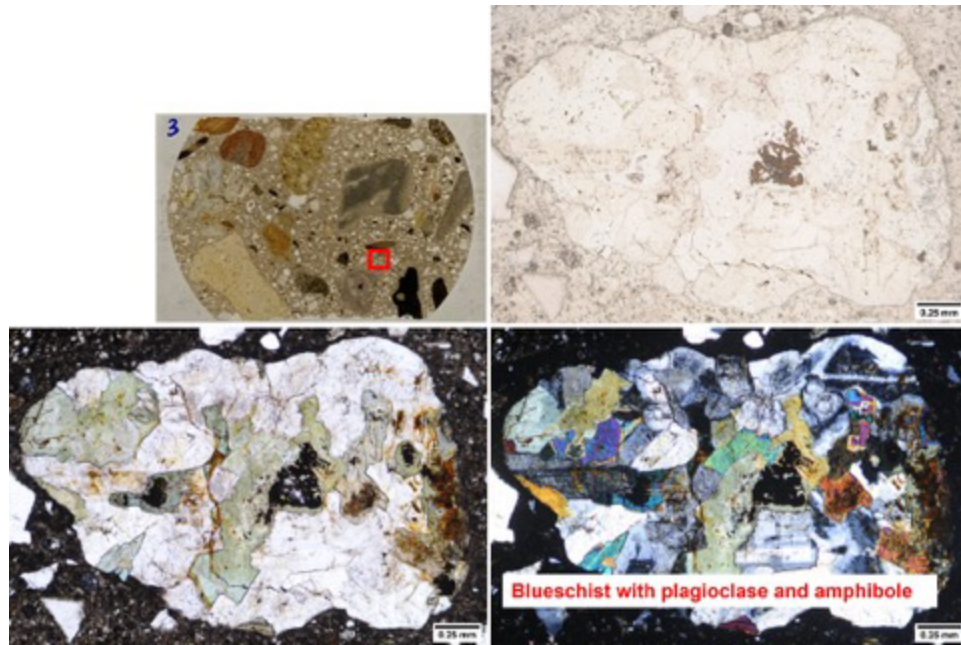
Figure 4-21 Petrographic images under reflected light (top right), under transmitted light with uncrossed polarizers (bottom left), and crossed polarizers (bottom right) taken in the area marked with a red rectangle
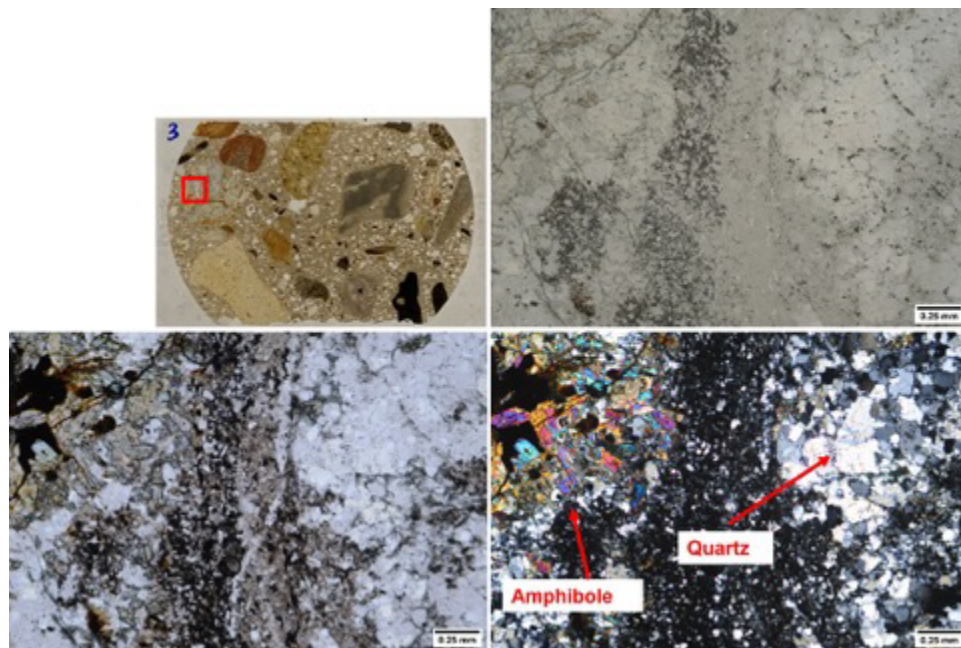
Figure 4-22 Petrographic images under reflected light (top right), under transmitted light with uncrossed polarizers (bottom left), and crossed polarizers (bottom right) taken in the area marked with a red rectangle
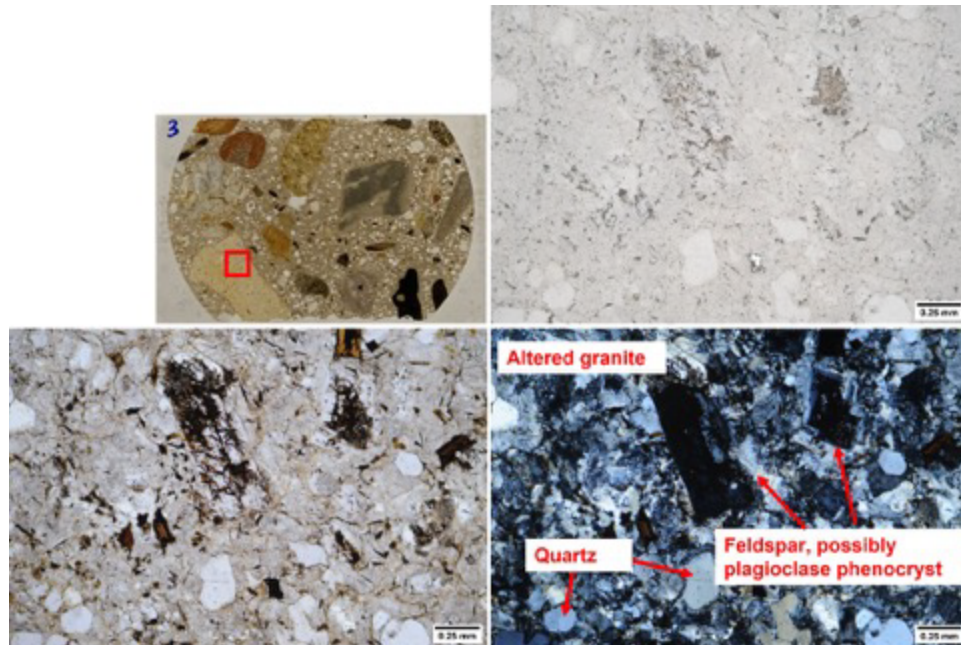
Figure 4-23 Petrographic images under reflected light (top right), under transmitted light with uncrossed polarizers (bottom left), and crossed polarizers (bottom right) taken in the aggregate marked with a red rectangle
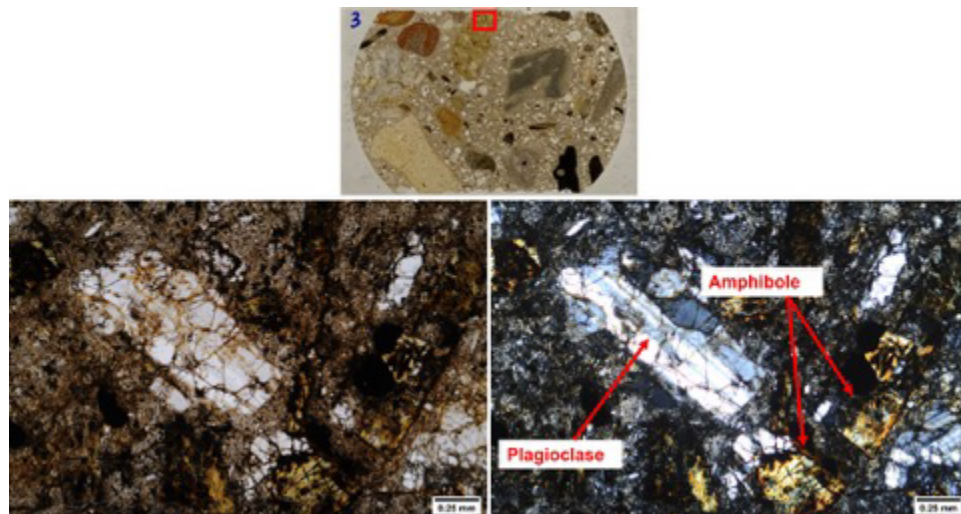
Figure 4-24 Petrographic images with uncrossed (left) and crossed polarizers (right) taken in the area marked with a red rectangle
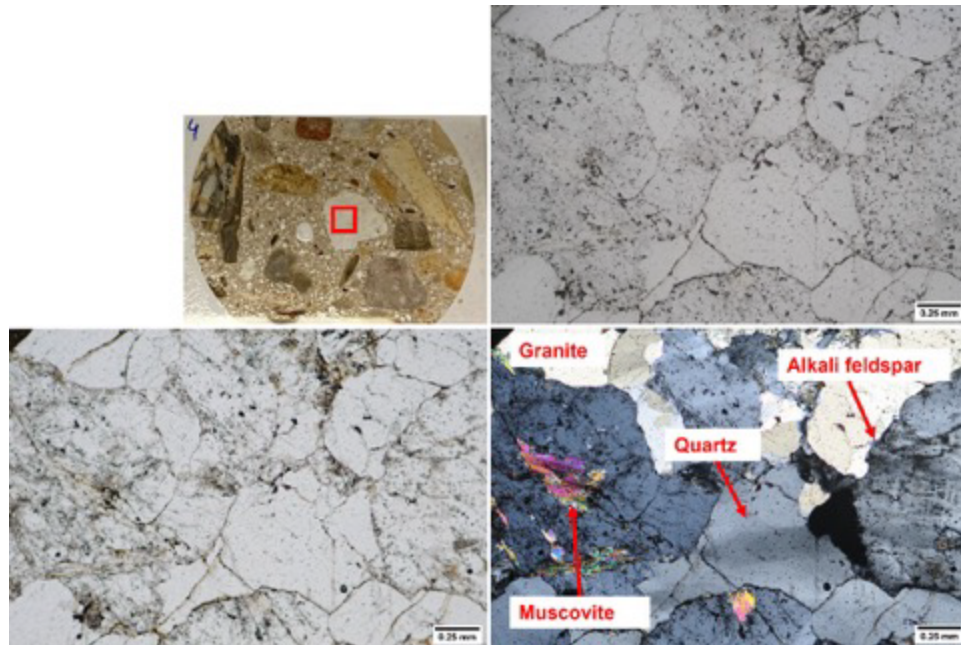
Figure 4-25 Petrographic images under reflected light (top right), under transmitted light with uncrossed polarizers (bottom left), and crossed polarizers (bottom right) taken in the aggregate marked with a red rectangle
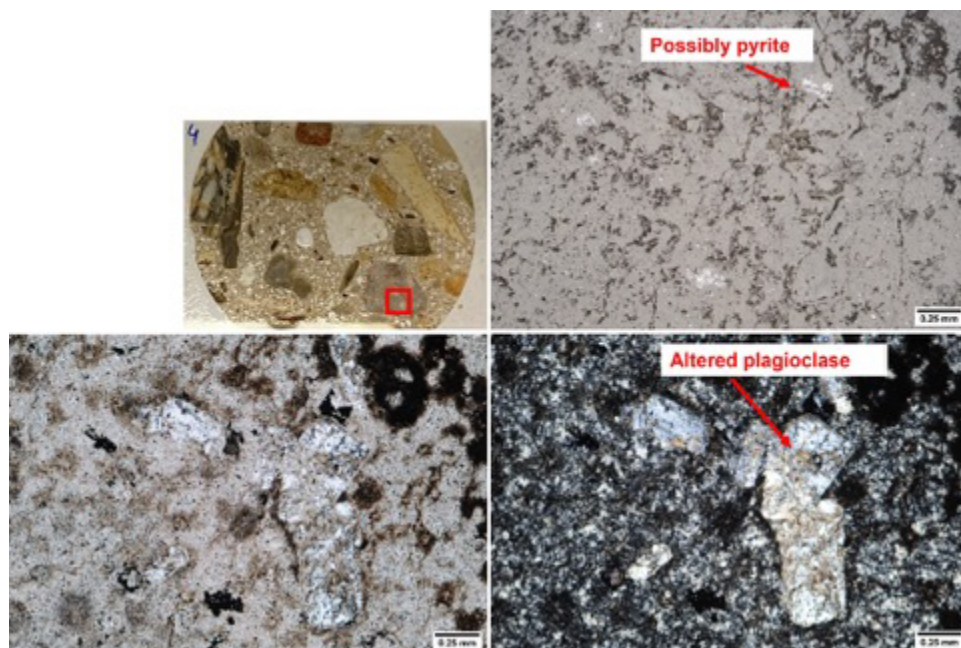
Figure 4-26 Petrographic images under reflected light (top right), under transmitted light with uncrossed polarizers (bottom left), and crossed polarizers (bottom right) taken in the aggregate marked with a red rectangle
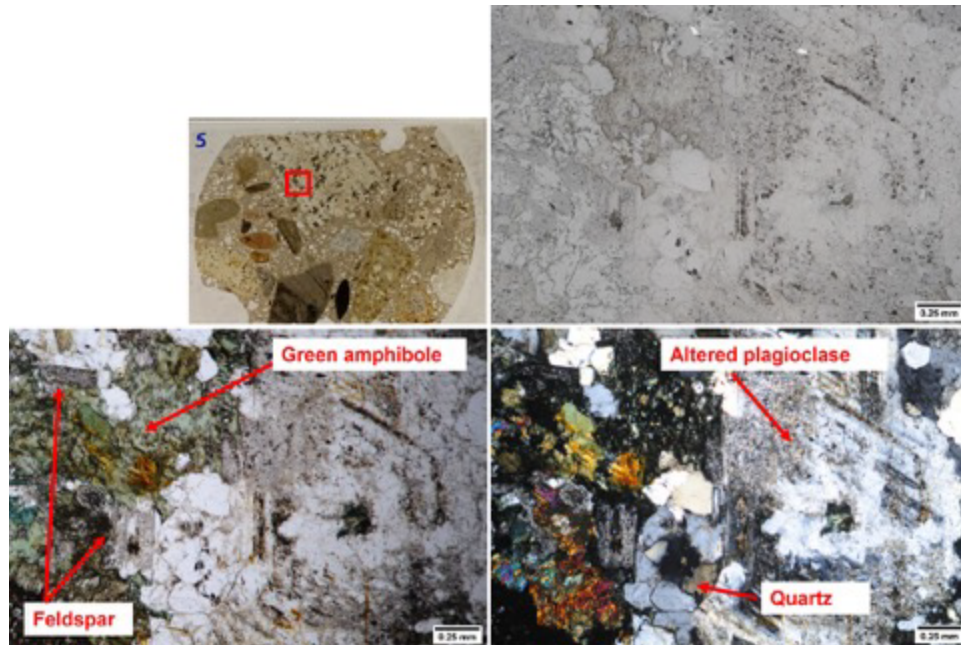
Figure 4-27 Petrographic images under reflected light (top right), under transmitted light with uncrossed polarizers (bottom left), and crossed polarizers (bottom right) taken in the aggregate marked with a red rectangle
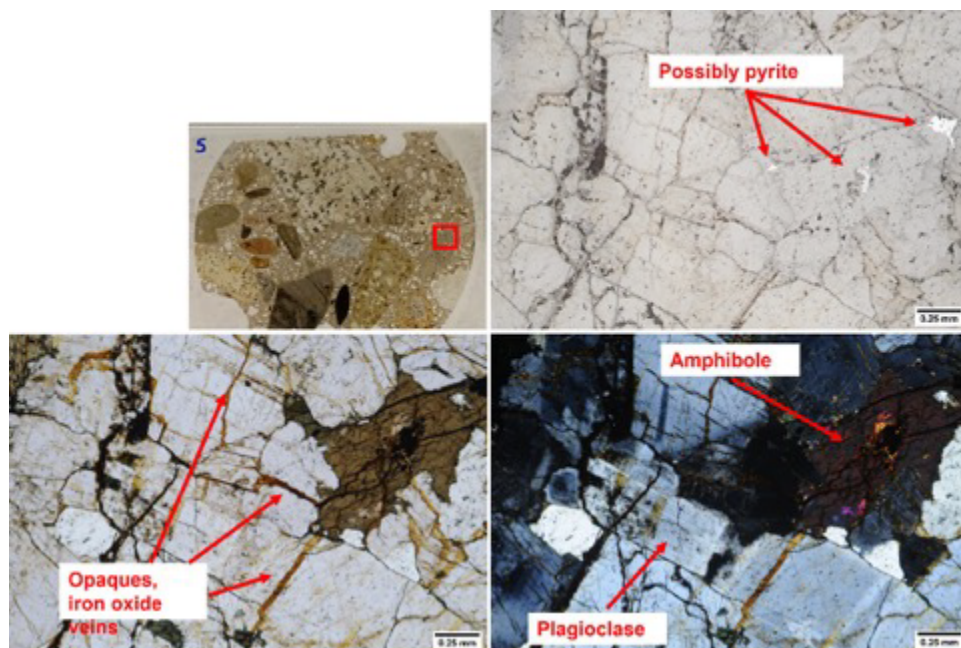
Figure 4-28 Petrographic images under reflected light (top right), under transmitted light with uncrossed polarizers (bottom left), and crossed polarizers (bottom right) taken in the aggregate marked with a red rectangle
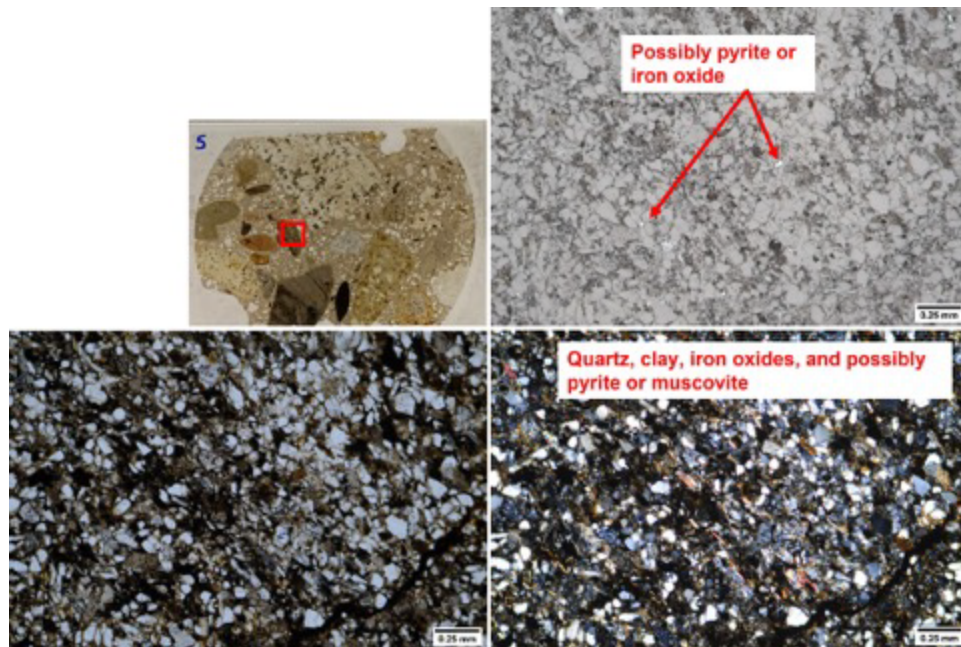
Figure 4-29 Petrographic images under reflected light (top right), under transmitted light with uncrossed polarizers (bottom left), and crossed polarizers (bottom right) taken in the aggregate marked with a red rectangle
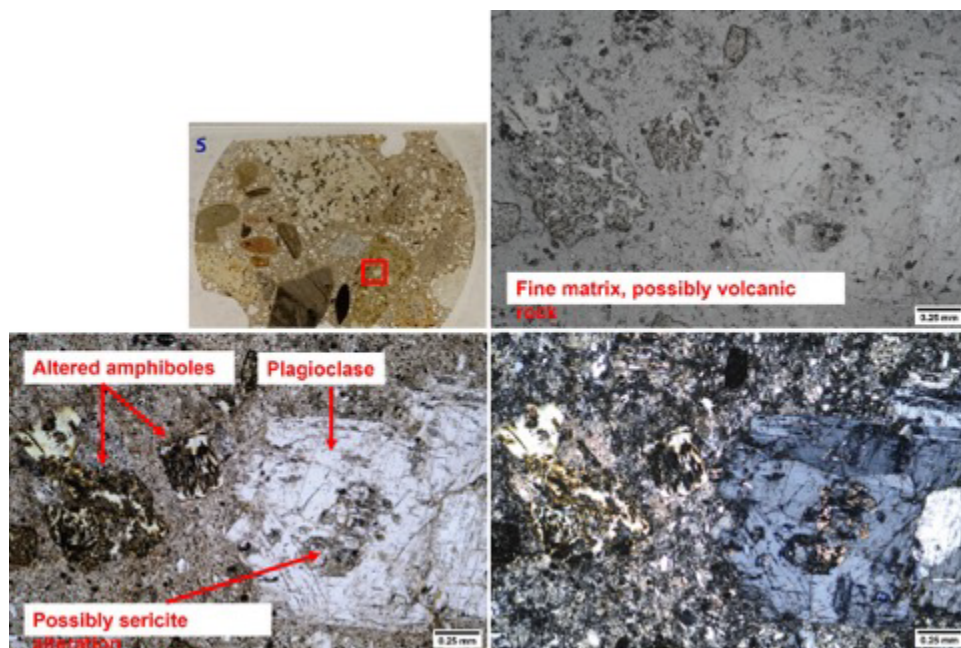
Figure 4-30 Petrographic images under reflected light (top right), under transmitted light with uncrossed polarizers (bottom left), and crossed polarizers (bottom right) taken in the aggregate marked with a red rectangle
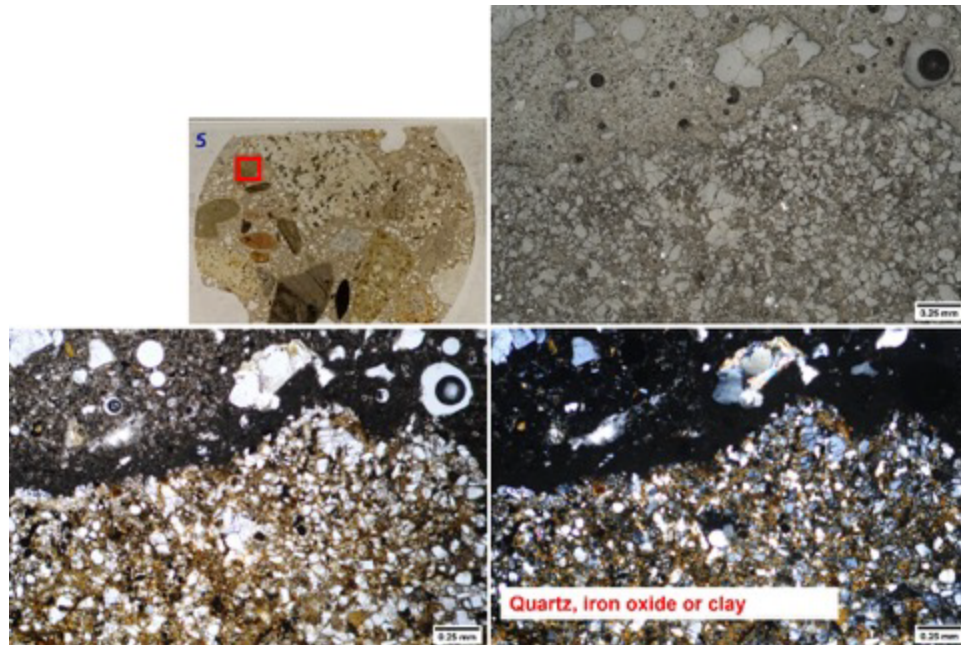
Figure 4-31   Petrographic images under reflected light (top right), under transmitted light with uncrossed polarizers (bottom left), and crossed polarizers (bottom right) taken in the aggregate marked with a red rectangle

4.4 QEMSCAN Mineral Maps

Selected areas of the thin section 1 were studied using quantitative analysis of minerals by SEM (QEMSCAN) to obtain mineral phase maps in areas of 1 to 2 mm^2. QEMSCAN is an FEI software trained by artificial intelligence (AI) with thousands of standards that can be used to identify mineral phases.

The first aggregate explored is shown in the petrographic images in Figure 4-10. Three areas were explored in this aggregate, and the resulting QEMSCAN maps with percentages of identified phases are shown in Figures 4-32 through 4-34. This volcanic rock has a silica-rich (matching quartz and albite standards) fine-grained groundmass of crystals and/or glass with larger phenocrysts of mostly albite. K-feldspar and apatite occur as inclusions within the albite phenocrysts. In these fields, "Ca-plagioclase" appears mainly as rims around albite phenocrysts and at the epidote and sphene (titania) margins, so these pixels likely represent a grain boundary phase that is a mix of albite and other Ca-silicates. Amphibole also rims epidote, and locations with only a few pixels are also interpreted as grain boundary mixtures. Muscovite forms fine grains, some barely larger than a few pixels, and it is associated with the Al-Silicate trap standard in these fields. Stringers of dark material observed in the petrographic images in Figure 4-10 seem to mainly match the Al-Silicate trap and Fe-oxide/clay (Limonite-clay interface) definitions, which are interpreted to be alternating bands of clay and Fe-oxyhydroxides. The kaolinite definition is associated with the limonite/clay interface and is therefore grouped with it. "Ilmenite" occurs as a trap definition (with O, Si, Ca, Ti, Al) mainly associated with sphene (titanite) rather than representing the true Fe-Ti oxide. There are single pixels of pyroxene and garnet definitions that are interpreted as grain boundary problems and not the true minerals, but they were minor.

Mineral Name	Count	Percentage
Background	165	0.0982522999970227
Quartz	59224	35.266025545598
Feldspar_Albite	61180	36.4307619019263
AlSilicate trap	22591	13.4522285408045
K-Feldspar	5818	3.4644356447435
Epidote_Fe	1159	0.69014797391848
Biotite (Fe-Mica)	3643	2.16929169023729
Limonite-clay interface	8888	5.29252389317295
Amphibole (Hornblende)	496	0.295352388475898
Muscovite	408	0.24295114181082
Ilmenite	1128	0.671688450888737
Plagioclase Feldspar	189	0.112543543632953
Sphene	890	0.529966951499092
Apatite	193	0.114925417572275
Pyroxene (En-Fs)	61	0.0363235775746569
Alm-Pyro-Gross	27	0.0160776490904219
Tourmaline	10	0.0059546848483044
Fe-Olivine	5	0.0029773424241522
Apatite in Ilmenite	1	0.00059546848483044
Zircon	1	0.00059546848483044
Zircon-rim	1	0.00059546848483044
Ti-mineral in qtz	1	0.00059546848483044
Others	2021	1.20344180784232

2.4 µm
1000.0 µm

Figure 4-32 QEMSCAN map showing mineral phases and their percentage in the first chosen area of a volcanic rock in thin section 1 shown in the petrographic images in Figure 4-15

Mineral Name	Count	Percentage
Background	398	0.237354039193235
Quartz	83291	49.6719981870445
Feldspar_Albite	48400	28.8641595400818
AlSilicate trap	19649	11.7180138595675
K-Feldspar	4209	2.51010841950836
Epidote_Fe	1305	0.778258847103446
Biotite (Fe-Mica)	2832	1.68891115325437
Limonite-clay interface	2519	1.50224830333608
Amphibole (Hornblende)	1234	0.735916794885557
Muscovite	653	0.389427607018046
Ilmenite	586	0.349471022530743
Plagioclase Feldspar	398	0.237354039193235
Sphene	376	0.224233966675016
Apatite	134	0.0799131689746067
Pyroxene (En-Fs)	110	0.0656003625910951
Talc_2	4	0.00238546773058527
Alm-Pyro-Gross	9	0.00536730239381687
Tourmaline	1	0.000596366932646319
Fe-Olivine	4	0.00238546773058527
Olivine	2	0.00119273386529264
Andalusite/Ky/Sill	1	0.000596366932646319
Rutile/Anatase-Albite interface	1	0.000596366932646319
Zircon-rim	2	0.00119273386529264
Corundum	1	0.000596366932646319
Others	1961	1.16947555491943

2.4 µm
1000.0 µm

Figure 4-33   QEMSCAN map showing mineral phases and their percentage in the second chosen area of a volcanic rock in thin section 1 shown in the petrographic images in Figure 4-15

Mineral Name		
Background	260	0.154928822123836
Quartz	70137	41.7932415280749
Feldspar_Albite	56693	33.7822296641024
AlSilicate trap	22847	13.6140723040895
K-Feldspar	4445	2.6486869782325
Epidote_Fe	1411	0.840786800064355
Biotite (Fe-Mica)	3220	1.9187338739952
Limonite-clay interface	3811	2.27089900428438
Amphibole (Hornblende)	1049	0.625078209261168
Muscovite	677	0.403410817607065
Ilmenite	551	0.328329926885514
Plagioclase Feldspar	382	0.22762619250502
Sphene	184	0.109641935656868
Apatite	124	0.0738891305513679
Pyroxene (En-Fs)	104	0.0619715288495343
Talc_2	4	0.0023835203403667
Alm-Pyro-Gross	20	0.0119176017018335
Tourmaline	18	0.0107258415316502
Fe-Olivine	4	0.0023835203403667
Staurolite	1	0.000595880085091676
Rutile/Anatase-Albite interface	1	0.000595880085091676
Zircon	2	0.00119176017018335
Low BSE edge	5	0.00297940042545838
Wollastonite	1	0.000595880085091676
Others	2128	1.26803282107509

Figure 4-34   QEMSCAN map showing mineral phases and their percentage in the third chosen area of a volcanic rock in thin section 1 shown in the petrographic images in Figure 4-15

The second aggregate that was investigated corresponds to the one shown in thin section 1 in Figure 4-7. QEMSCAN maps for two areas in this aggregate are displayed in Figures 4-35 and 4-36. As described in the petrographic thin section study, this aggregate contains mainly plagioclase feldspar and amphibole. The twinned plagioclase grains observed in polarized light have mostly Ca-rich cores with more Na-rich rims, although they do not exhibit the albite composition observed in the volcanic rock in Figures 4-32 through 4-34. Most of the black pixels labeled as "others" are Ca-Al-Si silicate that are similar to the plagioclase standard but that do not exactly match it. In a very strongly altered plagioclase grain, some of the core is Fe-rich enough to match the epidote standards. Most of the ground mass of this rock is fine-grained amphibole as identified in the petrography study, and some of the grains also show evidence of crystallinity in SEM, with cleavage and well-defined crystal shapes. In Figure 4-36, there is a very strongly altered mafic grain that is composed mainly of Fe-oxide and "Al-Silicate trap standard definitions. There are also a few relict pyroxene pixels, so this grain is interpreted as a strongly altered pyroxene grain. The hematite standard is most closely associated with this strongly altered region, and ilmenite grains mainly occur in the lower part of Figure 4-36 as discrete grains that are not associated with alteration.

Figure 4-35 QEMSCAN map showing mineral phases and their percentages in the first chosen area of the aggregate shown in the petrographic images in Figure 4-12 from thin section 1

Mineral Name		
Background	5492	1.2013273223219
Plagioclase Feldspar	200932	43.9521306498148
Amphibole (Hornblende)	137296	30.0323080927726
Limonite-clay interface	11569	2.53061831608558
Pyroxene (En-Fs)	3521	0.770188183156481
AlSilicate trap	10190	2.22897403759288
Quartz	13280	2.90488471238798
Biotite (Fe-Mica)	1822	0.398546682678531
K-Feldspar	2920	0.638724650615429
Ilmenite	5106	1.11689317330218
Hematite	1210	0.264676995631736
Muscovite	375	0.0820279945139677
Sphene	454	0.0993085586915769
Feldspar_Albite	1156	0.252864964421725
Talk_2	161	0.0352173523113301
Apatite	1355	0.296394486843803
Epidote_2	703	0.153775147048852
Epidote_Fe	1914	0.418670883999291
'Kaolinite' (clay)	1228	0.268614339368406
REE-Epidote (CeL)	638	0.139556961333097
Alm-Pyro-Gross	1658	0.362673106411089
Tourmaline	21	0.00459356769278219
Fe-Olivine	9	0.00196867186833523
Staurolite	1	0.000218741318703914
Pyroxene (Diopside)	5	0.00109370659351957
Andalusite/Ky/Sill	3	0.000656223956111742
Rutile/Anatase-silicate interface	1	0.000218741318703914
Magnesite	5	0.00109370659351957
CaSulphate-Qtz interface	4	0.000874965274815656
Apatite in Ilmenite	5	0.00109370659351957
Zircon	5	0.00109370659351957
Zircon-rim	4	0.000874965274815656
Corundum	108	0.0236240624200227
Low BSE edge	2	0.000437482637407828
Wollastonite	57880	12.6607475265825
Calcite	671	0.146775424850326
Calcite-rim	949	0.207585511450014

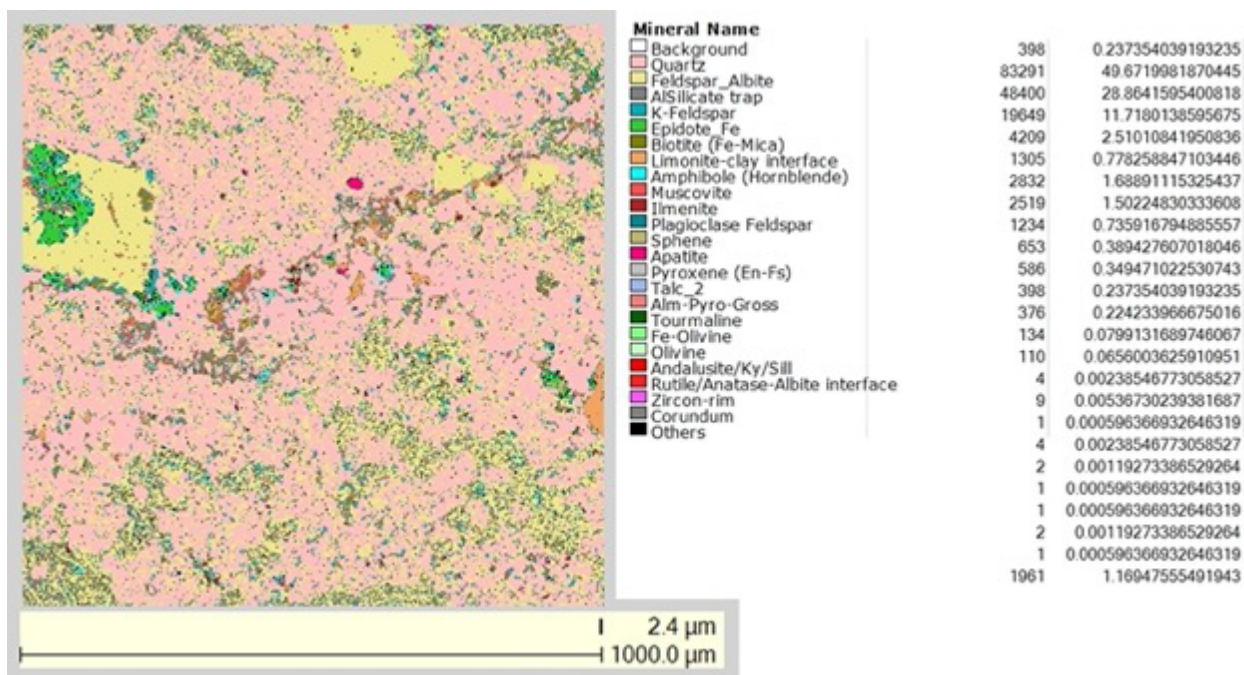**Figure 4-36 QEMSCAN map showing mineral phases and their percentages in the second chosen area of the aggregate shown in the petrographic images in Figure 4-12 from thin section 1**
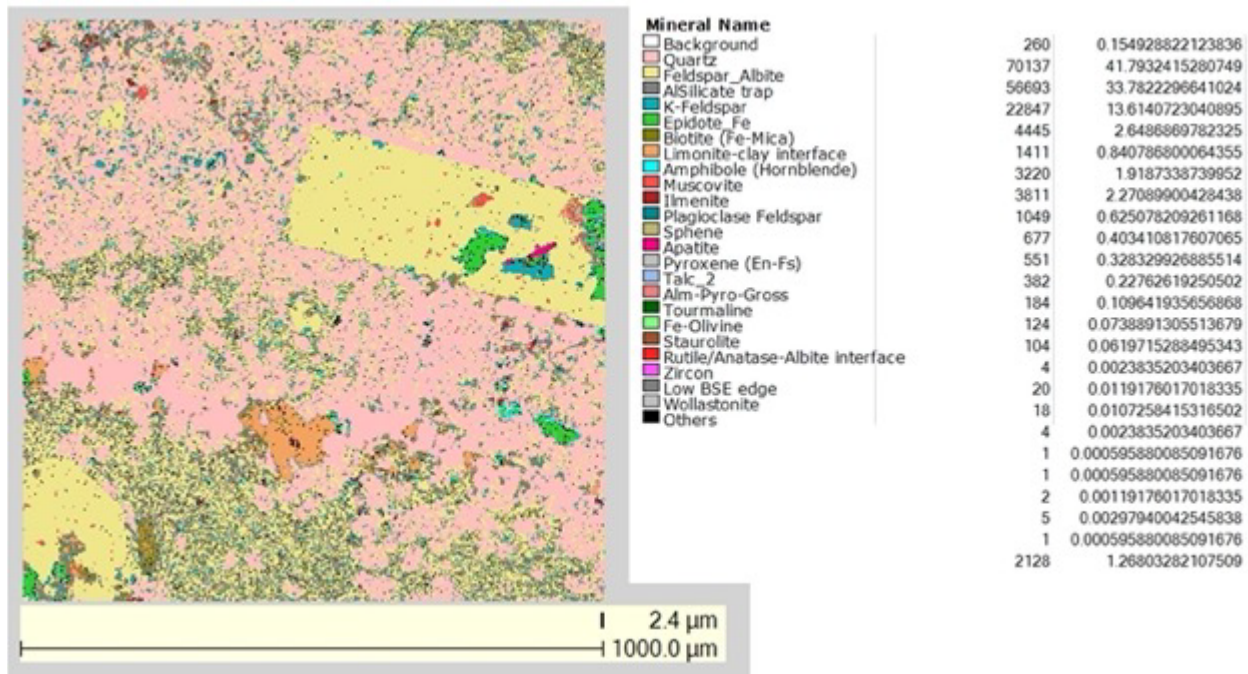
Mineral Name		
Background	3641	0.54458947884836
Plagioclase Feldspar	279395	41.7895021814989
Amphibole (Hornblende)	210974	31.5556772069634
Limonite-clay interface	35030	5.23948625214448
Pyroxene (En-Fs)	34491	5.15886726584971
AlSilicate trap	27459	4.10708115893906
Quartz	25348	3.79133592690146
Biotite (Fe-Mica)	19946	2.98335120711601
K-Feldspar	10437	1.56107673461696
Ilmenite	5908	0.883667849776466
Hematite	3182	0.475936204805131
Muscovite	2733	0.408778644793345
Sphene	2602	0.389184790981443
Feldspar_Albite	2323	0.347454369504186
Talk_2	1572	0.235126245742824
Apatite	1498	0.224057961910146
Epidote_2	1499	0.224207533313291
Epidote_Fe	1199	0.179336112370004
'Kaolinite' (clay)	1154	0.172605399228511
REE-Epidote (CeL)	983	0.147028689290837
Alm-Pyro-Gross	409	0.0611747038860146
Tourmaline	318	0.0475637061998842
Mn-silicate(Fe.Ca)	80	0.0119657122515432
Fe-Olivine	18	0.00269228525659722
Rutile/Anatase-silicate interface	1	0.00014957140314429
Apatite in Ilmenite	1	0.00014957140314429
Steel-rim	1	0.00014957140314429
Zircon	4	0.00059828561257716
Zircon-rim	5	0.00074785701572145
Albite-Chalcopyrite interface	1	0.00014957140314429
Cu trap	1	0.00014957140314429
Cr trap	4	0.00059828561257716
Wollastonite	1	0.00014957140314429

The third explored area in thin section 1 corresponds to the aggregate shown in the petrography images in Figure 4-8. QEMSCAN maps for this aggregate are displayed in Figures 4-37 and 4-38. Some of the India ink used to mark the area on the slide was captured in Figure 4-37 (upper right part of image) and shows up as white background pixels in the QEMSCAN data. This rock has a silica-rich (quartz and albite) ground mass composition similar to that observed in Figures 4-32 through 4-34, except it is texturally different. There are strongly bladed crystal shapes of quartz and albite which could correspond to devitrified glass or a rapid crystallization texture. In this region, the Al-silicate trap is composed mainly of O, Si, and Al, possibly a kaolinite group clay mineral, and some pixels containing Na, which could represent Na-smectite. As in Figures 4-32 through 4-34, the ilmenite standard is associated with sphene and occurs as a trap definition, so it does not correspond to the Fe-Ti oxide but rather to a Ca, Ti, Fe, Al silicate closely associated with sphene but more Fe- and Al-rich in composition. The limonite-clay interface definition is mostly intergrown with epidote and likely represents alteration of this Fe-rich aluminosilicate. The pixels labeled as "others" in Figure 4-37 are composed of Ca, Si, Al, and O, and they occur mainly in the cement paste. In Figure 4-38, two clusters of pixels are labeled as "others" (black) that are unusual in composition compared to all other regions. In the lower right corner of the image, one of these contains Na, Al, Si, K, Ca, and Cl. A second cluster of pixels identified as "others" in the lower left of the image contains S, K, Ca, Al, O, C, Si, and P.
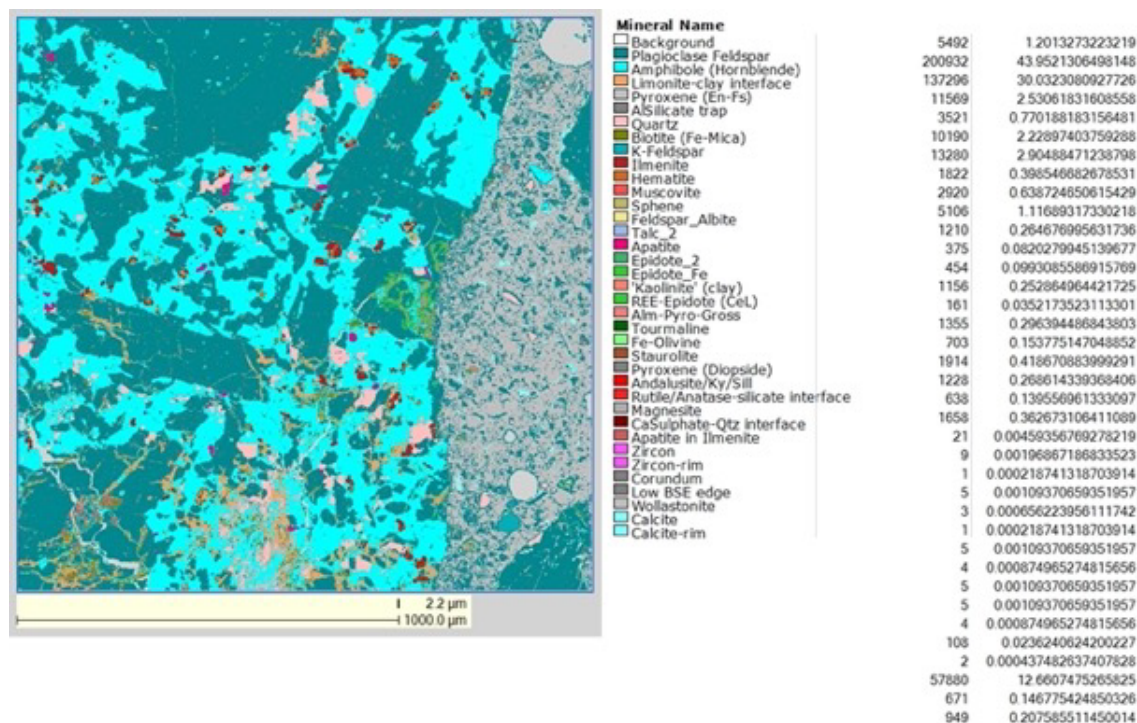

Figure 4-37   QEMSCAN map showing mineral phases and their percentages in the first chosen area of the aggregate shown in the petrographic images in Figure 4-13 from thin section 1
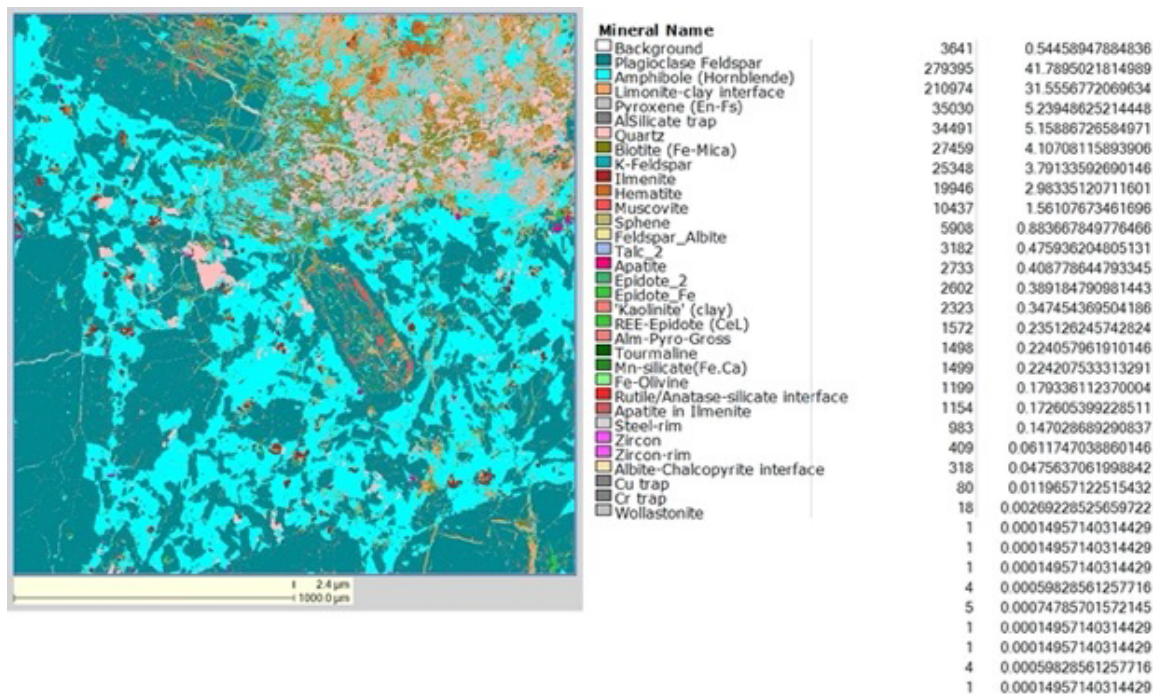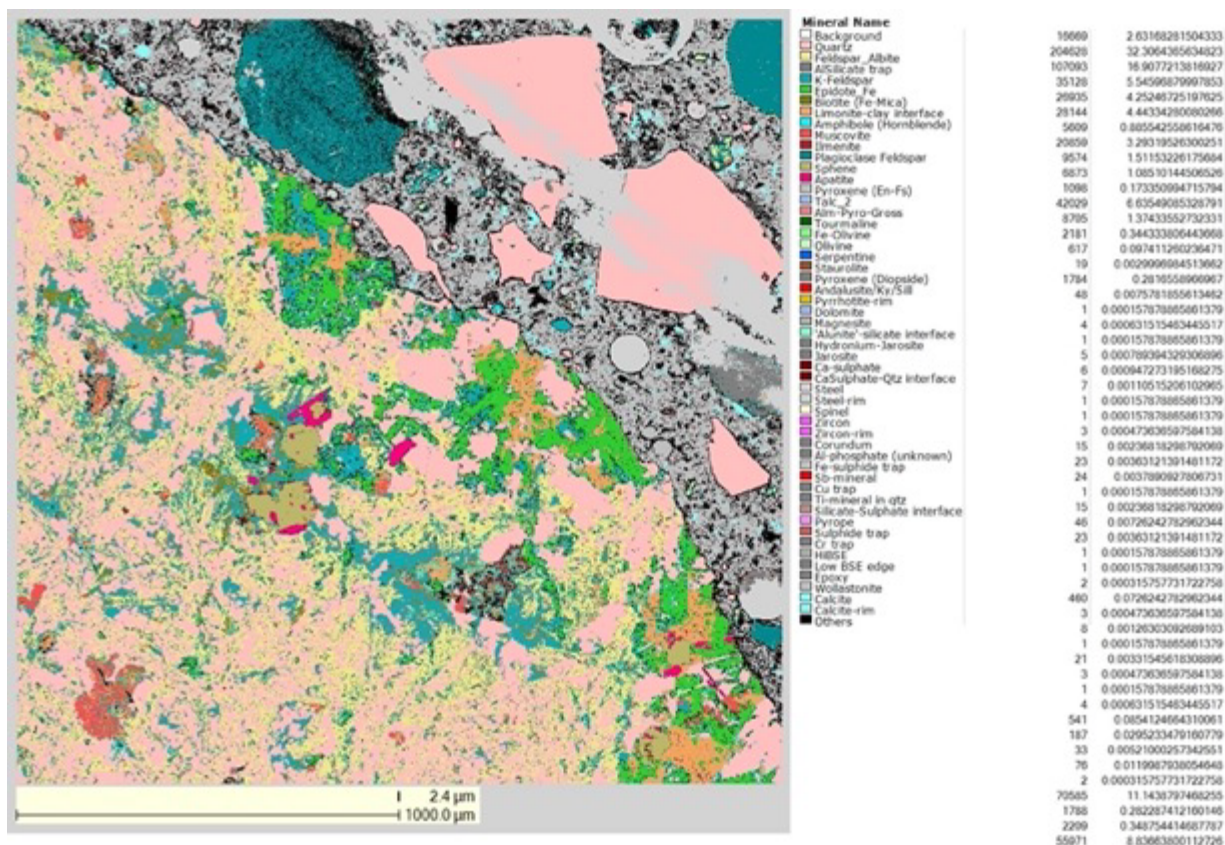
33

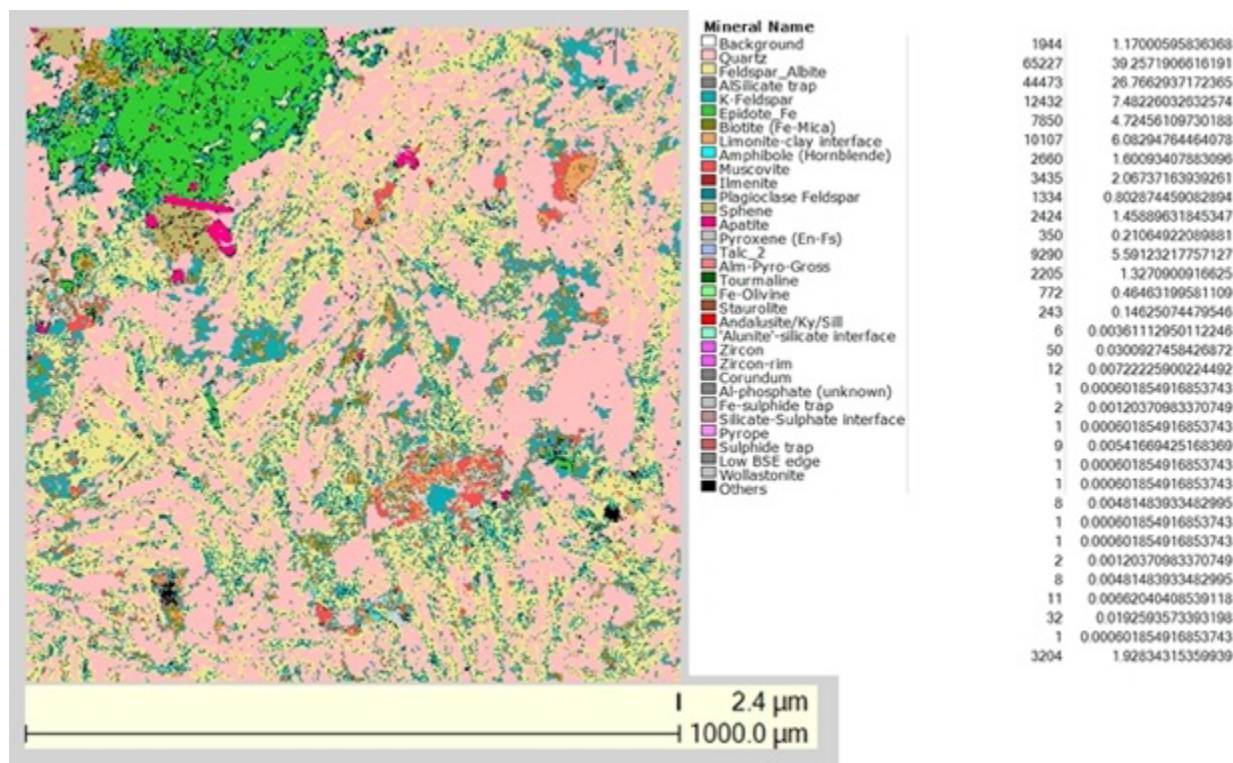| Mineral Name		
Background	1944	1.17000505836368
Quartz	65227	39.2571906616191
Feldspar_Albite	44473	26.7662937172365
AlSilicate trap	12432	7.48226032632574
K-Feldspar	7850	4.72456109730188
Epidote_Fe	10107	6.08294764464078
Biotite (Fe-Mica)	2660	1.60093407883096
Limonite-clay interface	3435	2.06737163939261
Amphibole (Hornblende)	1334	0.802874459082894
Muscovite	2424	1.45889631845347
Ilmenite	350	0.210649220898981
Plagioclase Feldspar	9290	5.59123217757127
Sphene	2205	1.3270900916625
Apatite	772	0.46463199581109
Pyroxene (En-Fs)	243	0.14625074479546
Talc_2	6	0.00361112950112246
Alm-Pyro-Gross	50	0.0300927458426872
Tourmaline	12	0.00722225000224492
Fe-Olivine	1	0.000601854916853743
Staurolite	2	0.00120370983370749
Andalusite/Ky/Sill	1	0.000601854916853743
'Alunite'-silicate interface	9	0.00541669425168369
Zircon	1	0.000601854916853743
Zircon-rim	1	0.000601854916853743
Corundum	8	0.00481483933482995
Al-phosphate (unknown)	1	0.000601854916853743
Fe-sulphide trap	1	0.000601854916853743
Silicate-Sulphate interface	2	0.00120370983370749
Pyrope	8	0.00481483933482995
Sulphide trap	11	0.00662040408539118
Low BSE edge	32	0.0192593573393198
Wollastonite	1	0.000601854916853743
Others	3204	1.92834315359939

2.4 µm

1000.0 µm

Figure 4-38 QEMSCAN map showing mineral phases and their percentages in the second chosen area of the aggregate shown in the petrographic images in Figure 4-13 from thin section 1

The last area explored in thin section 1 corresponds to the bubbles in the cement paste shown in the petrography images in Figure 4-13. The QEMSCAN map of this area is shown in Figure 4-39. The crystals in the bubbles mostly match the corundum QEMSCAN standard, and a few energy dispersive x-ray (EDX) spot analyses of these show good stoichiometry for Al_2O_3. For simplicity, the cement paste was matched with wollastonite (a calcium silicate), although it should mainly be composed of calcium silicate hydrates. There are several minerals and rock fragments of fine aggregates within the paste. Some are easy to identify, such as the perthite in the lower right (green K-feldspar background with yellow albite lamellae). The large, lowermost quartz grain has some irregular, unnatural-looking grain boundaries rimmed with a few pixel widths of a different Ca-silicate, which suggests a reaction with the paste material or an interfacial zone. Most of the Al-silicate trap phase occurs at grain boundaries between the Na and K-feldspar in the perthite and might simply be a grain boundary relict definition that belongs to one of the feldspars. The large-grain bluish-green mineral near the top of the image is variable in composition, partly matching plagioclase (Ca-Al silicate), but some Fe-rich regions match epidote standards and hornblende.
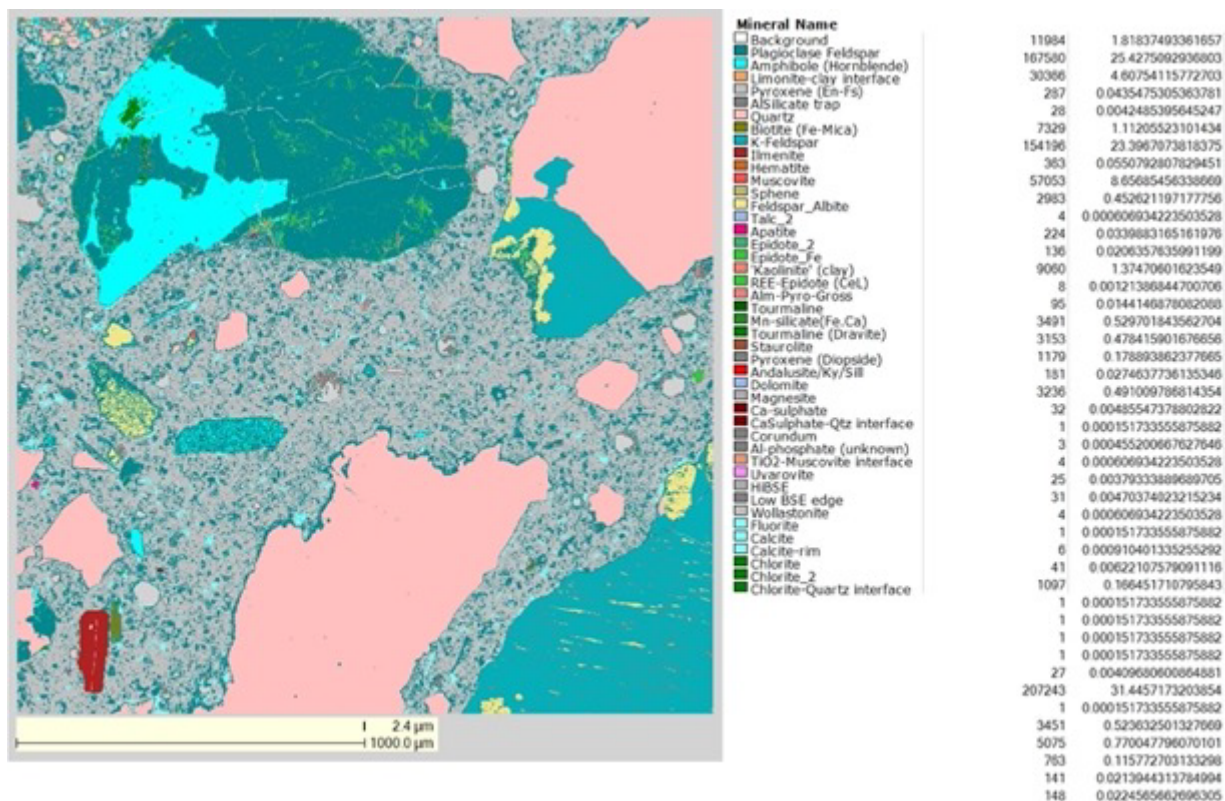
Figure 4-39   QEMSCAN map showing mineral phases and their percentages in an area of the cement paste in thin section 1 containing bubbles shown in the petrography images in Figure 4-18.

5 AGGREGATE CHARACTERIZATION

5.1 Aggregate Extraction

Along with the MXRF maps, thin section analyses, and QEMSCAN maps, the aggregates were investigated using methods such as XRD, Inductively Coupled Plasma (ICP), powder XRF, and MXRF on individual specimens. Because aggregates were required to be separated from the mortar for analysis, different methods for aggregate extraction were reviewed. These are known methods that are used in practice for recycled concrete aggregates (RCAs).

Based on a literature review [ALB16], high temperatures between 300 and 500°C do not seem to cause any negative effects on aggregates, but they do negatively affect the cement matrix. Concrete degrades after exposure to higher temperatures because its microstructure becomes rougher and the total pore volume increases, resulting in lower compressive strength. Sui and Mueller [SUI12] investigated the effect of the combination of a heat treatment and a mechanical treatment on RCA properties. The results indicate that the adhered mortar can be removed by heating to a temperature range of 250–300°C if heating is followed by strong, sufficient mechanical treatment. However, several chemical methods are implemented in practice. Ismail and Ramli [ISM13] tested the effects of various concentrations of hydrochloric acid (HCl) with different immersion times on treating the RCA to improve its performance. It was shown that there is a linear correlation between the amounts of mortar loss and the increasing concentration of acid. Accordingly, after confirming that little-to-no carbonates are present in the aggregates (from MXRF results), a heat treatment, a rough mechanical treatment, and a chemical treatment were employed.

The remaining part of core SONGS-PS-17 was cut in half and subjected to two identical heat treatment cycles. The pieces were rapidly heated to 400°C at a rate of 50°C/min, held at that temperature for four hours, and then quenched to room temperature. The pieces were then hammered to separate the aggregates from the paste as much as possible (see Figure 5-1). The remaining mortar on the coarse aggregates' surface was dissolved by immersing them in a 1 M solution of HCl at room temperature for 24 hours. In this acid solution, the cement hydration compounds were dissolved.

Figure 5-1   Resulting pieces of the core after heat and mechanical treatments

The clean coarse aggregates confirm that the core contained a very diverse group of aggregates. Visually, aggregates are of different shapes (flat vs. round) and colors. The initial sorting was performed based on the color and texture (see Figure 5-2). Five extracted aggregates were cut, embedded in epoxy, and polished. The remaining specimens were ground to fine powder for chemical and structural analyses. The mounted specimens and the ground powders are shown in Figure 5-3.

Figure 5-2   Aggregate separation for grinding and XRD analyses for mineral phase identification and quantification

Figure 5-3   Selected aggregates embedded in conductive epoxy for MXRF analyses (top) and ground for XRD, powder XRF, and ICP analyses

The polished pieces of the selected aggregates were characterized with MXRF, and the ground powder was characterized with conventional XRF, XRD and ICP to investigate their mineralogy qualitatively and quantitatively. MXRF was performed to gain insight on elemental composition, XRD for mineral phase identification and phase quantification through Rietveld refinement, and XRF and ICP for elemental and oxide content, respectively.

5.2 MXRF

MXRF maps were collected using an Atlas unit (iXRF Instruments) operated at 50 kV and 600 µA. Data acquisition was performed under vacuum with a dwell time of 300 msec, a time constant of 1, a pixel size of 15 µm, and a resolution of 400 pixels. The mapped surfaces covered areas of 6 × 6 mm.

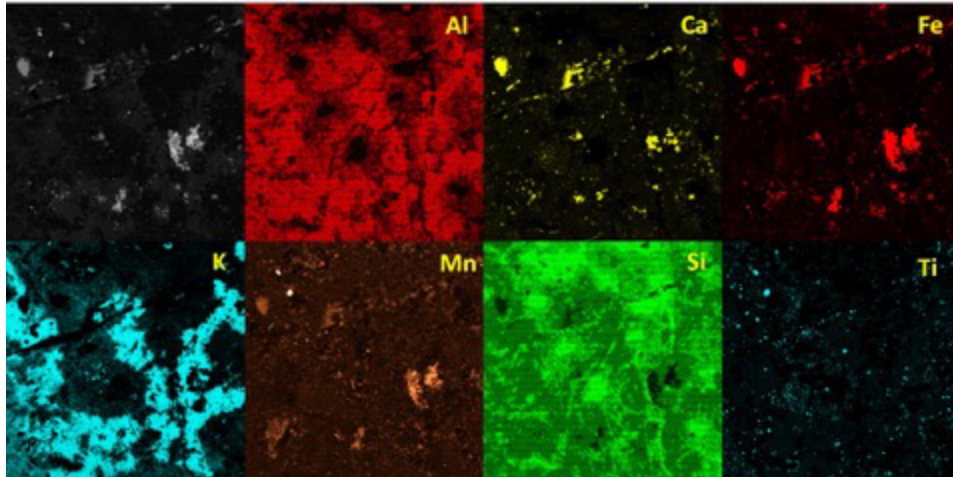The MXRF elemental maps of major elements for aggregates 1–5 are shown in Figures 5-4 through 5-8.

Figure 5-4 X-ray images and elemental maps for major elements (count intensity) for aggregate 1
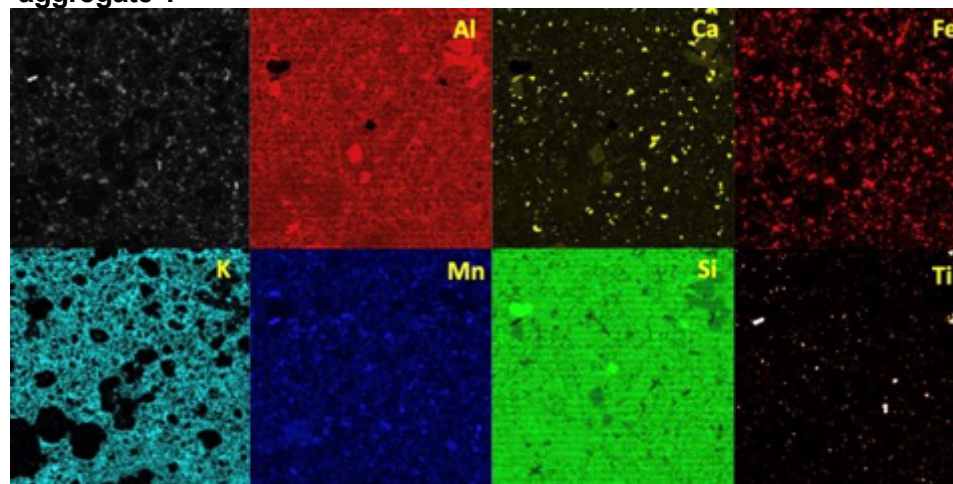

Figure 5-5 X-ray image and elemental maps for major elements (count intensity) for aggregate 2
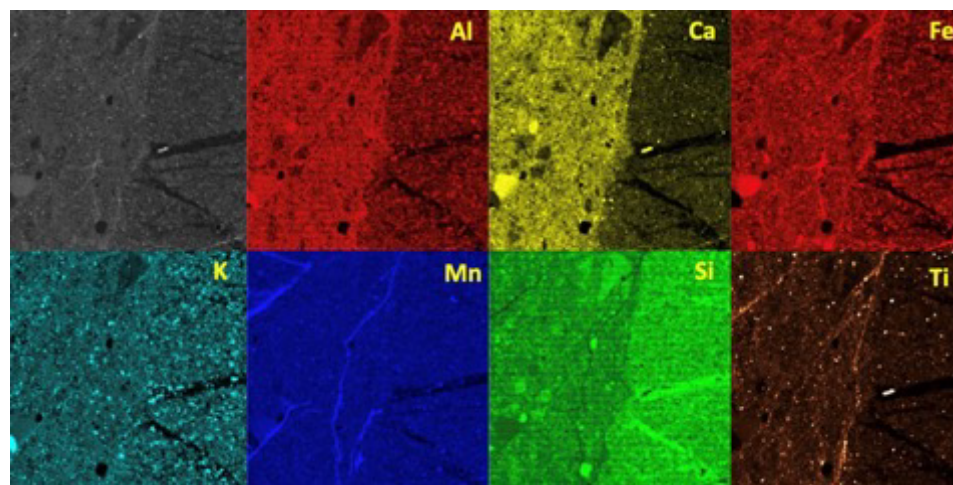

Figure 5-6 X-ray images and elemental maps for major elements (count intensity) for aggregate 3
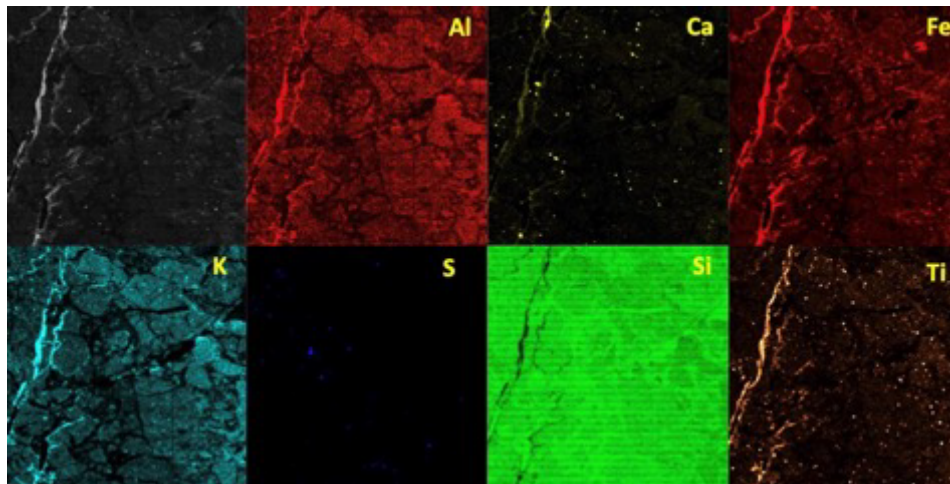
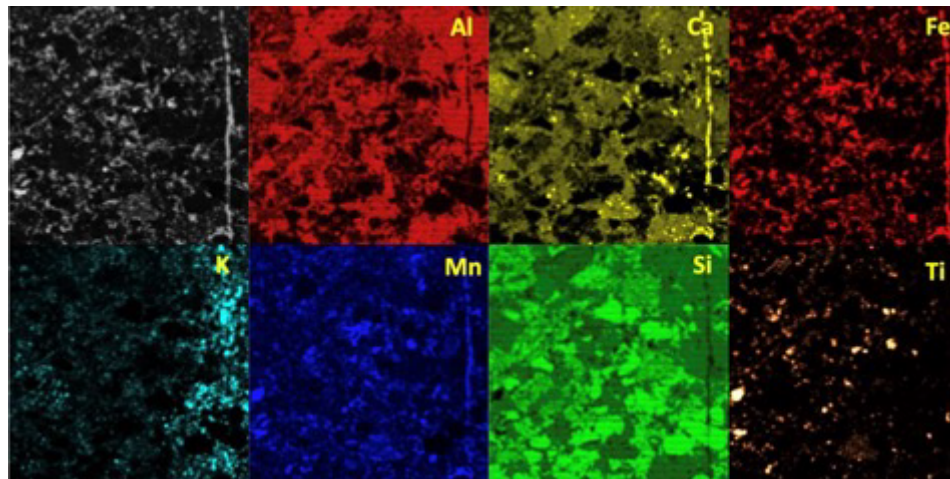**Figure 5-7   X-ray images and elemental maps for major elements (count intensity) for selected aggregate 4**

Figure 5-8   X-ray images and elemental maps for major elements (count intensity) for selected aggregate 5

5.3 Powder XRF and X-Ray Diffraction

X-ray fluorescence of the ground samples was performed on an Epsilon 1 system from Malvern Panalytical with a silver X-ray source. A small quantity of powder was placed in a sample holder that utilized a 3.6 μm Mylar film as its base. For each sample, four spectra were collected with various kV, mA, and filters to optimize detection of different types of elements (each sample had identical settings for each individual spectrum). The results were normalized to 100%.

Spectrum 1 = 50 kV, 100 μA, and Ag filter

Spectrum 2 = 50 kV, 100 μA, and Cu filter

Spectrum 3 = 12 kV, 416 μA, and Al filter

Spectrum 4 = 10 kV, 447 µA, and no filter

The elemental percentage content obtained through powder XRF are displayed in Table 5.1. The predominant element in all selected aggregates is Si, with several of them containing significant amounts of Al and K. Aggregate 5 contains a much larger amount of Fe than the other four selected aggregates. The content of Ca also varies among the specimens, with aggregate 4 containing a negligible percentage. This result is also in agreement with the XRF maps of aggregate 4 displayed in Figure 5-7, which shows Ca in very localized small areas.

Table 5-1 Elemental weight percentages present in aggregates 1-5 obtained through XRF of the powder samples

Element	Agg. 1 (%)	Agg. 2 (%)	Agg. 3 (%)	Agg. 4 (%)	Agg. 5 (%)
Al	11.832	10.705	7.736	3.398	10.581
Si	60.403	67.504	72.252	89.038	66.756
P	0.488	0.697	0.718	0.892	0.810
S	0.105	0.188	0.233	0.243	0.164
Cl	0.593	0.912	0.719	0.907	0.815
K	17.967	11.272	5.708	2.201	2.512
Ca	3.720	3.582	3.440	0.426	5.235
Ti	0.328	0.222	0.831	0.256	1.162
Mn	0.082	0.060	0.060	0.017	0.195
Fe	3.786	4.622	7.811	2.586	11.494
Ni	0.020	0.016	0.016	0.008	0.020
Cu	0.018	0.005	0.014	0.008	0.011
Zn	0.009	0.014	0.016	0.004	0.017
Rb	0.078	0.036	0.032	0.004	0.007
Sr	0.054	0.030	0.075	0.002	0.113
Y	0.020	0.010	0.008	0.002	0.008
Zr	0.109	0.044	0.088	0.005	0.057

The results for phase quantification through Rietveld refinement for aggregates 1–5 are shown in Figures 5-9 through 5-13. According to this assessment, the aggregates contain the following approximate phase percentages:

XRD patterns of the powdered samples of specimens 1, 2 and 4 were collected on a Malvern Panalytical Empyrian diffractometer using a zero-background silicon sample holder. Data were collected for diffraction angles (2θ) from 5 to 100° in Bragg-Brentano geometry. The x-ray wavelength was 0.15418 nm (Cu Ka). Typical measurement times were 30 minutes per sample. The patterns were analyzed in HighScore Plus for phase identification and quantification through Rietveld refinement.

X-ray diffraction of the powdered samples of aggregates 3 and 5 was performed on an Malvern Panalytical Empyrean diffractometer with a copper X-ray source. The incident beam optics included 0.04 radian Soller slits, a 7.0 mm automatic divergent slit, a 5 mm mask, and a 2-degree antiscatter slit. The diffracted beam optics included a 7.0 mm automatic antiscatter slit, 0.04 radian Soller slits, a nickel filter, and a PIXcel3D detector in scanning line detector (1D) mode. The automatic divergent and antiscatter slits open as the experiment progresses to maintain the programmed beam length. The relative intensity differences these automatic slits cause when compared to standard fixed slits are corrected for in HighScore Plus. The scan parameters included a 2θ range of 5-100°, 0.0263° step size, 121.89 sec/step, and a sample rotation speed of 4 sec/revolution. Results for phase quantification through Rietveld refinement for aggregates 1–5 are shown in Figures 5-9 through 5-13. According to this assessment, the aggregates contain the following approximate phase percentages:

Aggregate 1: Quartz (37%), Microcline, intermediate (36%) and Albite (27%)

Aggregate 2: Quartz (52%), Albite (34%) and Microcline, intermediate (14%)
Aggregate 3: Quartz (72%), Albite (17.5%), calcian and Biotite-1M (10.9%)
Aggregate 4: Quartz (92%), Muscovite 2M-1, sodian (4.3%) and Albite, calcian (3.3%)
Aggregate 5: Quartz (48%), Albite, calcian (47%) and Clinochlore, ferroan (4.4%)

Although the selected aggregates might not correspond to those analyzed in the petrography section and the QEMSCAN maps, the minerals identified through XRD are in accordance with most minerals observed in the optical images and the quantitative QEMSCAN maps. However, microcline was not identified explicitly in the maps. Quartz is the predominant phase present in all selected aggregates that also contain feldspars and iron oxides.
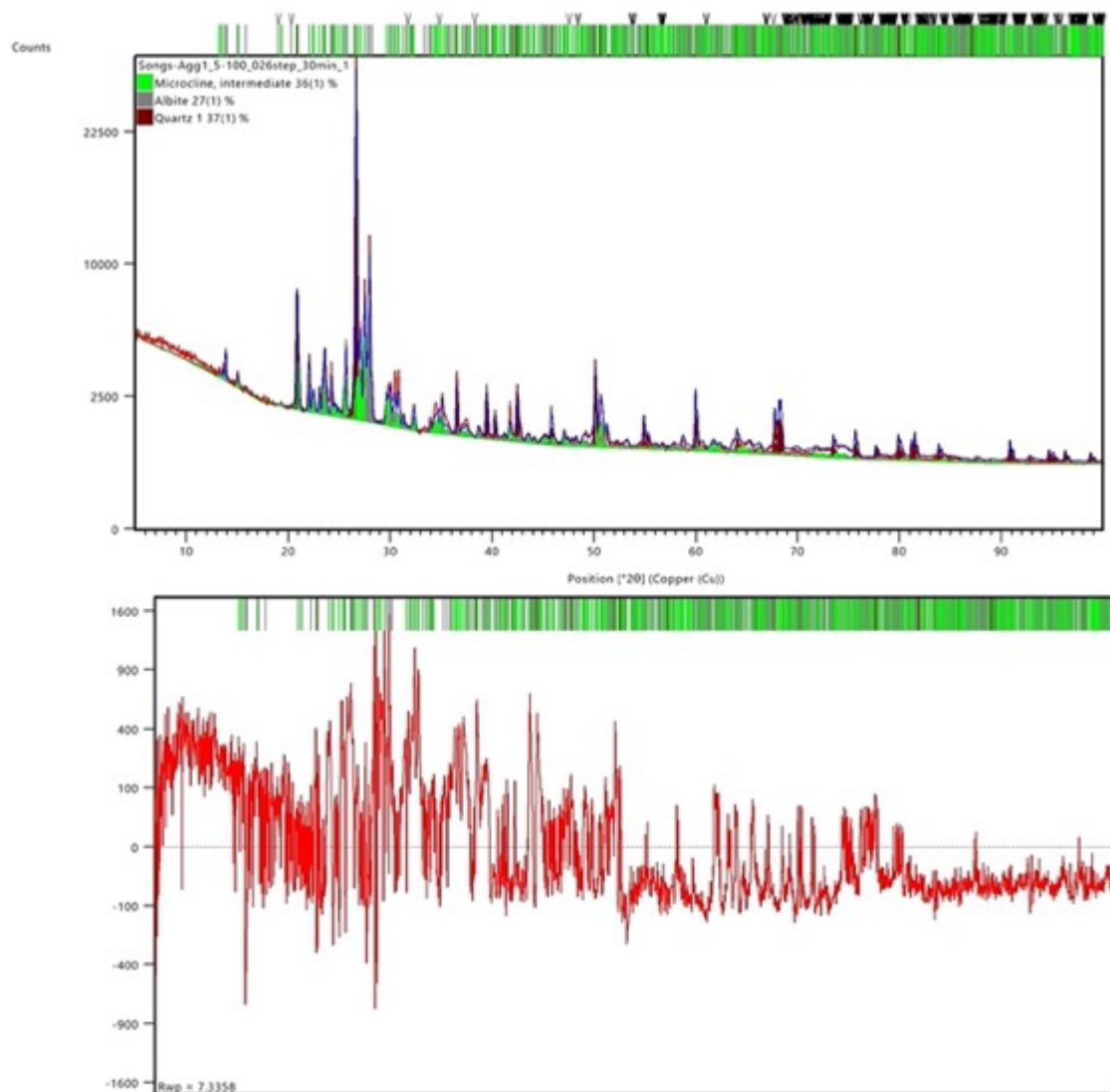

Figure 5-9   XRD pattern for aggregate 1 with Rietveld refinement for phase quantification (top), showing residuals and weighted profile R-factor (R_{wp}) (bottom)
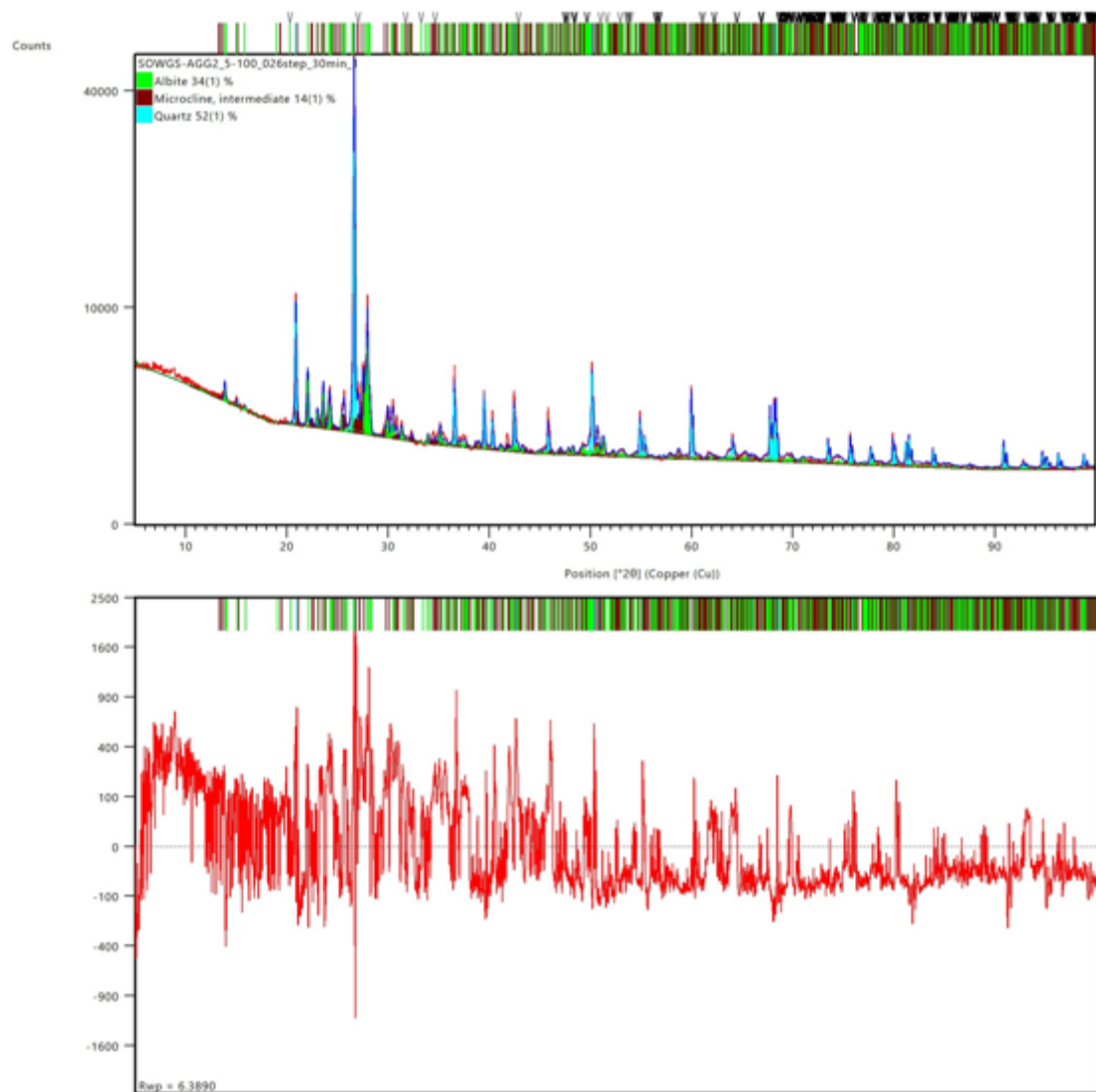
Figure 5-10   XRD pattern for aggregate 2 with Rietveld refinement for phase quantification (top), showing residuals and R$_{wp}$ (bottom)
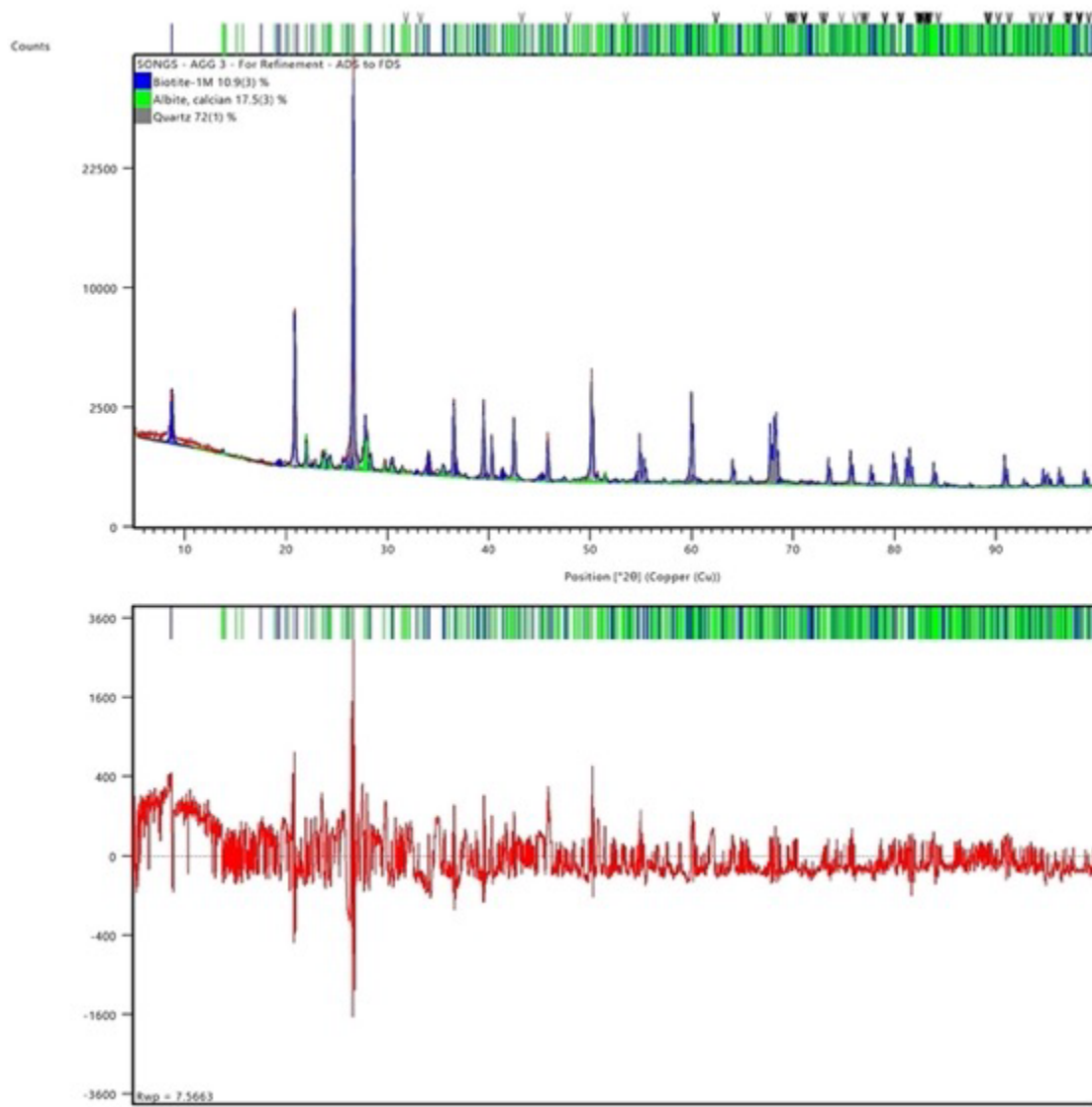
Figure 5-11   XRD pattern for aggregate 3 with Rietveld refinement for phase quantification (top), showing residuals and R$_{wp}$ (bottom)
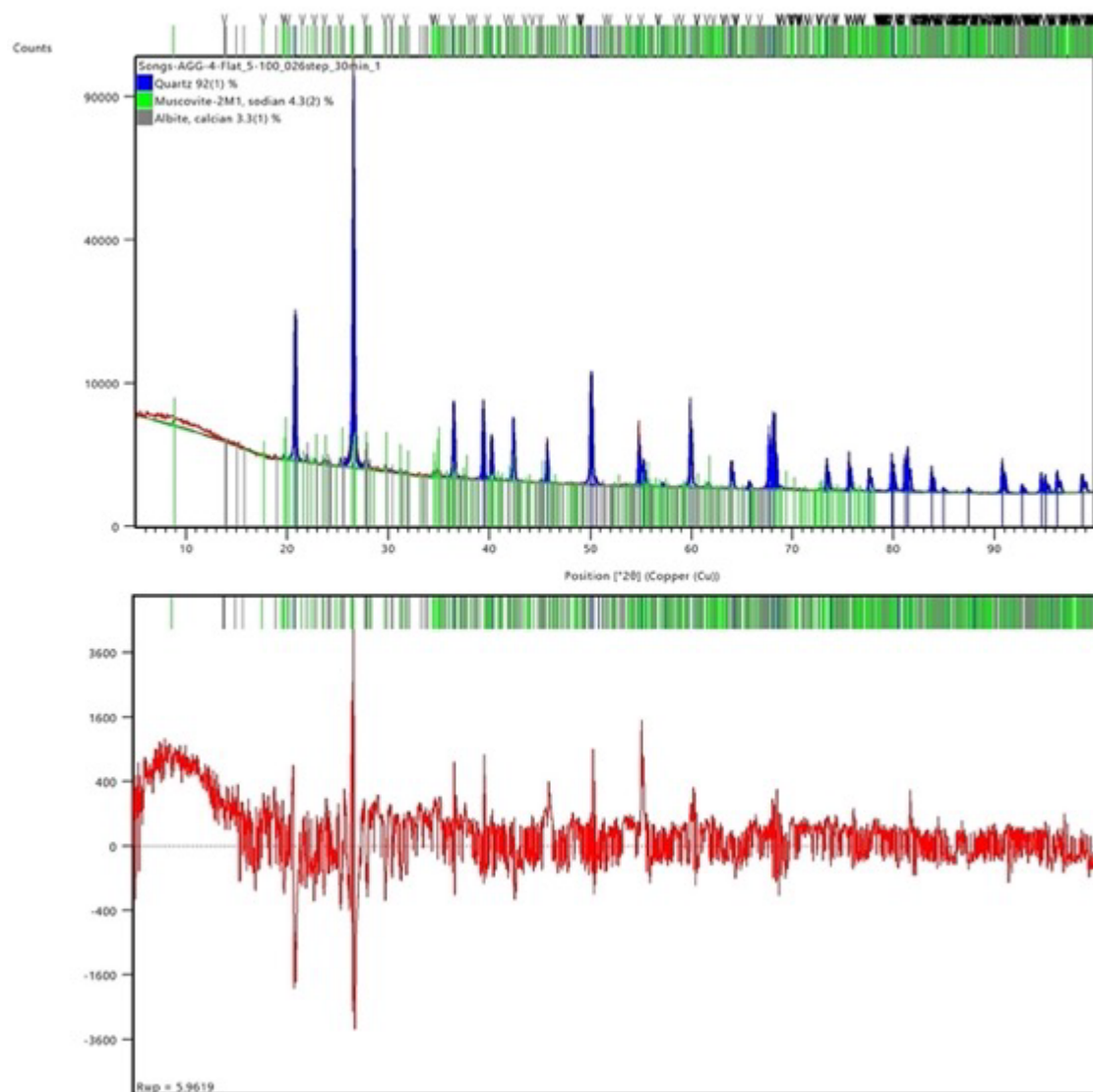
Figure 5-12   XRD pattern for aggregate 4 with Rietveld refinement for phase quantification (top), showing residuals and R$_{wp}$ (bottom)
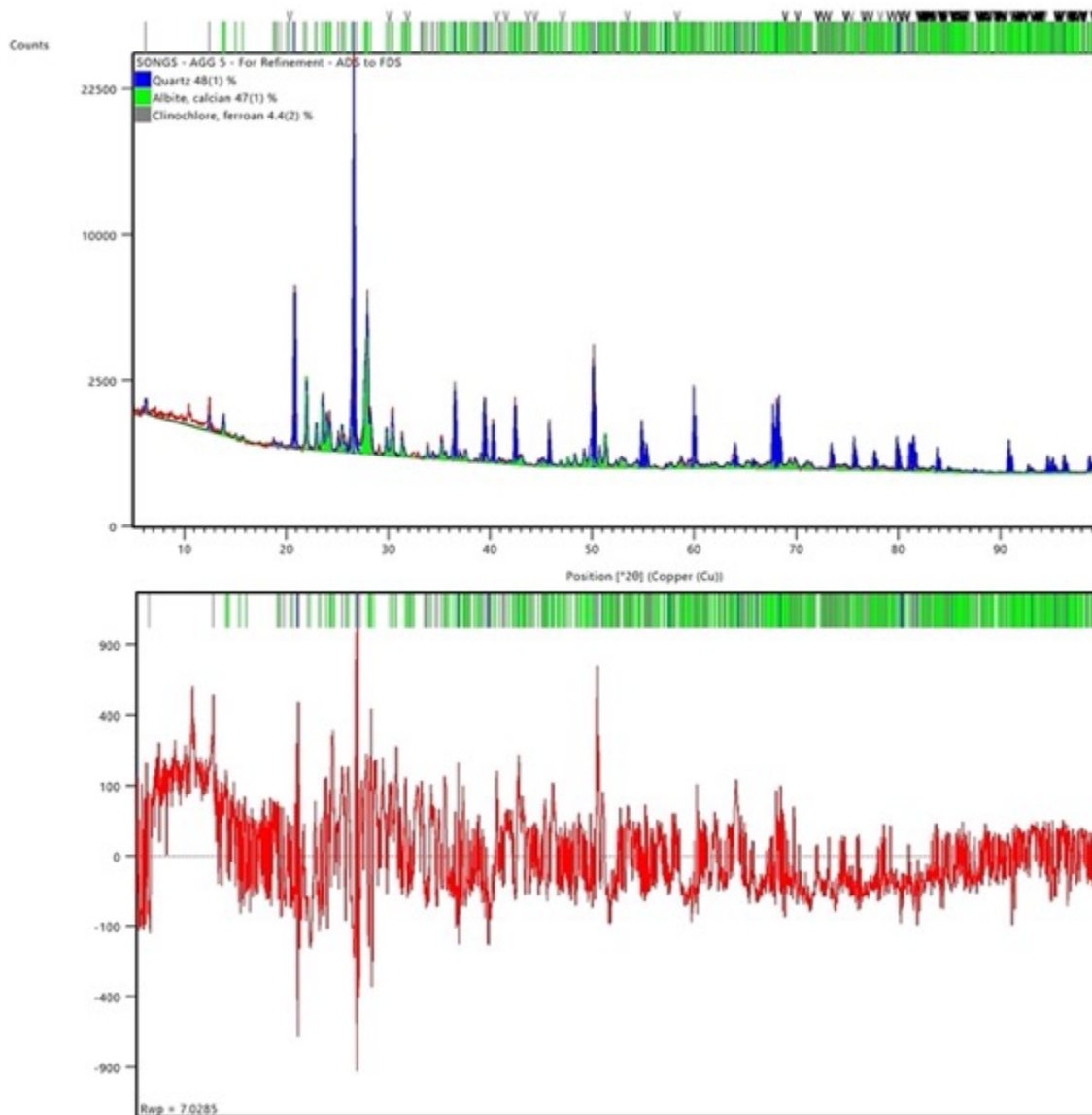
Figure 5-13   XRD pattern for aggregate 5 with Rietveld refinement for phase quantification (top), showing residuals and R_{wp} (bottom)

5.4 ICP

The oxide contents of the 5 aggregates obtained by ICP are indicated in Table 5-2. These data are complementary to those obtained through XRF (Table 4.1), because Na lies under the detection limit of XRF and can be part of many minerals present in aggregates, such as alkali feldspars. These data are in reasonable agreement with the XRF results for element content, indicating that quartz and silicates are the predominant phases for all samples. Discrepancies between results from XRF and ICP might be due to inhomogeneities of the analyzed samples. While samples for each aggregate came from a unique aggregate piece, the analyzed powders were not the same for both techniques. The amount available for XRF was very limited and might have caused uncertainty in the obtained data.

Table 5-2   Oxide contents in percent for each of the five selected aggregates

Sample	SiO$_2$ %	Al$_2$O$_3$ %	Fe$_2$O %	CaO %	MgO %	Na$_2$O %	K$_2$O %	Cr$_2$O$_3$%	TiO$_2$ %	MnO %	P$_2$O$_5$ %	SrO %	BaO %
Agg. 1	83.3	8.37	1.44	0.99	0.15	1.72	3.46	0.002	0.11	0.03	0.03	<0.01	0.11
Agg. 2	76.6	11.90	2.43	1.28	0.14	3.48	3.41	0.002	0.10	0.03	0.02	0.01	0.11
Agg. 3	82.4	7.48	3.71	1.19	1.04	1.28	2.03	0.007	0.32	0.03	0.11	0.01	0.11
Agg. 4	95.0	2.93	1.54	0.17	0.43	0.35	0.60	0.0003	0.11	0.01	0.01	<0.01	0.03
Agg. 5	75.7	11.15	4.04	2.80	1.22	3.75	0.74	0.008	0.55	0.08	0.10	0.03	0.03

The mineral compositions of each rock can be estimated using the CIPW norm "*developed in the early 1900s by Cross, Iddings, Pirsson and Washington [CIPW] [CRO02]. The CIPW normative mineralogy calculation is based on the typical minerals that may be precipitated from an anhydrous melt at low pressure, and simplifies the typical igneous geochemistry seen in nature with the following four constraints: (1) the magma crystallizes under anhydrous conditions so that no hydrous minerals (hornblende, biotite) are formed, (2) the ferro-magnesian minerals are assumed to be free of Al$_2$O$_3$, (3) the Fe/Mg ratio for all ferromagnesian minerals is assumed to be the same, and (4) several minerals are assumed to be incompatible, e.g., nepheline and/or olivine never appear with quartz. This is an artificial set of constraints, and therefore the results of the CIPW norm do not reflect the true course of igneous differentiation in nature.*"

Several CIPW calculators are available on the internet. The following calculations were conducted with *minetoshsoft online* (https://minetoshsoft.com/cipw/cipwcalc.html).

Table 5-3   CIPW estimates of the aggregates' mineral contents.

Sample	Quartz %	Plagioclase %	Orthoclase %	Corundum %	Rutile %	Hematite %	Magnetite %	Hypersthene %	Diopside %
Agg. 1	58.3	19.6	21.3	< 0.5	< 0.1	0.7			
Agg. 2	41.7	35.9	21.2			1.2	< 0.1	0.3	
Agg. 3	67.0	17.3	12.9	0.7	0.2	1.9			
Agg. 4	89.8	3.8	3.7	0.9	< 0.1	0.8		0.9	
Agg. 5	38.4	35.1	21.7	8.7	< 0.5	2.4		1.5	1.2

According to the CIPW estimates shown in Table 5.3, the volume fraction of quartz varies between ~ 40 and 90%, and the feldspars contents vary between <5 and 35%. Interestingly, these values are comparable with the compositions of the JCAMP aggregates [MAR17].

6   IRRADIATION CONDITIONS

It is estimated that SONGS Unit 2 was at ~23 effective full-power years (EFPY) at plant shutdown. Assuming (1) that the assumptions used for the RPV fast neutron fluence (E > 1.0 MeV) projections beyond end-of-cycle 10 (13.3 EFPY) from the last surveillance capsule analysis of SONGS Unit 2 remain valid [SCE01], and (2) that the methods used in Sections 3.2 and 3.3 of Lucius Pitkin, Inc. report [ESS13] are applicable, the maximum neutron fluence (E > 0.1 MeV) at the surface of the CBS at ~23 EFPY is estimated to be ~1.8 × 10^{19} n.cm^{-2}. The estimated neutron fluence (E > 10 keV) of the SONGS Unit 2 CBS inner surface at shutdown is 2.7 × 10^{19} n.cm^{-2}. This value is estimated using a three-loop Pressurized Water Reactor model with the RPV thickness of SONGS Unit 2 and an air gap (including thermal insulation) of 18.8 cm between the RPV outer radius and the CBS inner radius.

7 POTENTIAL FOR IRRADIATION-INDUCED DAMAGE

In-service irradiation temperature of the SONGS CBS is not well determined at this point. American Concrete Institute design codes limit the temperature to 65°C (Local spikes up to 93°C are permitted around the RPV nozzles, for example). The temperature at the back of the CBS is generally assumed to be around ~40°C. Without irradiation-induced heating (energy deposition), the steady-state temperature profile would be linear, varying from < 65°C at the concrete surface facing the reactor's cavity to ~40°C at the back of the CBS wall. The irradiation-induced heating modifies the otherwise linear temperature profile in steady condtions to form a "hump" profile whose peak is located at about 30 cm depth in the CBS from the cavity. The local temperature increase is estimated to be around +10°C [REM13]. As a preliminary assessment, the range of the irradiation temperature in the most exposed region (i.e., facing the RPV beltline and to ½ m deep in the biological shield) is estimated to be between 40 and 65°C. The fluence at the inner surface of the CBS is estimated at 2.7×10^{19} n.cm^{-2} 30% at E > 10 keV, or 1.9–3.5×10^{19} n.cm^{-2}.

Concrete and concrete constituents irradiated in test reactors exhibit physical and mechanical changes when exposed to fast-neutron fluence levels above 10^{19} n.cm^{-2} (E > 0.1 MeV) [FIE15]. Changes in the elastic modulus and tensile strength are more prominent than changes in the compressive strength. The losses of mechanical properties (compression strength, tensile strength, and Young's modulus) are directly associated with the RIVE of the concrete's aggregates, which depends on the mineralogy of the rock-forming aggregates. The RIVE of the silicate minerals depends on their chemical structures as associated with the nature of the bonds of the Si^{4+} tetrahedrons. Covalent bonds experience more irradiation-induced damage because they tend to be more rigid, more directional, and stronger than ionic bonds. Therefore, the irradiation-induced displacement of atoms tends to affect the surrounding atoms ("truss-like effect") and broken covalent bonds do not easily reform. The ionic bonds exhibit the opposite tendency. Silicate structures are classified in groups corresponding to their Si^{4+} coordination, which accounts for the approximate number of covalent bonds per Si atom. Consequently, silicates RIVE at full amorphization ranks as follows from the highest to the lowest – See summary in [LEP18]:

- quartz (~18%)

- other frameworks silicates (tectosilicates) including feldspars (7–8%)

- sheet silicates (phyllosilicates), including micas and clays (< 3% – Excluding data from [CRA58])

- single and double chains silicates (inosilicates), including pyroxenes and nesosilicates (island), including olivine and garnet (< 3%)

- island silicates (orthosilicates) such as Mg-olivine (< 1%).

Thus, aggregate RIVEs depend mainly on the quartz and feldspar contents [MAR17].

The expansion of quartz under neutron irradiation in test reactors is well documented in the scientific literature [BYK81]. At $\sim2.5 \times 10^{19}$ n.cm^{-2} (E > 10 keV), quartz expansion varies between < 0.5% at 80–100°C to ~2% at 25–30°C [BYK81].

RIVE data in this range of irradiation conditions are scarce, even for quartz. In the following table, data collected from the Irradiated Minerals, Aggregates and Concrete (IMAC) database that are relevant for SONGS irradiation conditions are presented. Because of annealing effects, RIVEs at lower temperatures provide upper bound values, whereas RIVEs at higher temperatures should be considered as lower bound values.

Table 7-1 Quartz expansion at irradiation conditions comparable to SONGS at end of operation (Data extracted from the IMAC database)

RIVE (%)	Fluence (× 10^{20} n.cm^{-2} at E > 0.1 MeV)	Temperature (°C)	Reactor / Reference
1.18	0.19	25–30	channel 07-06 of AM reactor
1.62	0.26	ibid	
2.98	0.28		
7.93	0.38		
0.76	0.40	60–80	OK-70 channel of BR-10 reactor
3.10	0.55	50–100	[KRI98]
3.77	0.56	ibid	
4.10	0.51	50–100	[PRI58]
4.51	0.51	ibid	
2.12	0.50	50–100	[WIT54]

At 1.9×10^{19} n.cm^{-2} (E >10 keV), the lower fluence estimate, the RIVE of quartz is expected to be lower than 1.2%. At $1.9–3.6 \times 10^{19}$ n.cm^{-2} (E >10 keV) the higher fluence estimate, the RIVE of quartz is expected to be bounded between 0.8% and 7.9% (Table 7-1). The expected RIVE of feldspars in the fluence range of $1.9–3.57 \times 10^{19}$ n.cm^{-2} at T ~50–65°C is <0.13% (Table 7-2).

Table 7-2 Feldspar expansion at irradiation conditions comparable to SONGS at end of operation (Data extracted from the IMAC database)

RIVE (%)	Fluence ×10^{20} n.cm^{-2} at E > 0.1 MeV	Temperature (°C)	Reactor / Reference
0.13	0.39	60–65	channel 02-13 of AM reactor, albite
0.63	0.17	30–45	channel 02-13 of AM reactor, microcline
0.43	0.37	ibid	

Best estimate expansions can also be calculated using the RIVE models derived from the extensive dataset gathered in the IMAC database [LEP18] (See Table 7-3).

Table 7-3 Estimated RIVE values of minerals at irradiation conditions comparable to SONGS at end of operation. (Values calculated using the models derived from the IMAC database [LEP18])

	Fluence × 10^{19} n.cm^{-2} (E >10 keV)	1.9		3.57	
	Temperature (°C)	40	65	40	65
RIVE (%)	Quartz	1.8	0.7	4.2	1.7
	Feldspar	< 0.01	< 0.01	< 0.01	< 0.01
	Mica	0.4	0.4	0.7	0.7

Using the data from Table 7-3 and the mineral composition derived from the Rietveld analysis, the best estimates for the aggregate expansions without cracking are provided in Table 7-4.

53

These expansions correspond to the expected values if the aggregates were irradiated in test reactor conditions. The expansions vary between 0.27 and 3.98%, depending on the aggregates and the irradiation conditions. The average expansions considering each aggregate separately range between 0.78 and 1.95%. For the sake of comparison, the post-irradiation RIVEs measured on the JCAMP aggregates irradiated at 2.0×10^{19} $n.cm^{-2}$ (E >10 keV) and 53.3°C vary between ~0.4 and ~0.9%. It can be inferred that the expansion of the SONGS aggregates is likely to be on the order of 1% if irradiated in test reactors at 2.7×10^{19} $n.cm^{-2}$ 30% at E > 10 keV and ~55°C. At 1% RIVE, the loss of Young's modulus can be as low as 10% or as high as 60%, depending on the aggregate's assemblage mineralogy [DEN12].

Table 7-4 Estimated RIVE values of aggregates at irradiation conditions comparable to SONGS at end of operation

	Fluence × 10^{19} n.cm^{-2} (E >10 keV)	1.9		3.57	
RIVE (%)	**Agg. 1:** Quartz (37%), Microcline, intermediate (36%) and Albite (27%)	0.67	0.27	1.56	0.64
	Agg. 2: Quartz (52%), Albite (34%) and Microcline, intermediate (14%)	0.94	0.37	2.19	0.89
	Agg. 3: Quartz (72%), Albite (17.5%), calcian and Biotite-1M (10.9%)	1.35	0.56	3.12	1.32
	Agg. 4: Quartz (92%), Muscovite 2M-1, sodian (4.3%) and Albite, calcian (3.3%)	1.67	0.66	3.89	1.59
	Agg. 5: Quartz (48%), Albite, calcian (47%) and Clinochlore, ferroan (4.4%)	0.89	0.36	2.05	0.85

8   CONCLUSIONS

The range of irradiation temperature in the most exposed region (i.e., facing the RPV beltline and up to ½ m deep in the biological shield) is estimated between 40 and 65°C. The maximum neutron fluence at the surface of the CBS at ~23 EFPYs is estimated to be ~1.8 × 10^{19} n.cm^{-2} (E > 0.1 MeV) or 2.7 × 10^{19} n.cm^{-2} at E > 10 keV, with an uncertainty of $\pm$30%: 1.9–3.5 × 10^{19} n.cm^{-2}. Hence, the fast neutron exposure exceeds the admitted threshold for irradiation damage of concrete.

Three unirradiated concrete specimens were cored from three elevations of thr outside of Steam Generator Room 2 (106) on the north wall of the primary shield at elevations of 45, 30 and 17 feet in Unit 2. The specimens were prepared and characterized using thin-section petrography, micro x-ray fluorescence, scanning electron microscopy, energy dispersive x-ray spectroscopy (QEMSCAN analysis), inductively coupled plasma spectroscopy, and x-ray diffraction to determine the chemical compositions and mineralogies of the concrete-forming aggregates.

The aggregates extracted from the concrete specimens cored from SONGS Unit 2 exhibit a complex assemblage of shale (mudstone), San Onofre breccia, and sandstone, rich in varied types of clastic and aphanitic silicates. The silicates present in the aggregates have very different crystalline structures and grain sizes. The silicates belong to varied groups, including tecto-, phyllo-, ino- and nesosilicates, from higher to lower coordination of SiO_2.

This heterogenous configuration favors the formation of irradiation-induced cracking in the vicinity of quartz grains and a higher loss of the aggregates' elastic modulus at any given radiation-induced expansion when compared to aggregates of more uniform chemical compositions. The quartz content is a good indicator of the potential for radiation-induced expansion, and it varies between ~35 and ~90% in the tested aggregates. At the fast-neutron irradiation fluence and temperature at the end of operation, the radiation-induced expansion of the SONGS aggregates is estimated to be approximately ~1% (without accounting for possible expansion-induced cracking). At that level of expansion, the mechanical properties of irradiated aggregates in test reactors are substantially affected. For example, Young's modulus can decrease from -10 to -60%, depending on the mineralogy of the aggregates.

In conclusion, the susceptibility of irradiation-induced damage in concrete is governed by the exposure level (fast neutron fluence > 10^{19} n.cm^{-2} at E > 0.1 MeV) and the mineralogy of the aggregate (high quartz content and chemical heterogeneity of the assemblage). Both conditions are met for the SONGS CBS. The fast-neutron flux in test reactors is about 30 to 180 higher than in light-water reactors. The effects of flux reduction on the development of the irradiation-induced damage rate are unknown. For these reasons, harvesting in-service irradiated concrete from the SONGS (unit 2 or 3) biological shield is an unparalleled opportunity to study the flux effects of neutron irradiation. Oak Ridge National Laboratory is developing a research plan for the harvesting, characterization, and companion modeling for SONGS concrete. This plan will be transmitted to the NRC in a separate document.

9 REFERENCES

[ALT97] Altheim, B. (1997). Low-Grade Metamorphism in the Catalina Schist: Kinetic and Tectonic Implications, *M.Sc. Dissertation*, Lehigh University.

[ALB16] Hanaa Khaleel Alwan Al-Bayati, Prabir Kumar Das, Susan L. Tighe, Hassan Baaj, Evaluation of Various Treatment Methods for Enhancing the Physical and Morphological Properties of Coarse Recycled Concrete Aggregate, *Construction and Building Materials*, Volume 112, 2016, 284–298, https://doi.org/10.1016/j.conbuildmat.2016.02.176.

[BLO58] Blosser, T.V., Reid, R.C., Bond, G.W., Reynolds, A.B., Lee, L.A., Speidel, T.O., Morgan, D.T., Vroom, D.W., Nichols, J.F. and Welt, M.A. (1958). *A Study of the Nuclear and Physical Properties of the ORNL Graphite Reactor Shield*, Tech. Report, Oak Ridge National Laboratory, ORNL-2195.

[BYK81] Bykov, V.N., Denisov, A.V., Dubrovskii, V.B., Korenevskii, V.V., Krivokoneva, G.K. and Muzalevskii, L.P. (1981). "Effect of Irradiation Temperature on the Radiation Expansion of Quartz," *Atomnaya Energiya*, 51(3):593–595.

[CRAW58] Crawford, H.H. Jr. and Wittels, M.C. (1958). Radiation stability of nonmetals and ceramics, in *Proceedings of the Second U.N. International Conference on the Peaceful Uses of Atomic Energy*, 5(P/679):300-310.

[CRO02] Cross, W., Iddings, J.P., Pirsson, L.V. and Washington, H.S. (1902). "A Quantitative Chemico-Mineralogical Classification and Nomenclature of Igneous Rocks." *The Journal of Geology*, 10:555–690.

[DEN12] Denisov, A.V. and Dubrovskii, V.B. and Solovyov, V.N. (2012). *Radiation Resistance of Mineral and Polymer Construction Materials*, ZAO MEI Publishing House.

[ESS13] Esselman, T. and Bruck (2013). Expected Condition of Concrete Exposed to Radiation at Age 80 Years of Reactor Operation, Lucius Pitkin, Inc. Report No. A13276-R-001, Rev. 0, December 2013, ORNL/TM-2018/768, Rev. 0, January 2018.

[FIE15] Field, K., Remec, I. and Le Pape, Y. (2015). "Radiation Effects on Concrete for Nuclear Power Plants – Part I: Quantification of Radiation Exposure and Radiation Effects," *Nuclear Engineering and Design*, 282:126–143.

[GIO17] Giorla, A. and Le Pape, Y. and Dunant, C. (2017). Computing creep-damage interactions in irradiated concrete, *Journal of Nanomechanics and Micromechanics*, 7(2): 04017001-1-13

[GRA71] Gray, B.S. (1971). The effects of reactor radiation on cement and concrete, Proceedings of an Information *Exchange Meeting on 'Results of Concrete Irradiation Programmes'*, EUR 4751 f-e, Brussels, Belgium, April 19, Commission des Communautés Européennes.

[HIE78] Hilsdorf, H.K., Kropp, J. and Koch, H.J. (1978). The Effects of Nuclear Radiation on the Mechanical Properties of Concrete, *Special Publication of The American Concrete Institute*, 55:223-254.

[ISM13] Ismail, S. and Ramli, M. (2013). Engineering Properties of Treated Recycled Concrete Aggregate (RCA) for Structural Applications, *Construction and Building Materials*, 44, 464–476.

[KAM20] Kambayashi, D., Sasano, H., Sawada, S., Suzuki, K. and Maruyama, I. (2020). Numerical Analysis of a Concrete Biological Shielding Wall under Neutron Irradiation by 3D RBSM, *Journal of Advanced Concrete Technology*, 18:617-632.

[KRI98] Krivokoneva, G.K, Solntseva, L.S., Pergamenshchik, B.K. and Korenevskii, V.V. (1998) Changes in Quartz upon Neutron Irradiation, *Inorganic Materials*, 10(11):1074.

[LEP18] Le Pape, Y., Alsaid, M.H.F. and Giorla, A.B. (2018). Rock-Forming Minerals Radiation-Induced Expansion – Revisiting Literature Data, *Journal of Advanced Concrete Technology,* 16(5):191–209.

[LEP20] Le Pape, Y., Sanahuja, J. and Alsaid, M.H.F. (2021). Irradiation-Induced Damage in Concrete-Forming Aggregates: Revisiting Literature Data through Micromechanics, *Materials and Structures,* 54(75).

[MAR17] Maruyama, I., Kontani, O., Takizawa, M., Sawada, S., Ishikawa, S., Yasukouchi, J., Sato, O., Etoh, J. and Igari, T. (2017). "Development of the Soundness Assessment Procedure for Concrete Members Affected by Neutron and Gamma-Irradiation," *Journal of Advanced Concrete Technology*, 15:440–523.

[PRI58] Primak, W. (1958). Fast-Neutron-Induced Changes in Quartz and Vitreous Silica, *Physical Review*, 110(6):1240–54.

[ROW94] Rowland, S.M. (1984). Geology of Santa Catalina Island, *California Geology*, November, 239–251.

[SCE01] Southern California Edison, "Surveillance Capsule Test Report San Onofre Nuclear Generating Station, Unit 2," Docket Nos. 50-361, October 19, 2001.

[STU79] Stuart, C.J. (1979). Lithofacies and Origin of the San Onofre Breccia, Coastal Southern California, in *A Guidebook to Miocene Lithofacies and Depositional Environments, Coastal Southern California and Northwestern Baja California,* Geological Society of America, (Copyright © 2012 Pacific Section, SEPM, Society for Sedimentary Geology, 25–42.

[SUI12] Y. Sui, A. Mueller, Development of Thermo-Mechanical Treatment for Recycling of Used Concrete, *Mater. Struct.*, 45 (10) (2012), 1487–1495.

[VED79] Vedder, J.G, Howell, D.G. and Farman, J.A. (1979). Miocene Strata and Their Relation to Other Rocks, Santa Catalina Island, California, *Cenozoic Paleogeography of the Western United States: Pacific Section Coast Paleogeography Symposium*, 3:239–257.

[WIT54] Wittels, M. and Sherrill, F.A. (1954). Radiation Damage in SiO_2 Structures, *Physical Review*, 93:1117–1118.

APPENDIX A CORING LOCATIONS
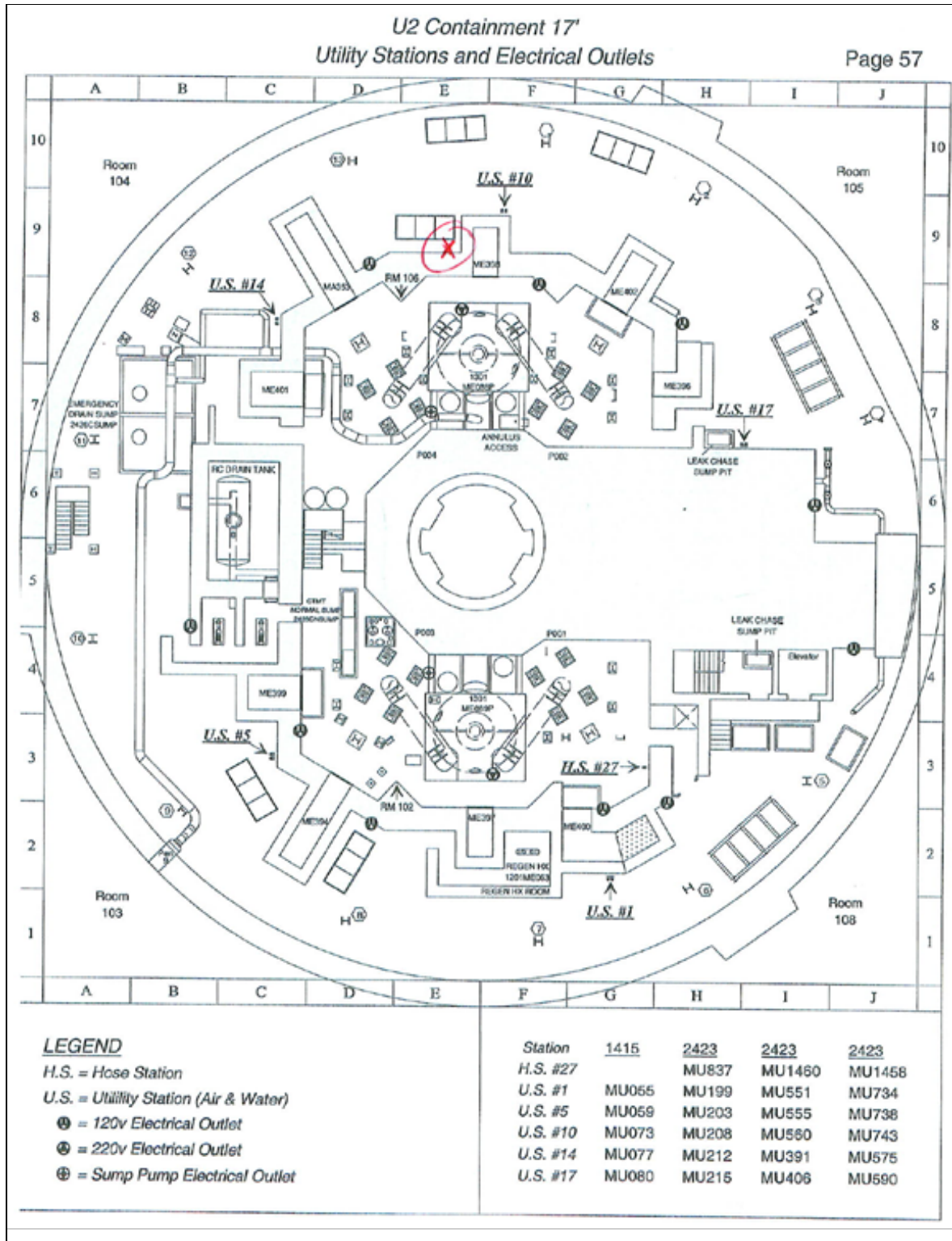
Figure A-1   Coring location at 17 ft elevation
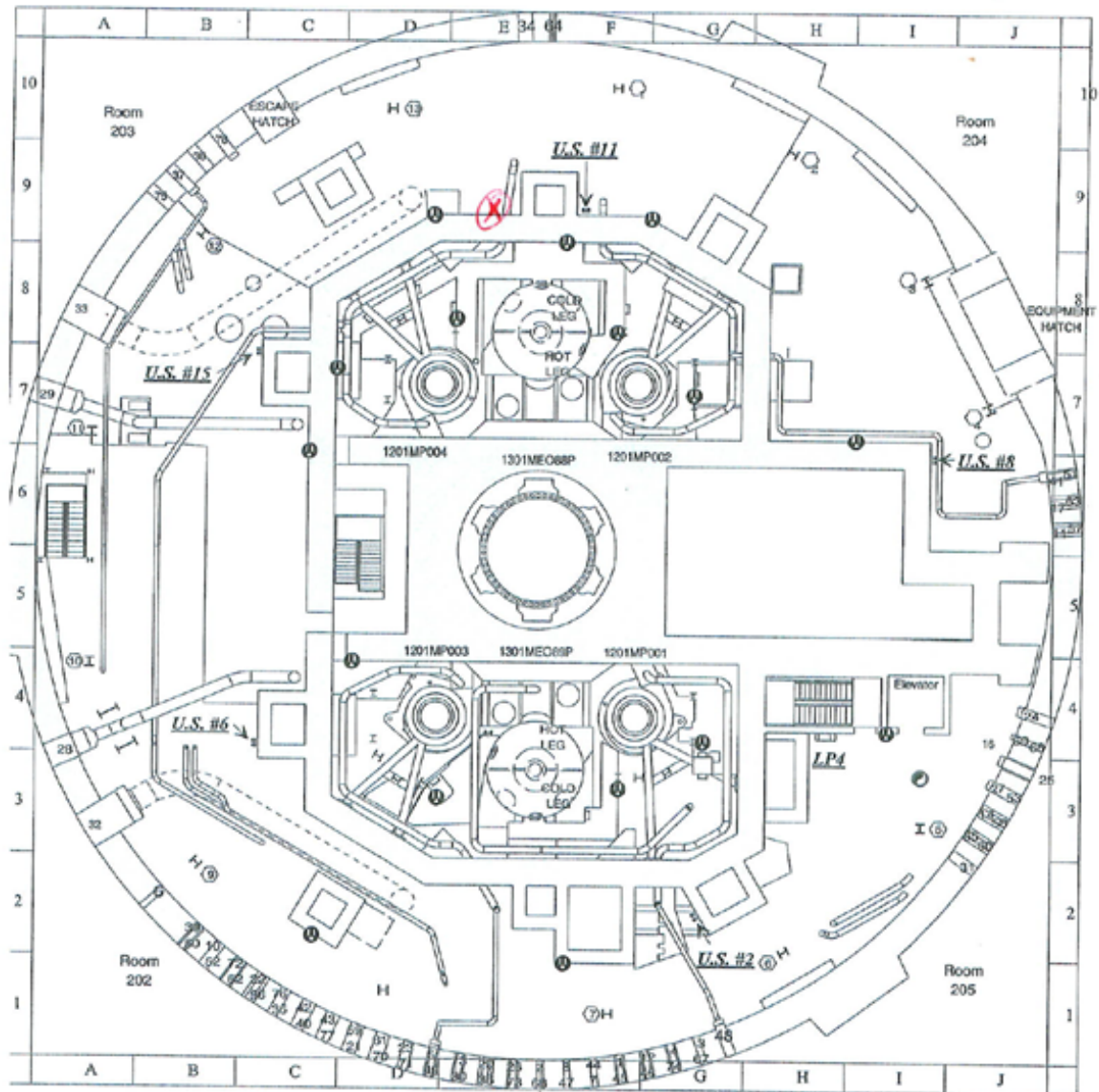
Figure A-2   Coring location at 30 ft elevation
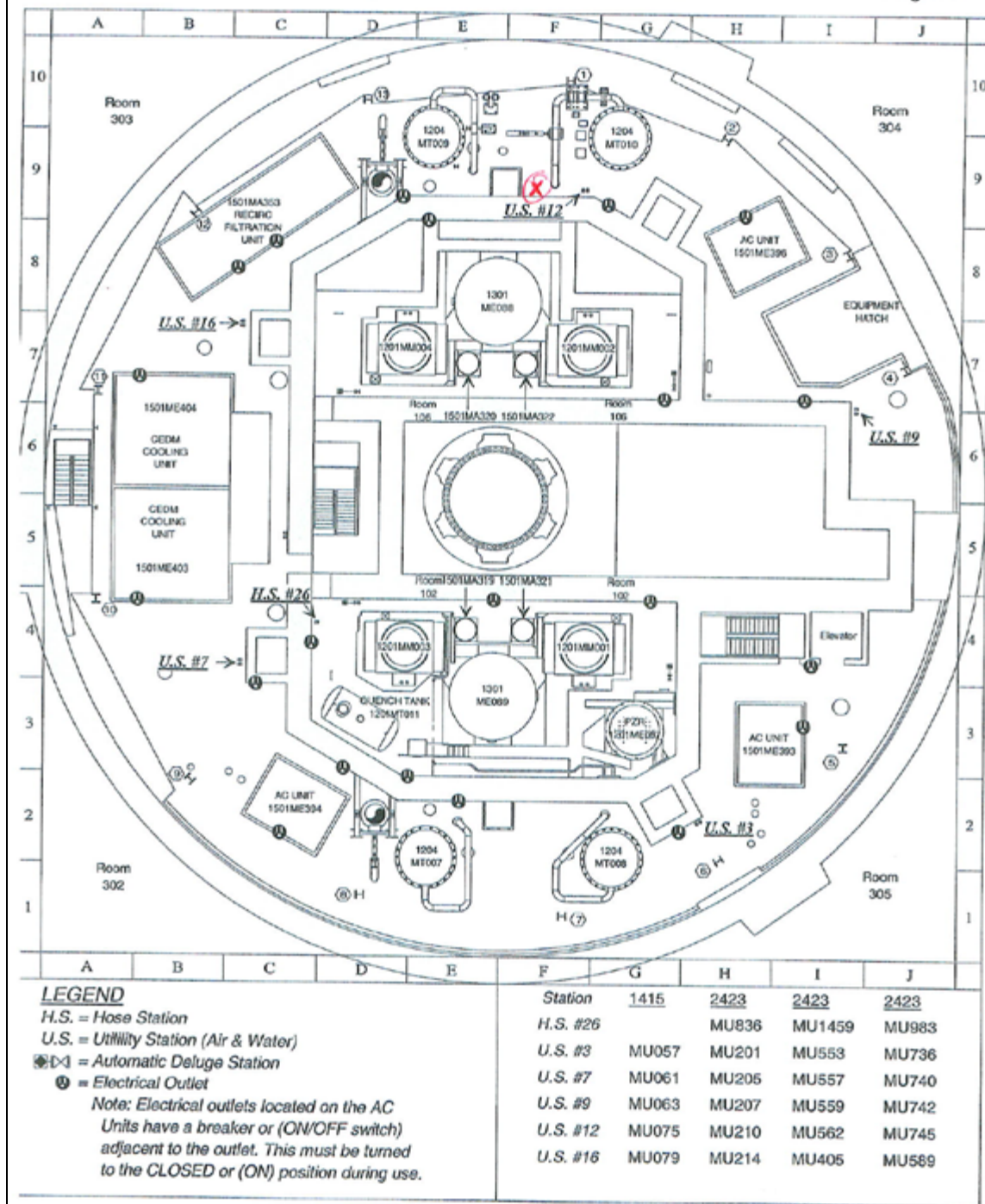
Figure A-3   Coring location at 45 ft elevation

APPENDIX B MXRF IMAGES AND PLOTS

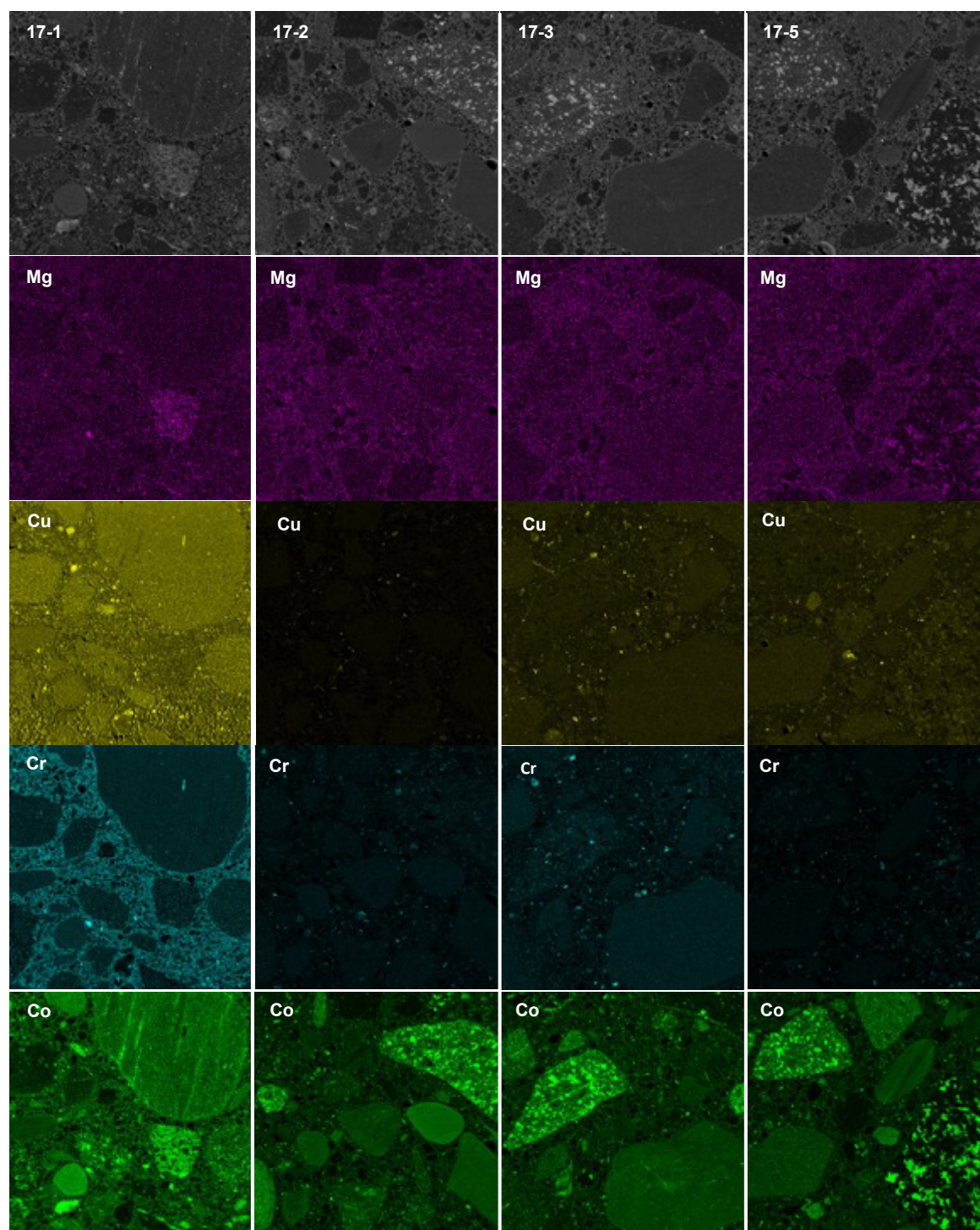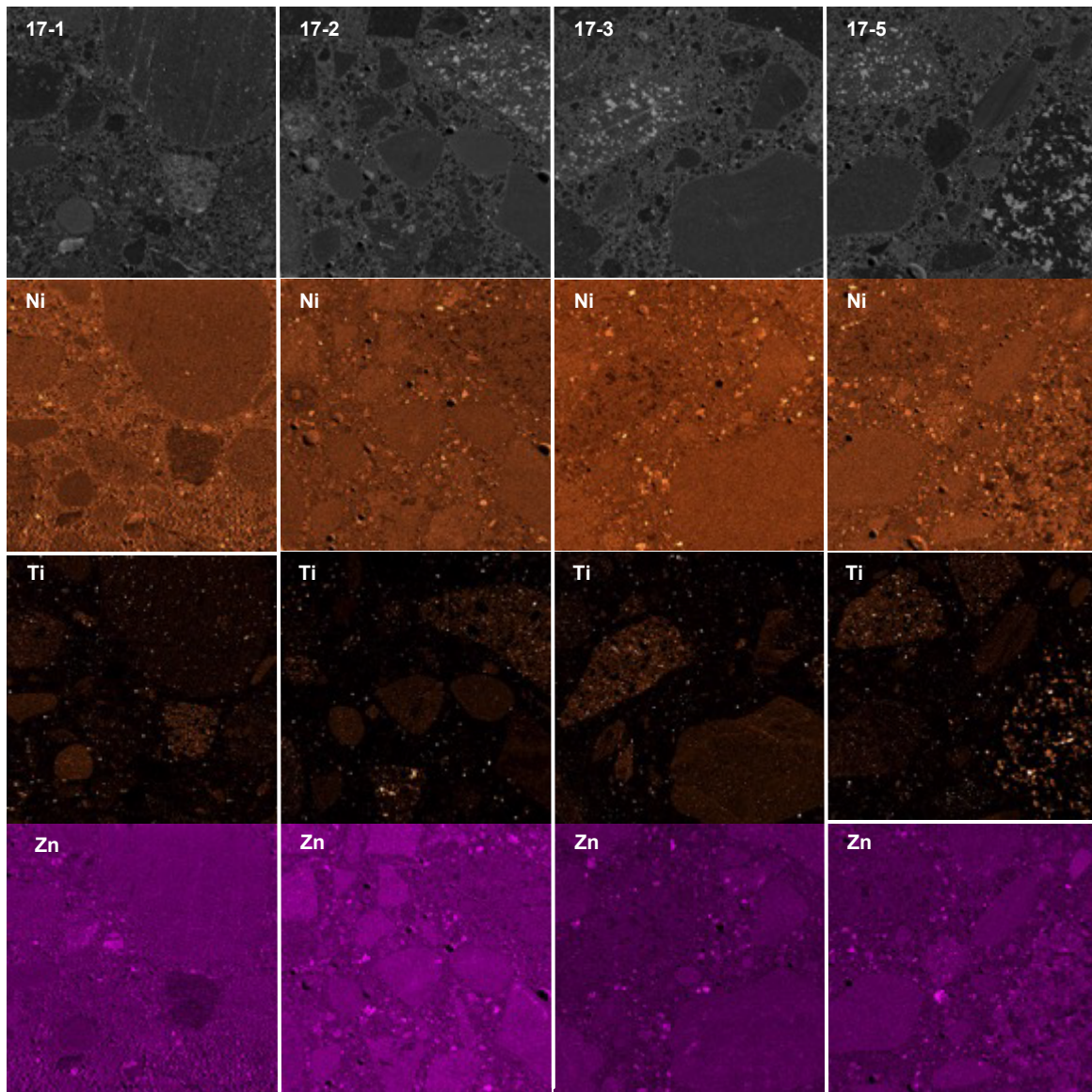**Figure B-1   Element intensity maps of magnesium, copper, chromium, and cobalt**

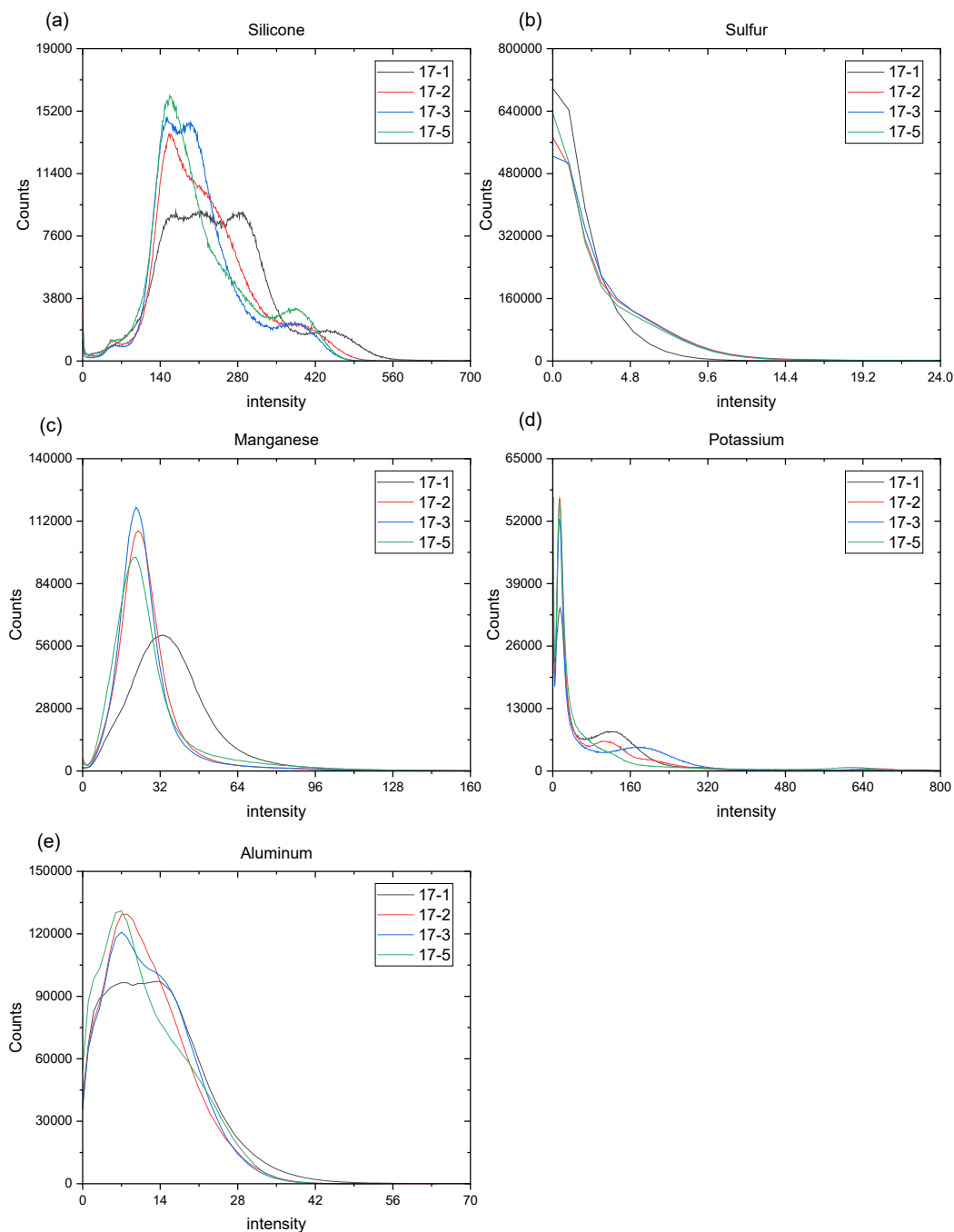**Figure B-2   Element intensity maps of nickel, titanium, and zinc**

Figure B-3   Intensity histograms: (a) silicon, (b) sulfur, (c) manganese, (d) potassium, and (e) aluminum
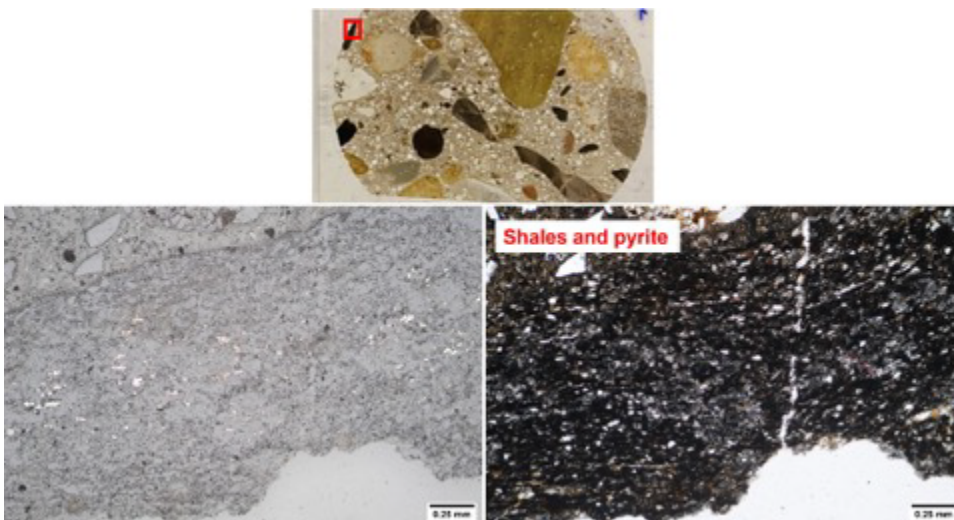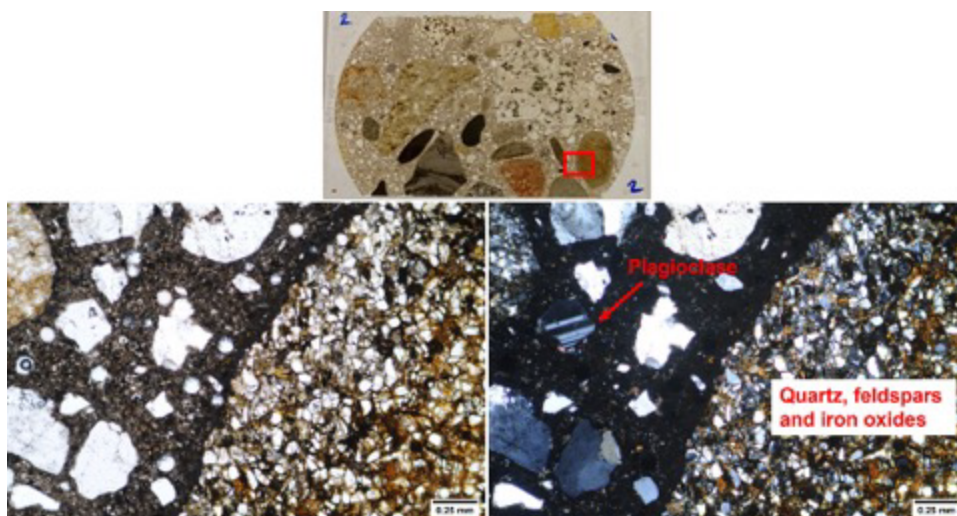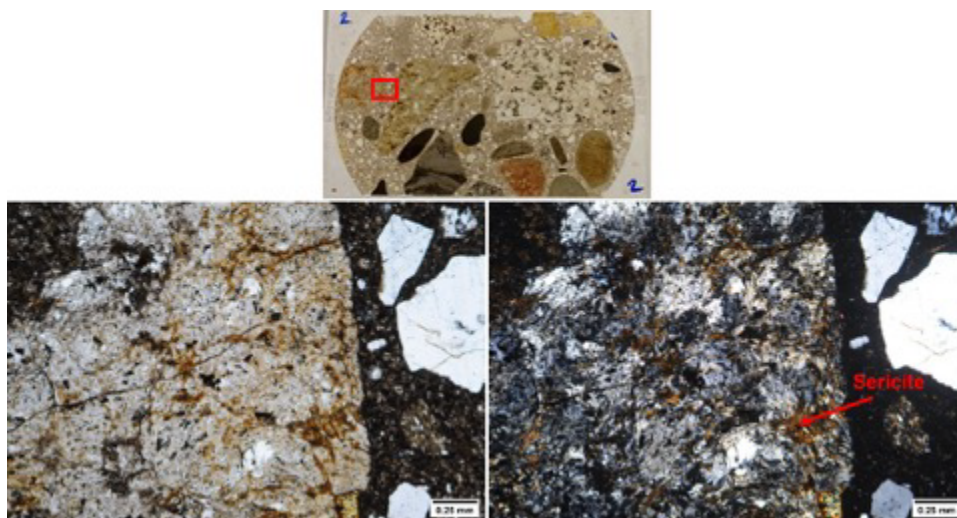
APPENDIX C PETROGRAPHIC IMAGES
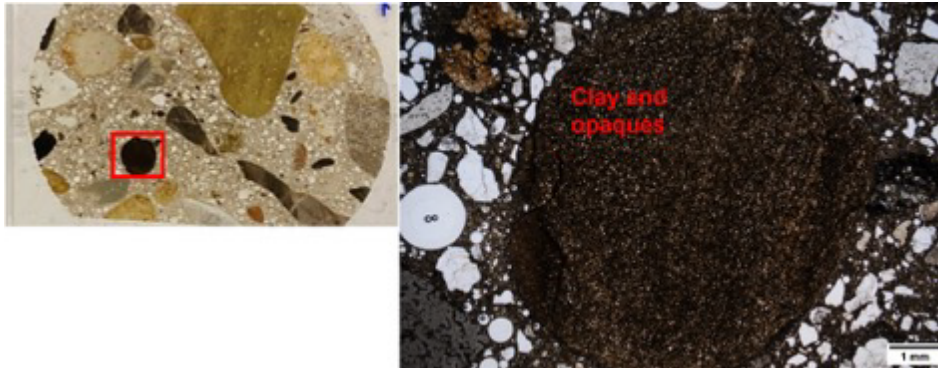
Figure C-1   Petrographic image of the aggregate marked with the red rectangle using transmitted light and crossed polarizers
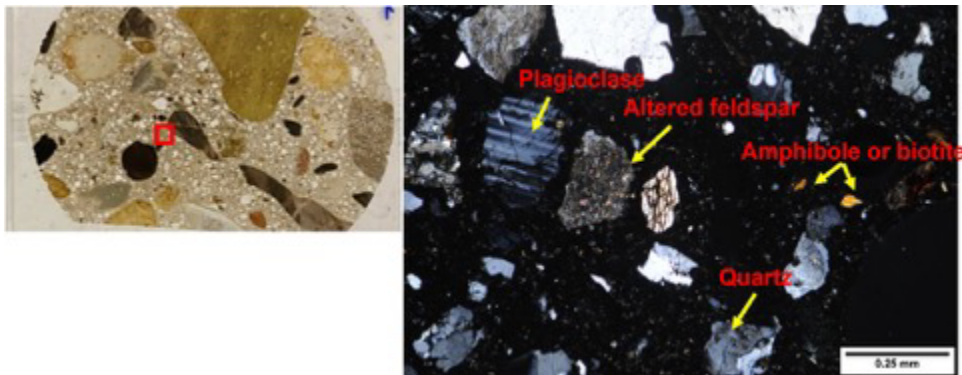
Figure C-2   Petrographic image of the area marked with the red rectangle within the cement paste showing small aggregates using transmitted light and crossed polarizers
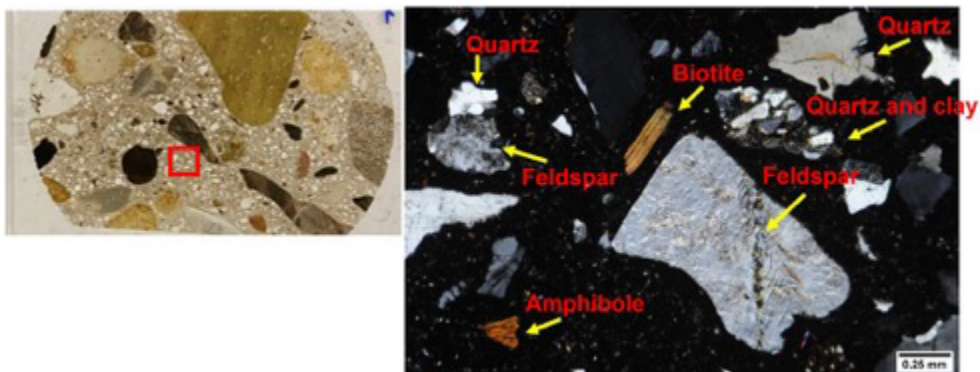
Figure C-3   Petrographic image of the cement paste area marked with the red rectangle showing small aggregates using transmitted light and crossed polarizers
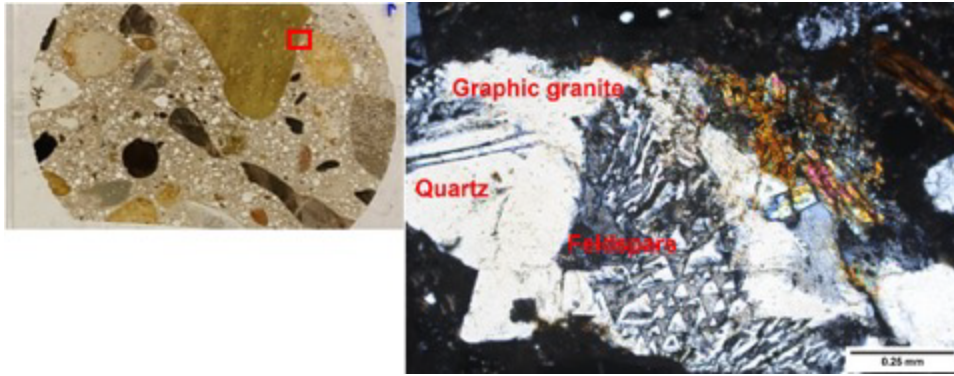
Figure C-4 **Petrographic image of the area marked with the red rectangle showing a small granitic aggregate using transmitted light and crossed polarizers**
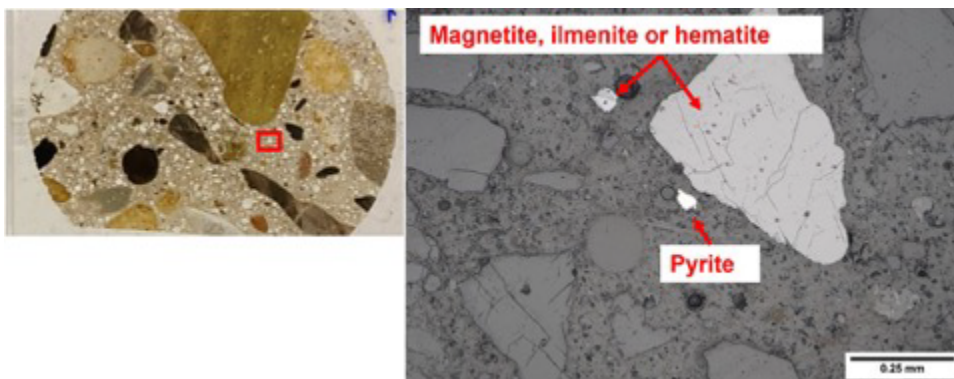
Figure C-5 **Petrographic image taken with reflected light showing small aggregates and cement paste in the area marked with the red rectangle**

Figure C-6 **Petrographic images of the aggregate marked with the red rectangle using reflected light (left) and transmitted light with crossed polarizers (right)**

Figure C-7   Petrographic images of the edge of the aggregate marked with the red rectangle using transmitted light with uncrossed polarizers (left) and crossed polarizers (right)
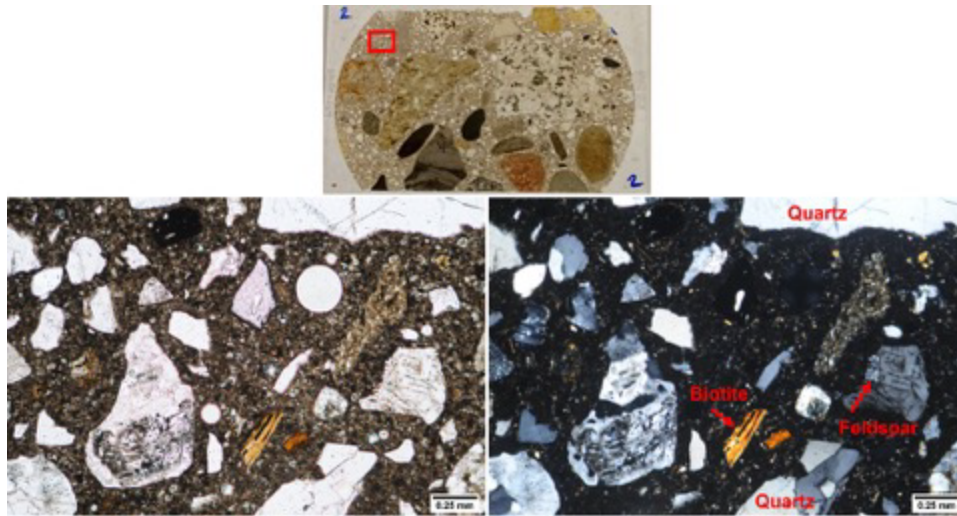

Figure C-8   Petrographic images of the edge of the aggregate marked with the red rectangle using transmitted light with uncrossed polarizers (left) and crossed polarizers (right)

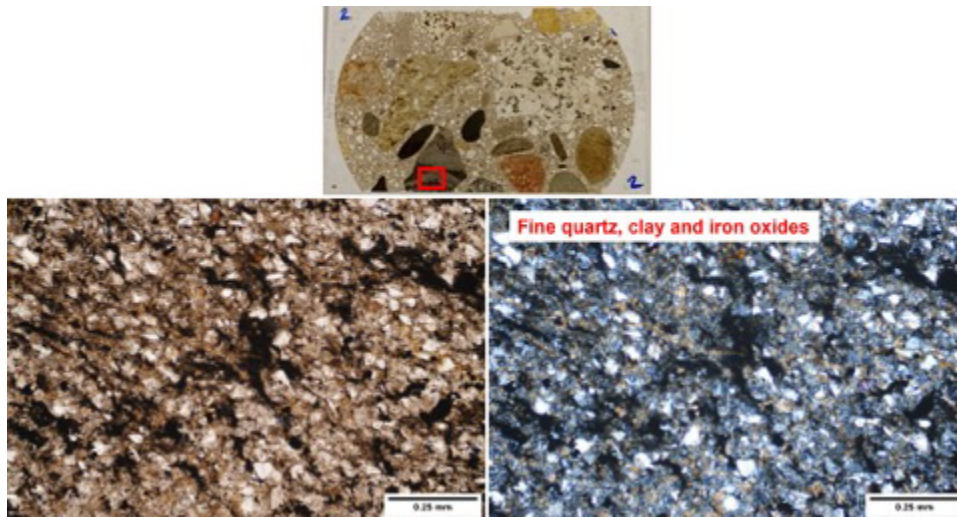**Figure C-9** Petrographic images of small aggregates in the cement paste from the area marked with a red rectangle using transmitted light with uncrossed polarizers (left) and crossed polarizers (right)

Figure C-10 Petrographic images of the aggregate marked with a red rectangle using transmitted light with uncrossed polarizers (left) and crossed polarizers (right)
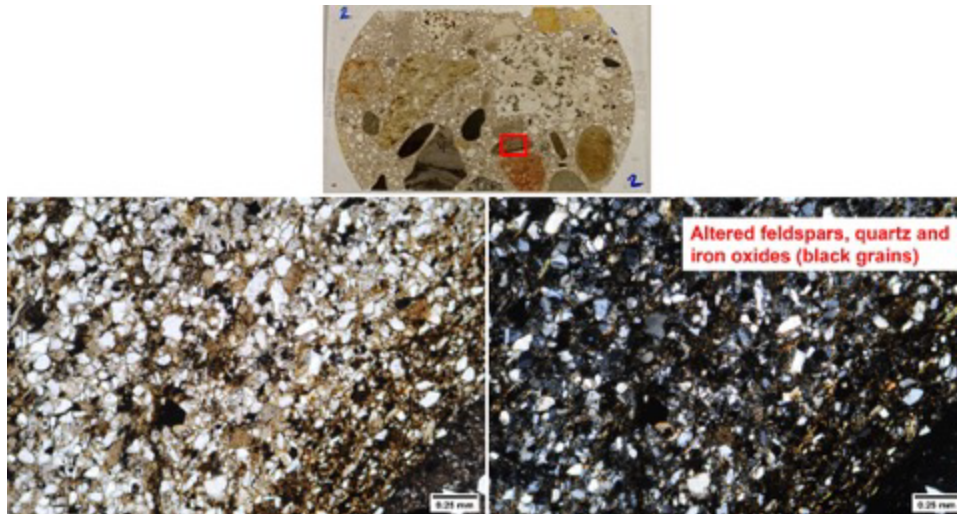
Figure C-11 Petrographic images of the area marked with the red rectangle using transmitted light with uncrossed polarizers (left) and crossed polarizers (right)
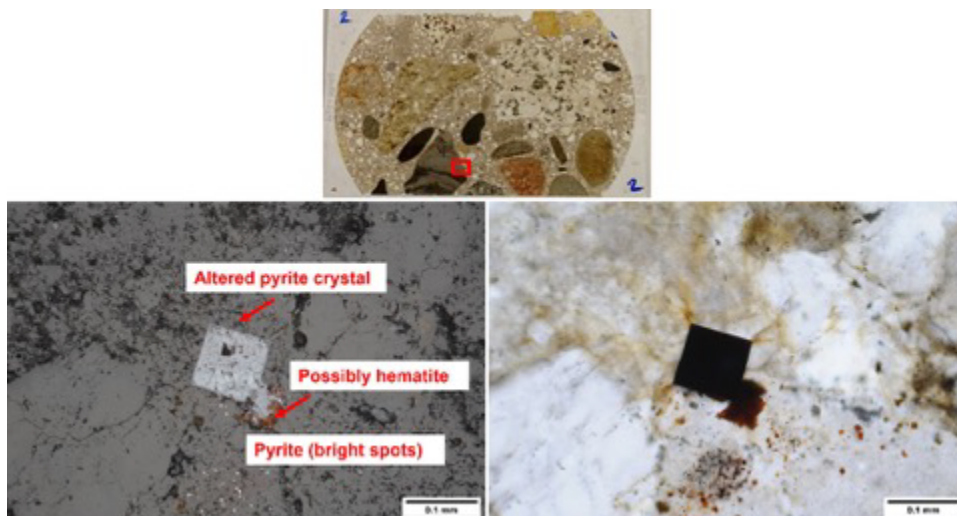

Figure C-12 Petrographic images of the aggregate marked with the red rectangle using reflected light (left) and transmitted light with uncrossed polarizers (right)
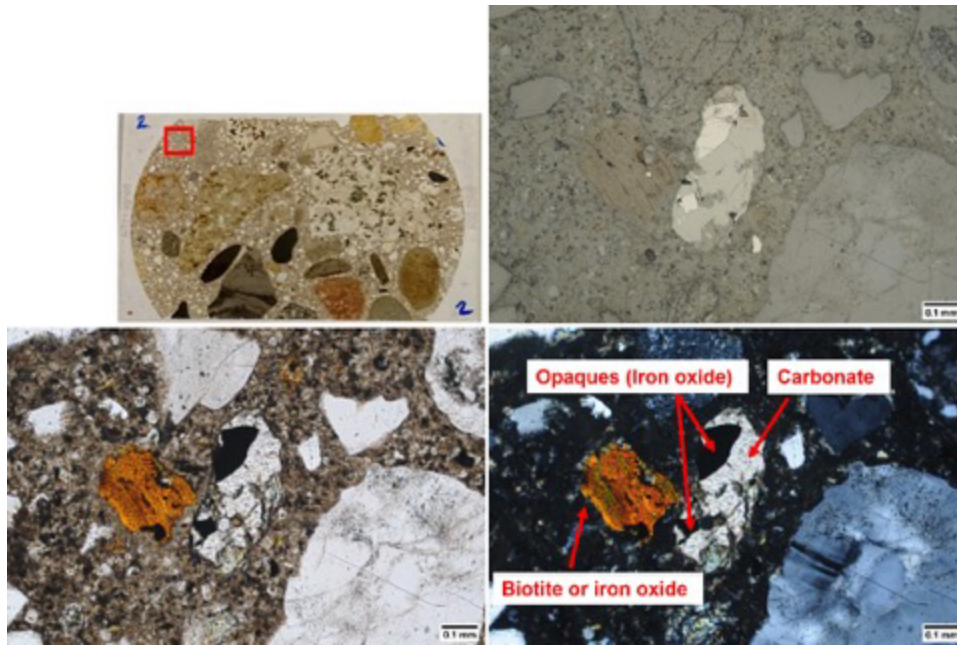
Figure C-13 Petrographic images of small aggregates in the cement paste from the area marked with the red rectangle using reflected light (top right), transmitted light with uncrossed polarizers (bottom left), and crossed polarizers (bottom right)

Figure C-14 Petrographic images of small aggregates in the cement paste from the area marked with the red rectangle using transmitted light with uncrossed polarizers (left) and reflected light (right)
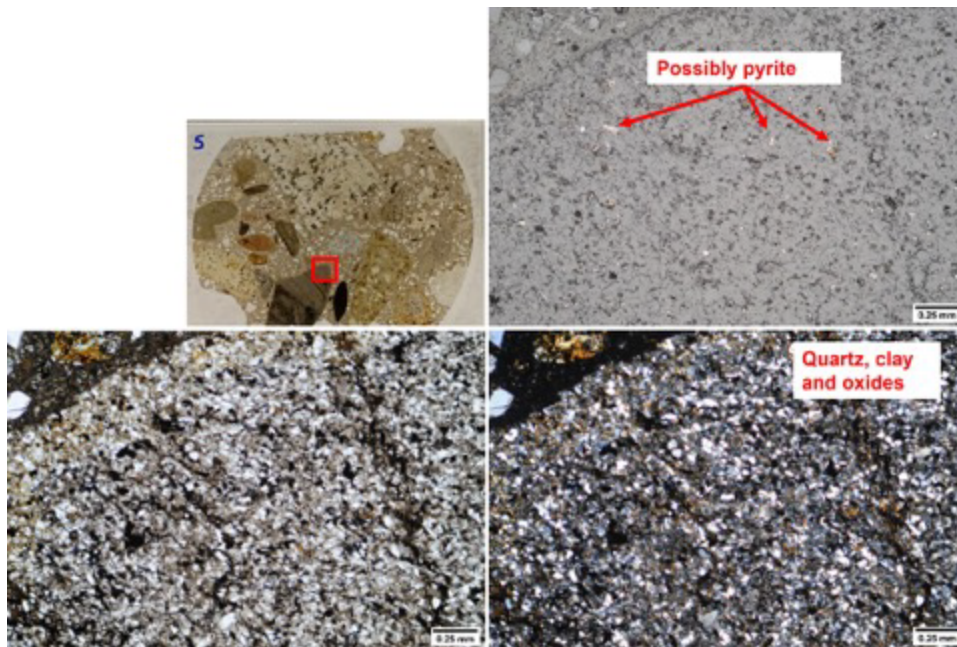
Figure C-15 Petrographic images of the tip of the aggregate marked with the red rectangle using reflected light (top right), transmitted light with uncrossed polarizers (bottom left), and crossed polarizers (bottom right)
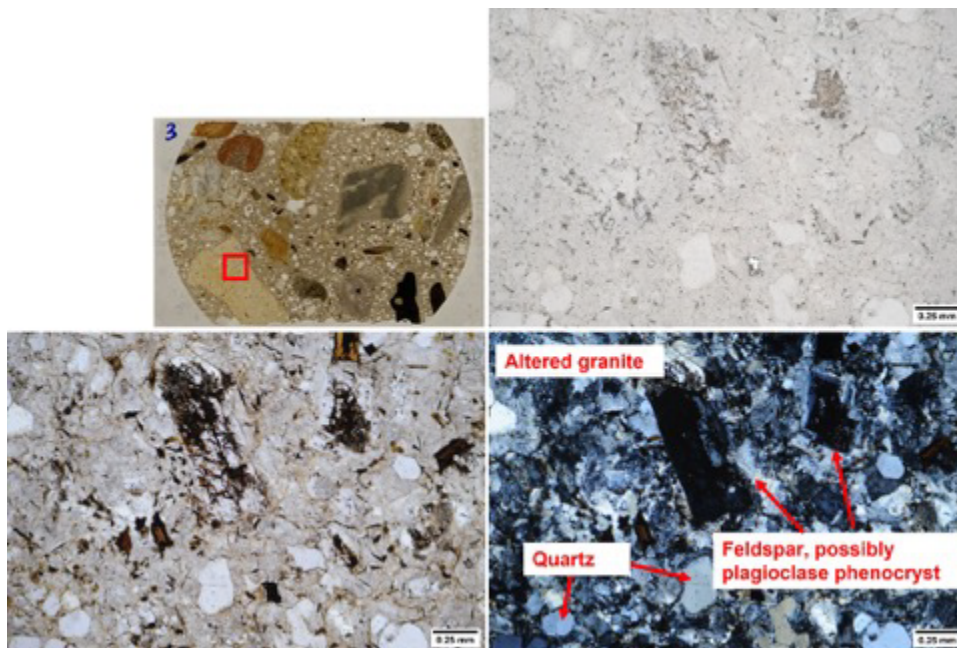

Figure C-16 Petrographic images from the area marked with the red rectangle using reflected light (top right), transmitted light with uncrossed polarizers (bottom left), and crossed polarizers (bottom right)